The Astrophysical Journal Supplement Series, 268:20 (36pp), 2023 September https://doi.org/10.3847/1538-4365/ace69f

Long-term X-Ray Outburst in the TeV-detected Blazar Mrk 501 in 2021–2022: Further Clues for the Emission and Unstable Processes

B. Kapanadze[1,2,3], A. Gurchumelia[2,4], and M. Aller[5]
[1] Space Research Center, Department of Astronomy and Astrophysics, School of Natural Sciences and Medicine, Ilia State University, Colokashvili Av. 3/5, Tbilisi, 0162, Georgia; bidzina_kapanadze@iliauni.edu.ge
[2] E. Kharadze National Astrophysical Observatory, Mt. Kanobili, Abastumani, 0803, Georgia
[3] INAF, Osservatorio Astronomico di Brera, Via E. Bianchi 46, I-23807 Merate, Italy
[4] Department of Physics, I. Javaksishvili State University, Chavchavadze Av. 3, Tbilisi 012, Georgia
[5] Astronomy Department, University of Michigan, Ann Arbor, MI 48109-1107, USA
Received 2023 April 20; revised 2023 May 25; accepted 2023 June 20; published 2023 September 1

Abstract

This paper presents the results of a detailed X-ray timing and spectral analysis of Mrk 501, which are based mainly on the Swift data obtained during 2021 February–2022 December. The source showed strongly enhanced X-ray activity, characterized by a long-term increase in the baseline 0.3–10 keV flux level superimposed by shorter-term flares on timescales of a few weeks to about 2 months. During some time intervals, Mrk 501 was the brightest blazar in the X-ray sky and, moreover, showed an intense intraday variability, which was sometimes detected within the exposures lasting a few hundred seconds. These instances were characterized by fractional variability amplitudes of 4%–18% and were mostly observed during short-term X-ray flares. The source exhibited extreme spectral properties with dominance of the spectral curvature, frequent occurrence of hard photon indices in the 0.3–10 keV and 0.3–300 GeV bands, and the peak of a synchrotron spectral energy distribution in the hard X-ray range. These properties demonstrate the importance of relativistic magnetic reconnection, first-order Fermi mechanism within the magnetic field of different confinement efficiencies, stochastic acceleration, and hadronic processes. The X-ray and γ-ray fluxes showed a log-normal distribution, which hints at the imprint of accretion disk instabilities on the blazar jet, as well as the possible presence of hadronic cascades and random fluctuations in the particle acceleration rate. The optical–UV and γ-ray variabilities showed a weak or absent correlation with the X-ray flaring activity, which is not consistent with simple leptonic models and requires more complex particle acceleration, emission, and variability scenarios.

Unified Astronomy Thesaurus concepts: BL Lacertae objects (158)

Supporting material: figure set, machine-readable tables

1. Introduction

Blazars form a class of active galactic nuclei (AGNs) with a relativistic jet of magnetized plasma, emerging with a relativistic bulk velocity from the vicinity of the central supermassive black hole (SMBH) and pointed almost along the observer's line of sight (see Padovani & Giommi 1995 and references therein). Among the different blazar subclasses, BL Lacertae objects (BL Lac objects) are remarkable for featureless optical spectra, very broad continuum extending from the radio to the very high-energy (VHE; $E > 100$ GeV) γ-rays, compact radio-structure with apparent superluminal motion of some components and strong flux variability in all spectral bands (Falomo et al. 2014). The broadband spectral energy distribution (SED) is dominated by nonthermal, strongly Doppler-boosted, and variable emission produced in the innermost jet area (Abdo et al. 2011a). In the $\log \nu$–$\log \nu F_\nu$ plane, the SED represents two different components: the lower-energy "hump" extends over the radio-to-X-ray frequencies and is widely accepted to be synchrotron emission of a relativistic, magnetized plasma. Based on the position of the synchrotron SED peak E_p, BL Lac objects are broadly divided into two subclasses (Padovani & Giommi 1995): high-energy-peaked (HBLs, peaking at UV-to-X-ray frequencies) and low-energy-peaked (with E_p situated in the IR–optical part of the spectrum) objects.

However, we still have not achieved an unambiguous identification of the physical mechanisms responsible for the higher-energy SED component (γ-rays in HBLs) and various emission scenarios are proposed: (1) inverse Compton (IC) scattering of synchrotron photons by their "parent" electron–positron population (the synchrotron self-Compton model, SSC; Marscher & Gear 1985 and references therein); (2) external Compton scattering (Dermer et al. 1992), with "seed" photons contributed by the non-jet AGN components (accretion disk, broad and narrow emission line clouds, dust thorus); and (3) hadronic models that predict the production of γ-rays by relativistic protons either directly (the proton synchrotron model; Mannheim 1992) or indirectly (e.g., synchrotron emission from a secondary electron population, generated by the interaction of high-energy protons with ambient photons; Mücke et al. 2003). While the first mechanism characterized by (nearly) simultaneous variations in both the synchrotron and higher-energy components, the latter models "tolerate" a complicated multiwavelength (MWL) timing behavior with absent or time-shifted correlation. A valid model can be selected through the intense study of MWL flux variability, interband cross-correlations, and X-ray and γ-ray spectral properties. These studies are also useful for solving some other open questions of the blazar physics like the location and

Table 1
Summary of the Time Intervals Selected for Our Analysis (Interval 1) and for Comparison (2008–2020)

Interval (1)	Dates (2)	MJD (3)	N_{obs} (4)	$N_{tab:11}$ (%) (5)	α (6)	N_{hard}^{LAT} (%) (7)
Interval 1	2021 Feb 12–2023 Jan 1	(59)257–945	190	45.1	0.43(0.08)	38.0
Interval 1a	2021 Feb 12–2021 Dec 10	(59)257–558	73	58.1	⋯	43.5
Interval 1b	2021 Dec 16–2022 Jul 13	(59)564–773	79	36.2	0.40(0.12)	25.0
Interval 1c	2022 Jul 15–2023 Jan 1	(59)775–945	38	50.0	⋯	46.3
2016–2020	2016 Mar 8–2020 Sep 20	57,455–59,118	319	53.0	0.30(0.10)	31.7
2014–2015	2014 Mar 1–2015 Sep 28	56,717–57,293	321	25.5	0.49(0.08)	25.0
2011–2013	2011 Mar 3–2013 Sep 1	55,623–56,536	182	53.2	0.50(0.08)	37.1
2008–2010	2008 Mar 28–2010 Aug 21	54,553–55,430	107	40.9	0.18(0.09)	36.1

Note. Columns are as follows: ranges of the Gregorian and corresponding modified Julian dates (columns 2 and 3, respectively); number of the XRT observations (column 4); portion of the power-law spectra among all 0.3–10 keV ones (column 5); value of the exponent in the relation $S_p \propto E_p^{\alpha}$ (column 6); and portion of those 2-weekly integrated LAT-band spectra showing a harder photon index in the 2–300 GeV sub-band compared to that in the 0.3–2 GeV one (column 7).

structure of their dominant emission zones, the origin of their variability, jet matter content, etc. For these purposes, very important clues can be provided by the intense MWL timing and spectral investigation of the nearby ($z = 0.0337$; Ulrich et al. 1975) HBL source Mrk 501, which is one of the brightest at X-rays and a strong TeV emitter.

Mrk 501 became the second extragalactic source detected in the TeV band with the Whipple telescope in 1995 and showing variability on timescales of days; Quinn et al. 1996). Afterwards, it underwent a prolonged, exceptionally strong TeV-activity in 1997 March–April, accompanied by correlated X-ray variability on timescales of days (Aharonian et al. 1997; Catanese et al. 1997 etc.). In that epoch, the X-ray spectra frequently were very hard and the parameter E_p showed an extreme shift to ∼100 keV or above (Pian et al. 1998). In 1998 June, a second TeV-band outburst was observed, along with a shift of the synchrotron SED peak to the energies $\gtrsim$50 keV (Sambruna et al. 2000). During the MAGIC campaign in 2005 May–June, the TeV-band flux varied by an order of magnitude, and an intraday variability (IDV) with the flux-doubling timescale of ∼2 minutes was recorded (Albert et al. 2007). We reported powerful and long-lasting X-ray flaring activity (Kapanadze et al. 2017, hereinafter Paper I), based on the intense observations with Swift-XRT (Burrows et al. 2005) during 2014 March–October: a long-term X-ray outburst with shorter-term flares by factors of 2–5 on timescales of a few weeks and intense 0.3–10 keV IDVs, sometimes occurring within 1 ks of observational runs. During strong flares, the spectral index frequently became harder than 1.70. The spectral evolution was characterized by a harder-when-brighter behavior with a shift of the quantity E_p by more than 20 keV.

The source was reported to show another prolonged, strong 0.3–10 keV activity, which started in 2021 February (Kapanadze 2021a, 2021b, 2021c, 2022a, 2022b) and the 0.3–10 keV flux declined to the nearly initial level in 2022 December. In this paper, we present the results of a detailed X-ray timing and spectral analysis of Mrk 501 focused on the long-term Swift-XRT observations performed in 2021 February–2022 December (hereafter, Interval 1; see Table 1). We analyzed the X-ray flaring behavior during the particular subintervals; constructed histograms characterizing the distributions of the different spectral parameters and MWL fluxes; and checked cross-correlations between these parameters and/or MWL fluxes. The obtained results are compared with the predictions of various theoretical studies and simulations presented by different authors to date, as well as with the spectral results from the previous years (2008–2020). In order to check the MWL cross-correlations, we also examined the data trains obtained with the (i) Ultraviolet-Optical Telescope (UVOT; Roming et al. 2005) on board Swift (Gehrels et al. 2004); (ii) Burst Alert Telescope (BAT; Barthelmy et al. 2005) on board the same space mission; (iii) Monitor of All Sky X-ray Image (MAXI; Matsuoka et al. 2009); (iv) Large Area Telescope (LAT) on board Fermi (Atwood et al. 2009); and (v) First G-APD Cherenkov Telescope (FACT; Anderhub et al. 2009).

The paper is organized as follows: Section 2 describes the data processing and analysis procedures. In Section 3, we provide the results of the timing analysis and X-ray spectroscopy. We discuss our results in Section 4, and provide the corresponding summary and conclusions in Section 5.

2. Data Sets, Reduction, and Analysis

2.1. X-Ray Data

The XRT observational log of Mrk 501 is presented in Table 2.[6] We retrieved the raw observational data obtained from the publicly available archive maintained by HEASARC.[7] The Level-1 unscreened XRT event files (in `FITS` format) were processed with the `XRTDAS` package (version 3.6.1) developed at the ASI Science Data Center (ASDC) and distributed by HEASARC within the `HEASOFT` package (version 6.30.1). These files were reduced, calibrated, and cleaned by means of the `XRTPIPELINE` script, adopting the standard filtering criteria (grade, region, time, energy, intensity, and phase filterings) and the latest calibration files incorporated by Swift-XRT CALDB (Version 20210924). The details of these steps, as well as those related to the extraction of the 0.3–10 keV light curved and spectra are provided in Paper I.

The instrument with the largest field of view (FOV, 1.4 sr; Barthelmy et al. 2005), Swift-BAT, observed Mrk 501 in the 15–150 keV energy range during our period of study, monitoring the entire sky at hard X-rays every few hours. We retrieved the daily binned data, processed using the BAT CALDB (version 20171016) and publicly available on the website of the Hard X-ray Transient Monitor program[8]

[6] The three leading zeros in observation IDs (ObsIDs) are omitted throughout the paper.
[7] http://heasarc.gsfc.nasa.gov/docs/archive.html
[8] https://swift.gsfc.nasa.gov/results/transients/weak/3EGJ0853p1941/

Table 2
XRT Observations of Mrk 501

ObsID (1)	Obs. Start–End (UTC) (2)	Exp. (s) (3)	MJD (4)	CR (counts s^{-1}) (5)	χ^2_r/DOF (6)	Bin (s) (7)	Var. (8)
11184079	2021-02-12 12:39:35 02-12 13:34:59	900	59,257.527	3.50(0.08)	5.96/6	120	V
11184080	2021-02-16 12:13:36 02-16 13:10:31	810	59,261.501	3.89(0.08)	2.79/6	120	NV
11184081	2021-02-20 11:47:36 02-20 12:44:32	810	59,265.491	4.04(0.05)	1.99/6	120	NV

Note. The columns are as follows: (1) observation ID; (2) observation start–end (in UTC); (3) exposure (in seconds); (4) modified Julian date corresponding to the observation start; (5)–(7): mean value of the 0.3–10 keV count rate with the associated error (in counts s^{-1}), reduced χ^2 with the corresponding degrees of freedom (DOF) and time bin used for light-curve construction, respectively; (8) existence of brightness variability during the observation (V stands for variability detection; PV—possibly variable; NV—nonvariable).

(This table is available in its entirety in machine-readable form.)

Table 3
Results from the UVOT Observations

	V			*B*			*U*		
ObsID (1)	Mag. (2)	Flux (mJy) (3)	$\log \nu F_\nu$ (4)	Mag. (5)	Flux (mJy) (6)	$\log \nu F_\nu$ (7)	Mag. (8)	Flux (mJy) (9)	$\log \nu F_\nu$ (10)
11184156	13.07(0.02)	13.51(0.43)	−10.125(0.014)	13.69(0.04)	9.82(0.43)	−10.167(0.019)	13.53(0.03)	4.86(0.13)	−10.382(0.012)
11184157	13.11(0.02)	12.72(0.43)	−10.151(0.014)	13.80(0.04)	8.52(0.33)	−10.229(0.017)	13.48(0.03)	5.12(0.11)	−10.360(0.009)
11184158	13.09(0.02)	13.11(0.43)	−10.138(0.014)	13.81(0.04)	8.40(0.33)	−10.235(0.017)	13.53(0.03)	4.86(0.11)	−10.382(0.010)

Note. In columns (4), (7), and (10), the flux values are given in units of erg cm^{-2} s^{-1}.

(This table is available in its entirety in machine-readable form.)

(Krimm et al. 2013). As the source was relatively rarely detectable with 5σ significance (the threshold typically adopted for the variability studies with the coded-mask devices) with BAT, integration times of 2 days or longer were adopted. For this purpose, we used the tool `REBINGAUSSLC` from `HEASOFT` and rebinned the BAT data within the time intervals of 2–4 days and 1–4 weeks.

The background-subtracted 2–20 keV MAXI data are normalized using the instrument response function and are publicly available.[9] Similar to BAT, we filtered these data using the 5σ detection threshold (as recommended by the MAXI team; T. Mihara 2023, private communication). Using the online tool `MAXI ON-DEMAND PROCESS`,[10] we also extracted the 2–20 keV light curve with the integration times of 2–4 days and 1–4 weeks. The same was done for the different bands of this energy range, in order to achieve the maximum number of the 5σ detections.

2.2. Optical–UV Observations

In the course of each XRT exposure, the target was observed with UVOT in six optical–UV bands *V*, *B*, *U*, *UVW*1, *UVM*2, and *UVW*2. We retrieved the sky-corrected images from HEASARC and performed absolute photometry using the `UVOTSOURCE` tool (included by `HEASOFT`). The measurements were done by means of the source aperture radius amounting to 5″ and 10″ in the optical and UV bands, respectively: the source was significantly brighter at the UV frequencies and characterized by an approximately twice-as-large image. The derived magnitudes were then corrected for the Galactic absorption. For this purpose, we adopted the value $E(B-V) = 0.023$ mag (see Paper I). Using the interstellar extinction curves provided by Fitzpartick & Massa (2007), we calculated the $A_\lambda/E(B-V)$ value for each of the UVOT bands (0.07 mag, 0.09 mag, 0.11 mag, 015 mag, 0.22 mag and 0.20 mag, respectively). Using the effective wavelength of each band (Poole et al. 2008) and the photometric zero-points provided in Breeveld et al. (2011), we converted the corrected magnitudes into the linear fluxes (in millijanskys). The calculated optical–UV magnitudes and fluxes in each UVOT band are presented in Table 3.

The host contribution was estimated by using the color-indices $V-R = 0.61$ mag, $B-V = 0.96$ mag and $U-B = 0.64$ mag derived from Fukugita et al. (1995). Adopting the host *R*-band flux of 12 mJy (see Nilsson et al. 2007 and references therein), we determined the host *R*-band value $m_R = 13.52$ mag by using the relation (Nilsson et al. 2007)

$$F = 10^{0.4(16.22-m_R)}, \quad (1)$$

where the flux is given in millijanskys. In the *V*, *B*, and *U* bands, the host contribution amounts to 8.17 mJy, 3.73 mJy and 0.74 mJy, respectively. As for the UV fluxes of Mrk 501 in the $UVW1-UVW2$ bands, they are not affected by the host emission (see Acciari et al. 2020).

2.3. γ-Ray Observations

The high-energy (HE; $E > 100$ MeV) Fermi-LAT data were analyzed using the `Fermitools` package version 2.2.0. We adopted the post-launch instrument response function `P7SOURCE_V7` and extracted the 0.3–300 GeV fluxes from the LAT observations for optimizing the analysis quality: (i) the LAT effective area is largest (>0.5 m^2) in this energy range; (ii) the angular resolution is relatively good when $E \geqslant 300$ GeV (the 68% containment angle is smaller than 2° versus 3.5° at ∼100 MeV); (iv) minimize contamination by misclassified cosmic rays (Atwood et al. 2009). Consequently,

[9] http://maxi.riken.jp/star_data/J0035+598/J0035+598.htm
[10] http://maxi.riken.jp/mxondem/

we deal with smaller systematic errors and obtain the highest signal-to-noise ratio for the target; additionally, the spectral fit is less-affected by possible contamination from the neighboring transient sources (Abdo et al. 2011b).

Only the events of the diffuse class (associated with the highest probability of belonging to the source) from a region of interest (ROI) of radius 10° centered on Mrk 501 were selected and processed using the unbinned maximum likelihood method `GTLIKE`.[11] Only those photons belonging to `evclass` = 128 and `evtype` = 3 and flagged with (DATA_QUAL==1) and (LAT_CONFIG==1) were selected for our analysis: the spacecraft was outside the South Atlantic Anomaly, and the source was in the LAT FOV. A cut on the zenith angle (>90°) was made to reduce contamination from the Earth-albedo γ-rays. The data taken when the rocking angle of the spacecraft was larger than 52°, and were discarded to avoid time intervals during which the Earth entered the LAT FOV.

Using the user-contributed tool `make4FGLxml.py`,[12] we created a background model, which includes all point γ-ray sources from the Fourth Fermi-LAT Catalogue (4FGL; Abdollahi et al. 2020) within 20° from the position of Mrk 501. For the spectral modeling of our target, we adopted a log-parabolic model, as done in the catalog. The spectral parameters of sources within the ROI were left free during the minimization process, while those situated beyond this radius were fixed to the 4FGL values. The Galactic and extragalactic diffuse γ-ray emission as well as an isotropic component (including a residual instrumental background) were incorporated in the model, adopting the recommended model files `gll_iem_v07.fits` and `iso_P8R3_SOURCE_V3_v1.txt`, respectively. The detection significance of the target is given by $\sigma \approx (\mathrm{TS})^{1/2}$ (Abdo et al. 2009) where TS is the test statistics, the value of which is derived along with those of the spectral parameters. When the source was not detectable with at least a 3σ significance and/or `GTLIKE` yielded a low value for the model-predicted photons $N_{\mathrm{pred}} \lesssim 8$, we calculated a 2σ upper limit to the photon flux using the Python-based tool `UpperLimits`.[13]

Mrk 501 is monitored by the FACT telescope (Observatorio del Roque de los Muchachos, La Palma, Spain) in the TeV energy range since 2011 October. The FACT collaboration publishes the results of a quick-look analysis on a website.[14] The details of this analysis are provided in Dorner et al. (2015). Generally, the background-subtracted VHE excess rates are not corrected for the effect of changing energy threshold with various zenith distances and ambient light, and no data selection is done. However, we have restricted our timing study to the nights with a signal detected with a minimum significance of 3σ: more than 98% of these data were taken with zenith distances small enough to not significantly influence the energy threshold of the analysis. Nevertheless, more than 84% of these data are taken under light conditions that do not increase the analysis threshold. From the daily binned data, we used 69 nights (89.4 hr) for the study, selecting detections with a minimum significance of 3σ for four nights. The duration of the latter observations ranged between 0.56 and 2.07 hr.

[11] https://fermi.gsfc.nasa.gov/ssc/data/analysis/scitools/
[12] https://fermi.gsfc.nasa.gov/ssc/data/analysis/user/make4FGLxml.py
[13] https://fermi.gsfc.nasa.gov/ssc/data/analysis/scitools/upper_limits.html
[14] http://www.fact-project.org/monitoring

3. Results

3.1. X-Ray Flux Variability

3.1.1. Long-term Behavior

Mrk 501 was targeted 199 times with XRT between 2021 February 12 and 2022 December 31, yielding a net exposure of 171 ks (see Table 2). However, three exposures were very short for extracting any useful information (~50 s or shorter; ObsIDs (11184)097, 101, 105, 110). During some observations (ObsIDs(11184)103, 167, 232 and 96029006), the image center of Mrk 501 was just at the edge of the observational area or beyond, and we excluded those cases from our study to avoid incorrect PSF reconstruction. Moreover, the highest 0.3–10 keV count rate (CR ~ 40 counts s^{-1} was derived from the XRT pointing with ObsID 11184197 (performed on 2022 April 12, MJD 59,681), which was clearly due to an instrumental effect: there is a "hot" central pixel with the count ~10 times higher than that from the adjacent pixels. The fit of the corresponding spectrum with the log-parabolic model (see Section 3.2) produces a large excess at the energies $E < 0.45$ keV (a similar situation is obtained when adopting a simple power-law model). After removing the corresponding channels from the fit, we obtained a good fit with this model ($\chi^2_{\mathrm{r}} = 1.05$ with 207 degrees of freedom, DOF), yielding $a = 1.78 \pm 0.04$, $b = 0.29 \pm 0.08$ and unabsorbed flux $F_{0.3-10\,\mathrm{keV}} = (3.37 \pm 0.08) \times 10^{-10}\,\mathrm{erg\,cm^{-2}\,cm^{-1}}$. After performing interpolation from the XRT observations of Mrk 501 with the same 0.3–10 keV flux and values of the spectral parameters (within the error ranges), we derived the 0.3–10 keV count rate CR = 11.95 ± 0.12 counts s^{-1}, which is significantly lower than the maximum rate shown by the source in the here-presented period.

Figures 1(a) and 2(a) show that Mrk 501 underwent a strong, long-term X-ray flare with a wide range of the 1 day binned 0.3–10 keV count rate CR = 3.50(0.08) counts s^{-1}–15.51(0.14) counts s^{-1} (corresponding to the unabsorbed flux $F_{0.3-10\,\mathrm{keV}} = (1.00\text{–}5.47) \times 10^{-10}\,\mathrm{erg\,cm^{-2}\,s^{-1}}$) in Interval 1. Table 4 provides a summary of the XRT observations of Mrk 501 in this period (along with those obtained from other MWL data sets): the maximum and mean fluxes, the maximum-to-minimum flux ratio, and the fractional rms variability amplitude in each spectral range. The latter quantity and the associated errors are calculated as (Vaughan et al. 2003)

$$F_{\mathrm{var}} = \left\{ \frac{S^2 - \overline{\sigma^2_{\mathrm{err}}}}{\overline{F}} \right\}^{1/2}, \qquad (2)$$

with S^2, the sample variance; $\overline{\sigma^2_{\mathrm{err}}}$, the mean square error, and $\overline{F}$, the mean flux. Note that the quantities F_{max}, F_{var}, $\overline{F}$, and F_{var} were calculated and presented in Table 5 for three different subintervals of the period 2021 February–2022 December, selected on the basis of the long-term trends as follows:

1. Interval 1a: on average, the source showed a long-term brightening with a progressively rising baseline flux level (see Figure 2(a)). Unfortunately, there was an interruption in the Swift observations during 2021 September 13–November 3 (MJD 59,470–59,521), which prevented observing properly a long-term X-ray flare superimposed on this trend. The latter was also accompanied by shorter-term, lower-amplitude flares. In addition to the different

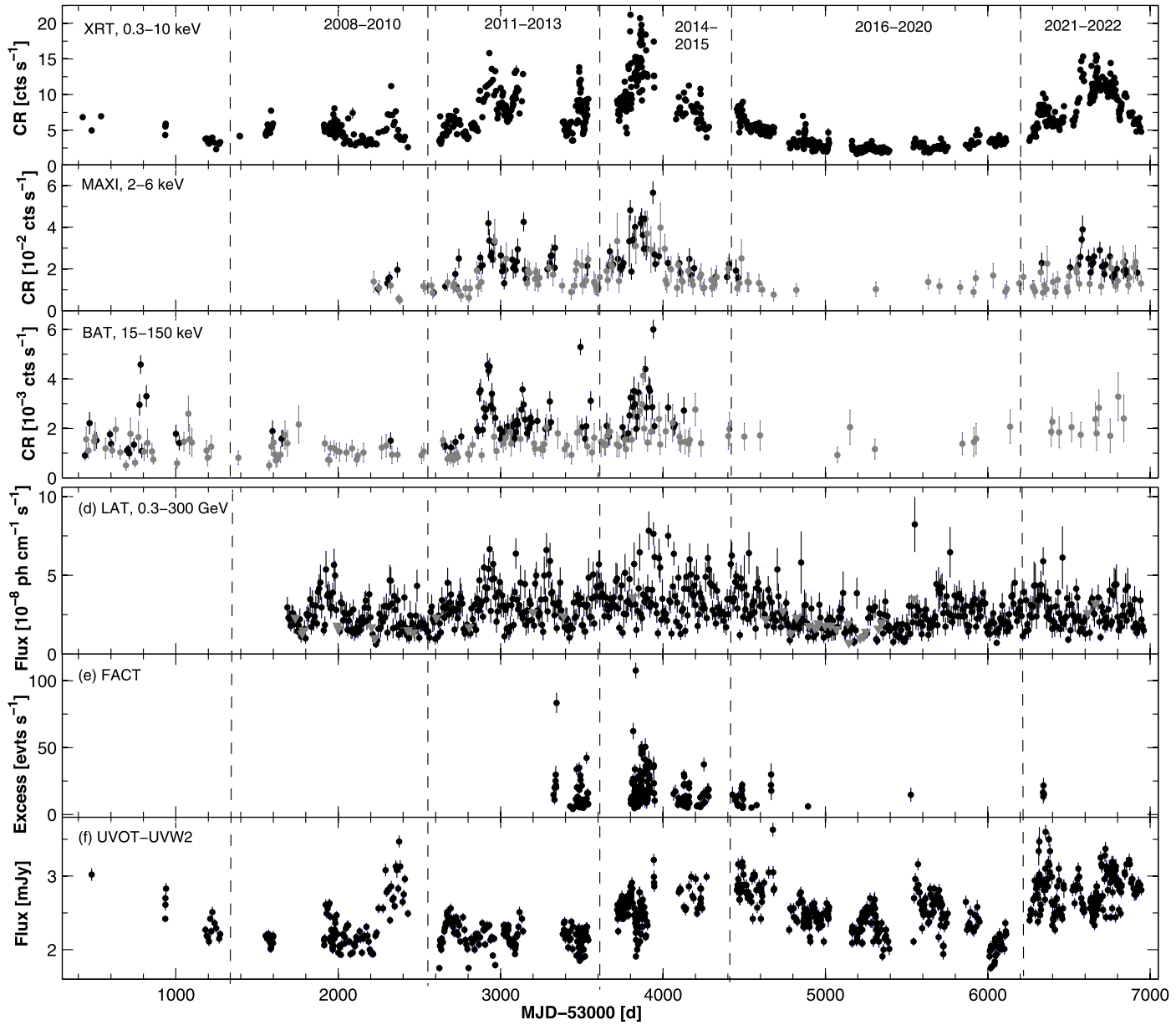

Figure 1. Historical MWL light curves from the observations with different instruments. (a) XRT, (b) MAXI, (c) BAT, (d) LAT, (e) FACT, and (f)–(k) UVOT *UVW2* − *V* bands. While the XRT, FACT, and UVOT data are derived by using the 1 day integration, the BAT, MAXI, and LAT light curves are based on data binned every 2 weeks. In panels (b)–(c), the black and gray data points correspond to the detections of the source with 5σ and 3σ–4σ significances, respectively. In panel (d), the downward gray triangles show the upper limits to the 0.3–300 GeV flux when TS < 9 and/or $N_{\rm pred} < 8$. The vertical dashed line denotes a boundary between the different time intervals listed in Table 1.

durations and amplitudes, these instances showed various flaring profiles (see Section 4.1 for the corresponding physical implications): (a) two flares with fast brightening and significantly slower decline (Figures 3(A1)–(A2))). In such a situation, the flare is classified as a variability instance having positive asymmetry (see, e.g., Chen & Wang 2015). During the second flare, we observed a similar, low-amplitude instance emerging during the flux-decreasing phase (MJD 59,431–59,440); (b) flares with a negative asymmetry—slow brightening and faster decline phases (Figures 3(B1)–(B2)); and (c) two-peak flares (Figures 3(C1)–(C2)).

2. Interval 1b: the maximum epoch, when the baseline flux level showed a plateau-like behavior. Meanwhile, the source underwent consecutive short-term flares with various amplitudes (with a peak flux by 20%–65% higher than the initial flux value). Similar to those in Interval 1a, various flare profiles were recorded: two instances with a positive asymmetry (Figures 3(A3)–(A4)); and three two-peak flares (Figures 3(C3)–(C5)). Note that the first two-peak flare was followed by the 5-weekly interruption in the Swift observations in 2022 January–February (MJD 59,594–59,628), owing to the failed reaction wheel that caused the spacecraft to enter safe mode, suspending the pointed science observations.[15] Moreover, a nearly symmetric variability characterized by similar slopes in the brightness rising and declining phases was also observed (Figure 3(D1)). During some XRT visits to the

[15] See https://swift.gsfc.nasa.gov/news/2022/safe_mode.html.

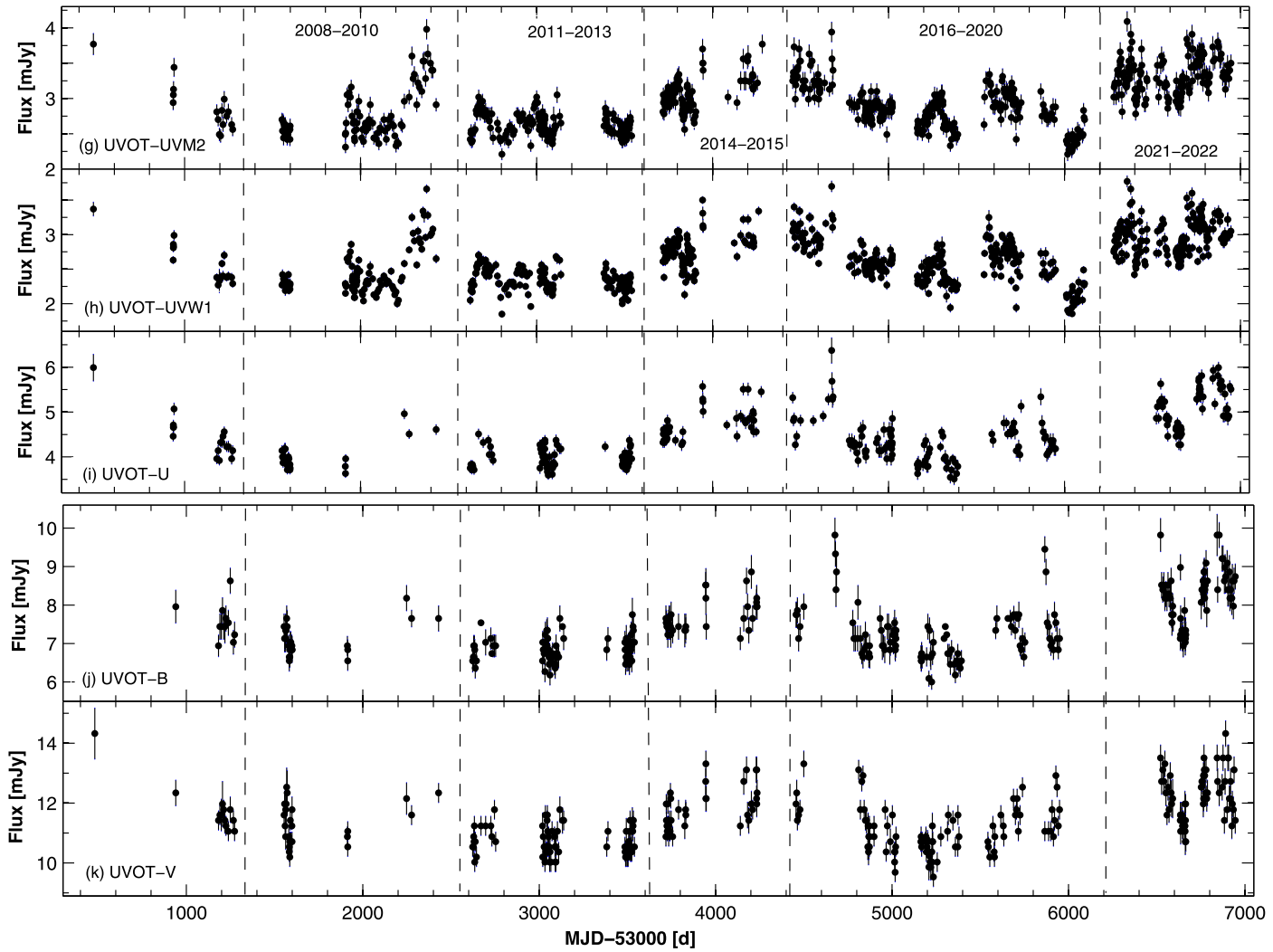

Figure 1. (Continued.)

source, Mrk 501 was revealed to be the brightest blazar in the X-ray sky (in MJD(59)586–587, 662–672, 695–699).

3. Interval 1c: a long-term declining phase of the baseline 0.3–10 keV flux level, which almost dropped to that observed in the start of Interval 1a (Figure 2(a)). This process was accompanied by shorter-term variability showing two instances with two-peak structure (Figures 3(D6)–(D7), lasting about 12–60 days) and by one flare with a nearly symmetric profile Figure 3(D2)).

Finally, Table 5 contains the $F_{\rm max}$, $\overline{F}$, and $F_{\rm var}$ values from the time intervals 2008–2010, 2011–2013, 2014–2015, and 2016–2020 (see Table 1 for the corresponding time ranges), which were selected depending on the long-term 0.3–10 keV activity of the source.

The source was detected most frequently with 5σ significance from 1 week binned MAXI observations in the 2–6 keV band (26 times). However, the $\Re$ and $f_{\rm var}$ values were significantly lower than the 0.3–10 keV "counterparts," most likely owing to the restricted instrumental capabilities of MAXI compared to those of XRT (e.g., the sensitivity of $\sim 2.4 \times 10^{-10}$ erg cm^{-2} s^{-1} of MAXI[16] versus $\sim 10^{-14}$ erg cm^{-2} s^{-1} in the case of XRT; Gehrels et al. 2004). In addition to these data, we also plotted those corresponding to the detections of Mrk 501 with 3σ–4σ significances in Figures 1(b) and 2(b), in order to discern the periods of relatively enhanced hard X-ray activity (29 instances). The majority of the 5σ detections occurred in Interval 1b, in the epoch of the strongest XRT-band activity (see Figure 2(b)). The highest 2–6 keV level was recorded during MJD(5958)1–8, simultaneously with the two-peak short-term flare recorded by XRT in the start of interval 1b. The maximum number of the 3σ–4σ detections occurred in Interval 1a, which was characterized by only two detections of Mrk 501 with 5σ significance.

Figure 1(b) demonstrates that MAXI recorded much stronger hard X-ray activity of the source in the here-presented period than in 2016–2020. On the other hand, Mrk 501 showed even stronger 2–6 keV activity in 2014–2015 (particularly, during the exceptionally strong 0.3–10 keV flare presented in Paper I) and in 2011–2013, characterized by the most frequent 5σ detections[17] (see Table 5 for the corresponding values of the parameters $F_{\rm max}$, $\overline{F}$, and $F_{\rm var}$).

[16] See https://iss.jaxa.jp/en/kiboexp/theme/first/maxi/.

[17] A similar behavior of the source was also recorded throughout the entire 2–20 keV energy range, although with fewer detections with different significances and lower $f_{\rm var}$.

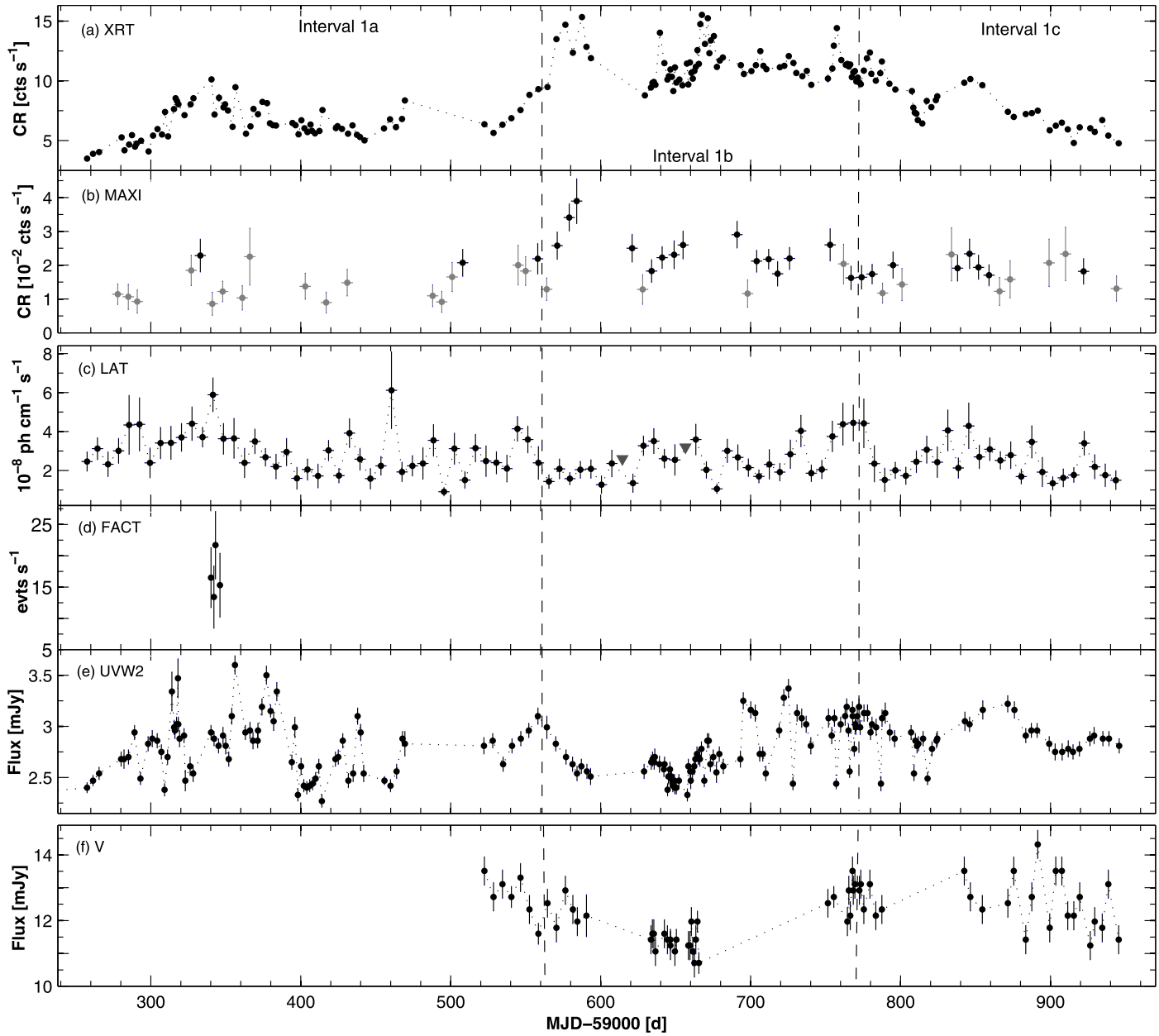

Figure 2. Same as Figure 1 in the subintervals of 2021–2022. Due to the strong correlation between the UVOT-band variabilities (see Section 4.1.2), only the plots from the shortest and longest wavelength bands are presented here.

On the contrary, the source did not show significant activity in the 15–150 keV energy range (see Figure 1(c)): Mrk 501 was not detected at the 5σ confidence level with BAT during 2021–202, and there were only 10 detections with 3σ–4σ significances. However, the source showed strong hard X-ray activity beyond 15 keV in 2011–2015, similar to the MAXI-band observations (see Figure 1(c) and Table 5).

3.1.2. Intraday Variability

The detection of IVD flux variability over timescales shorter than 1 day) is very important, since this nonstationary process can provide constraints on the source structure on linear scales smaller than the solar system (based on the causality arguments; see Wagner & Witzel 1995). Particularly crucial is the study of X-ray IDVs: the emission in this frequency range is widely accepted to be produced the highest-energy electrons. Note that these electrons lose energy very quickly (by synchrotron and IC processes) and exist only close to the sites where they are produced. Therefore, X-ray variability on the shortest timescales allows us to (i) derive the sizes of the inner nuclear regions (not accessible by the direct observations), and (ii) draw conclusions about the kinematics of the jet, and thereby study how the ultrarelativistic particles are accelerated and injected in the emission zone and how efficiently they cool thereafter (see, e.g., Pian 2002).

In order to detect the 0.3–10 keV IDVs from the XRT observations of Mrk 501, we applied the χ^2-test: the source is considered as (i) variable when the null hypothesis (assuming a constant brightness) is rejected with 99.97% confidence, and (b) possibly variable when the rejection significance is 99.5% (Andruchow et al. 2005). Generally, we used 120 s bins for a light-curve construction in this study. For some observations,

Table 4
Summary of the MWL Observations in Interval 1

Band (Units) (1)	F_{max} (2)	$\Re$ (3)	$\overline{F}$ (4)	F_{var} (5)
XRT 0.3–10 keV (counts s^{-1})	15.51(0.14)	6.1(0.2)	8.77(0.01)	0.33(0.01)
XRT 0.3–10 keV (10^{-10} erg cm^{-2} s^{-1})	5.47(0.13)	5.5(0.2)	2.63(0.01)	0.36(0.01)
XRT 0.3–2 keV (10^{-10} erg cm^{-2} s^{-1})	2.72(0.03)	5.1(0.2)	1.45(0.01)	0.33(0.02)
XRT 2–10 keV (10^{-10} erg cm^{-2} s^{-1})	2.83(0.07)	6.9(0.4)	1.19(0.01)	0.38(0.02)
UVOT V (mJy)	14.32(0.43)	1.3(0.1)	12.24(0.05)	0.06(0.01)
UVOT B (mJy)	9.82(0.43)	1.4(0.1)	8.20(0.1)	0.08(0.1)
UVOT U (mJy)	5.99(0.12)	1.4(0.1)	5.08(0.01)	0.09(0.01)
UVOT UVW1 (mJy)	4.09(0.14)	1.5(0.1)	3.27(0.01)	0.09(0.01)
UVOT UVM2 (mJy)	3.77(0.08)	1.6(0.1)	2.91(0.01)	0.09(0.01)
UVOT UVW2 (mJy)	3.60(0.09)	1.8(0.1)	2.75(0.01)	0.09(0.01)
LAT 0.3–300 GeV 2 weeks (10^{-8} ph cm^{-2} s^{-1})	4.43(0.49)	3.1(0.7)	2.55(0.06)	0.26(0.03)
LAT 0.3–300 GeV 1 week (10^{-8} ph cm^{-2} s^{-1})	6.12(1.97)	6.7(2.4)	2.70(0.07)	0.27(0.03)
LAT 0.3–300 GeV 4 days (10^{-8} ph cm^{-2} s^{-1})	6.18(1.28)	4.8(1.9)	2.90(0.07)	0.24(0.03
FACT 1 day (events hr^{-1})	21.7(5.4)	1.6(0.7)	16.55(2.50)	⋯
MAXI 2–6 keV 1 week (10^{-2} counts s^{-1})	3.89(0.66)	2.4(0.6)	2.24(0.08)	0.05(0.01)
MAXI 2–20 keV 1 week (10^{-2} counts s^{-1})	5.53(0.76)	1.9(0.5)	3.69(0.25)	⋯
BAT15–150 keV 1 week (10^{-3} counts s^{-1})	3.28(0.97)	1.9(0.7)	2.20(0.21)	⋯

Note. In each spectral range, the maximum (F_{max}) and mean ($\overline{F}$) fluxes, maximum-to-minimum flux ratio ($\Re$) and fractional variability amplitude (F_{var}) are provided. In the BAT and LAT bands, these quantities are derived using different time bins, while the 1 day bins are adopted for the data obtained with other instruments.

however, we also used the 60 s, 180 s or orbit-binned data when the value of χ^2 was close to the threshold of an IDV detection with the 120 s binning. The results of our study are summarized in Table 6, which consists of the timing and characteristics of each instance (dates, duration, F_{var}, values of the spectral parameters corresponding to the given XRT observation.

Among 58 IDVs detected with 99.97% confidence, the fastest instances detected within the 1 ks XRT exposures are presented in Figure 4. They were characterized by a brightness fluctuation by 10%–34% (taking into account the associated uncertainties) and $f_{var} = 4.4(1.1)\%$–$18.4(3.0)\%$ within 240–960 s. These extreme variabilities occurred in different X-ray states with the observation-binned count rate $\overline{CR} = 3.50(0.08)$–$13.74(0.14)$ counts s^{-1}. The comparable fractional variability amplitudes are found for other subhour instances detected within longer exposures (1.22–3.25 ks; eight instances; see Table 6 for details). During the period presented here, the source also showed 0.3–10 keV variability at the 99.5% confidence level 19 times: 15 instances occurred on subhour timescales and, generally, showed lower fractional amplitudes than the subhour instances detected with the higher significance (see Table 6).

Figure 5 presents the behavior of Mrk 501 during the densely sampled XRT campaigns, which were carried out in Interval 1b. The source did not vary during the first two XRT visits (see Figure 5(a) and Table 2 for the statistics corresponding to each observations). The data set from both visits (with a total time span of about 7.3 ks) shows only a possible variability (see Table 6). Afterwards, the source underwent a gradual decline by 44% in the 95 ks time interval and was variable during the last exposure with 99.97% significance, showing a symmetric profile around the peak moment (the last panel of Figure 5(a)).

A similar behavior was observed during another densely sampled XRT campaign performed in 2022 March 19–27 (Figures 5(b)–(c)): initially, the brightness declined by ∼25% during the 205 ks interval, which was followed by a cycle of the brightening decline with a comparable amplitude within ∼2 days (ObsIDs 96029017–11184185). Afterwards, the source showed the 0.3–10 keV IDVs during ObsIDs 11184186 and 96029019 (with $f_{var} = 4.4(1.0)$–$7.3(1.5)$ and exposures of ∼1 ks). The second instance was followed by an elevated brightness state in about 10 ks (∼50% higher; see the last panel of Figure 5(c)).

Finally, the source showed an interesting behavior during 2022 July 19–23 (Figure 5(c)): while there was a very fast brightening by ∼10% within 600 s during the first observation, the subsequent five XRT visits to the source (with a total time span of about 300 ks) revealed a plateau-like behavior with a mean rate of ∼10 counts s^{-1} and $f_{var} = 4.4(1.0)$.

3.2. X-Ray Spectral Behavior

We performed the 0.3–10 keV spectral analysis using the HEASOFT package XSPEC (v. 12.13.0) and the latest response matrix from the XRT calibration files from the Swift CALDB. The instrumental channels were combined to include at least 20 photons per bin by means of the task GRPPHA, in order to use the χ^2-statistics. By fixing the neutral hydrogen (H I and H_2) column density to the Galactic value of 1.64×10^{20} cm^{-2} (Willingale et al. 2013), each spectrum was first fitted with the log-parabola model (Massaro et al. 2004):

$$F(E) = K(E/E_1)^{-(a+b\log(E/E_1))}, \quad (3)$$

with the reference energy $E_1 = 1$ keV, where a is the photon index at the energy E_1, b is the curvature parameter, and K is the normalization factor. The model validity was checked by means of the distribution of the residuals and the reduced chi-squared (χ^2_r). Using the derived values of the parameters a and b, the position of the synchrotron SED peak was calculated as $E_p = 10^{(2-a)/2b}$ keV (Massaro et al. 2004).[18] Finally, we

[18] Practically the same value of E_p is obtained by means of the XSPEC model EPLOGPAR based on Equation (2) from Tramacere et al. (2007): the difference from that calculated according to Massaro et al. (2004) is significantly lower than the error range. Moreover, this model and LOGPAR (adopted by us within XSPEC) yield the same values of the parameter b.

Table 5
Same as Table 4 for the Different Subintervals of 2021–2022 and the Intervals in 2008–2020

Quantity	Int 1a			Int 1b			Int 1c			2016–2020
	Max	Mean	$F_{\rm var}$	Max	Mean	$F_{\rm var}$	Max	Mean	$F_{\rm var}$	Max
(1)	(2)	(3)	(4)	(5)	(6)	(7)	(8)	(9)	(10)	(11)
CR_{XRT}	10.12(0.11)	6.52(0.01)	0.23(0.01)	15.51(0.14)	11.38(0.02)	0.14(0.01)	12.37(0.02)	8.03(0.02)	0.25(0.01)	8.97(0.15)
$F_{0.3-10\ \rm keV}$	3.23(0.04)	2.03(0.01)	0.24(0.01)	5.47(0.07)	3.72(0.01)	0.20(0.01)	3.72(0.06)	2.41(0.01)	0.26(0.01)	3.37(0.01)
$F_{0.3-2\ \rm keV}$	1.80(0.03)	1.17(0.01)	0.23(0.01)	2.89(0.05)	1.89(0.01)	0.16(0.01)	2.00(0.05)	1.40(0.01)	0.21(0.01)	1.66(0.03)
$F_{2-10\ \rm keV}$	1.47(0.04)	0.86(0.01)	0.26(0.01)	2.98(0.07)	1.73(0.01)	0.27(0.01)	1.74(0.06)	1.02(0.01)	0.32(0.01)	1.73(0.04)
V	13.51(0.43)	12.73(0.14)	⋯	13.51(0.43)	11.91(0.07)	0.05(0.01)	14.32(0.43)	12.54(0.09)	0.05(0.01)	13.11(0.32)
B	9.82(0.43)	8.55(0.12)	⋯	8.98(0.33)	7.81(0.05)	0.07(0.01)	9.82(0.54)	8.71(0.08)	0.04(0.01)	9.82(0.44)
U	5.63(0.12)	5.17(0.04)	0.04(0.01)	5.75(0.13)	4.88(0.02)	0.09(0.01)	5.99(0.12)	5.38(0.03)	0.06(0.01)	7.13(0.24)
*UVW*1	4.09(0.14)	3.27(0.01)	0.07(0.01)	3.91(0.13)	3.31(0.01)	0.08(0.01)	3.80(0.13)	3.43(0.02)	0.04(0.01)	3.94(0.14)
*UVM*2	3.77(0.08)	2.96(0.01)	0.09(0.01)	3.60(0.07)	2.90(0.01)	0.09(0.01)	3.44(0.08)	3.08(0.01)	0.05(0.01)	3.70(0.08)
*UVW*2	3.60(0.09)	2.80(0.01)	0.10(0.01)	3.37(0.09)	2.74(0.01)	0.09(0.01)	3.22(0.08)	2.90(0.01)	0.05(0.01)	3.63(0.09)
$F_{\rm LAT}$	6.12(1.97)	2.92(0.11)	0.27(0.05)	4.38(1.08)	2.46(0.11)	0.26(0.06)	4.44(0.92)	2.56(0.13)	0.25(0.06)	8.23(1.73)
$F_{\rm FACT}$	21.7(5.4)	16.55(2.50)	⋯	⋯	⋯	⋯	⋯	⋯	⋯	29.9(8.09)
$CR_{2-6\ \rm keV}$	2.28(0.49)	2.18(0.26)	⋯	3.89(0.66)	2.30(0.10)	0.20(0.05)	2.34(0.44)	1.89(0.13)	⋯	2.24(0.47)
CR_{BAT}	⋯	⋯	⋯	⋯	⋯	⋯	⋯	⋯	⋯	⋯

Quantity	2016–2020		2014–2015			2011–2013			2008–2010		
	Mean	$F_{\rm var}$	Max	Mean	$F_{\rm var}$	Max	Mean	$F_{\rm var}$	Max	Mean	$F_{\rm var}$
(1)	(2)	(3)	(4)	(5)	(6)	(7)	(8)	(9)	(10)	(11)	(12)
CR_{XRT}	3.38(0.01)	0.41(0.01)	21.20(0.16)	10.74(0.01)	0.36(0.01)	15.82(0.13)	7.32(0.01)	0.35(0.01)	11.20(0.12)	4.88(0.01)	0.30(0.01)
$F_{0.3-10\ \rm keV}$	1.03(0.01)	0.51(0.01)	8.20(0.13)	3.85(0.01)	0.40(0.01)	7.00(0.13)	2.85(0.01)	0.43(0.01)	3.69(0.06)	1.55(0.01)	0.32(0.01)
$F_{0.3-2\ \rm keV}$	0.64(0.01)	0.42(0.01)	3.32(0.03)	1.76(0.01)	0.30(0.01)	2.99(0.05)	1.28(0.01)	0.32(0.01)	2.05(0.07)	0.88(0.01)	0.29(0.01)
$F_{2-10\ \rm keV}$	0.40(0.01)	0.68(0.01)	5.32(0.11)	2.10(0.01)	0.48(0.01)	4.72(0.14)	1.59(0.01)	0.52(0.01)	1.71(0.06)	0.67(0.01)	0.39(0.01)
V	10.99(0.04)	0.06(0.01)	13.31(0.43)	11.85(0.06)	0.05(0.01)	11.78(0.32)	10.72(0.04)	0.03(0.01)	12.53(0.64)	11.29(0.08)	0.05(0.01)
B	7.16(0.03)	0.08(0.01)	8.86(0.43)	7.70(0.05)	0.03(0.01)	7.75(0.33)	6.85(0.05)	0.03(0.01)	8.18(0.33)	7.10(0.06)	0.04(0.01)
U	4.33(0.01)	0.12(0.01)	5.57(0.13)	4.69(0.02)	0.08(0.01)	4.51(0.11)	3.97(0.02)	0.04(0.01)	4.96(0.11)	4.00(0.02)	0.07(0.01)
*UVW*1	2.85(0.01)	0.08(0.01)	3.77(0.13)	3.09(0.01)	0.07(0.01)	3.05(0.11)	2.62(0.01)	0.05(0.01)	3.98(0.14)	2.74(0.01)	0.13(0.01)
*UVM*2	2.56(0.01)	0.10(0.01)	3.50(0.06)	2.80(0.01)	0.08(0.01)	2.70(0.06)	2.34(0.01)	0.07(0.01)	3.66(0.06)	2.43(0.01)	0.14(0.01)
*UVW*2	2.44(0.01)	0.10(0.01)	3.22(0.08)	2.61(0.01)	0.09(0.01)	2.75(0.06)	2.20(0.01)	0.07(0.01)	3.47(0.08)	2.28(0.01)	0.15(0.01)
$F_{\rm LAT}$	2.41(0.04)	0.36(0.02)	7.83(1.20)	3.66(0.08)	0.37(0.02)	6.66(0.85)	3.02(0.06)	0.33(0.02)	5.65(1.02)	2.48(0.06)	0.33(0.03)
$F_{\rm FACT}$	12.31(0.70)	0.48(0.07)	107.6(5.6)	18.77(0.33)	0.68(0.02)	83.40(7.31)	15.74(0.43)	0.83(0.03)	⋯	⋯	⋯
$CR_{2-6\ \rm keV}$	1.95(0.21)	⋯	5.66(0.53)	2.97(0.09)	0.31(0.03)	4.26(0.45)	2.36(0.07)	0.25(0.03)	1.96(0.37)	1.49(0.12)	⋯
CR_{BAT}	⋯	⋯	6.00(0.37)	2.92(0.09)	0.30(0.03)	5.29(0.32)	2.40(0.05)	0.33(0.02)	1.89(0.41)	1.62(0.18)	⋯

Note. The 0.3–10 keV (1 day binned), 2–6 keV (1 week bins; divided by 10^{-2}), and 15–150 keV (1 week bins; divided by 10^{-3}) count rates are given in units of counts s^{-1}; unabsorbed 0.3–10 keV, 0.3–2 keV, and 2–10 keV fluxes—in 10^{-10} erg cm^{-2} s^{-1}; optical–UV fluxes in the bands $V-UVW2$ bands—in millijanskys; LAT-band photon flux—in 10^{-8} ph cm^{-2} s^{-1} (1 week binned); FACT excess rate—in events hr^{-1} (1 day bins).

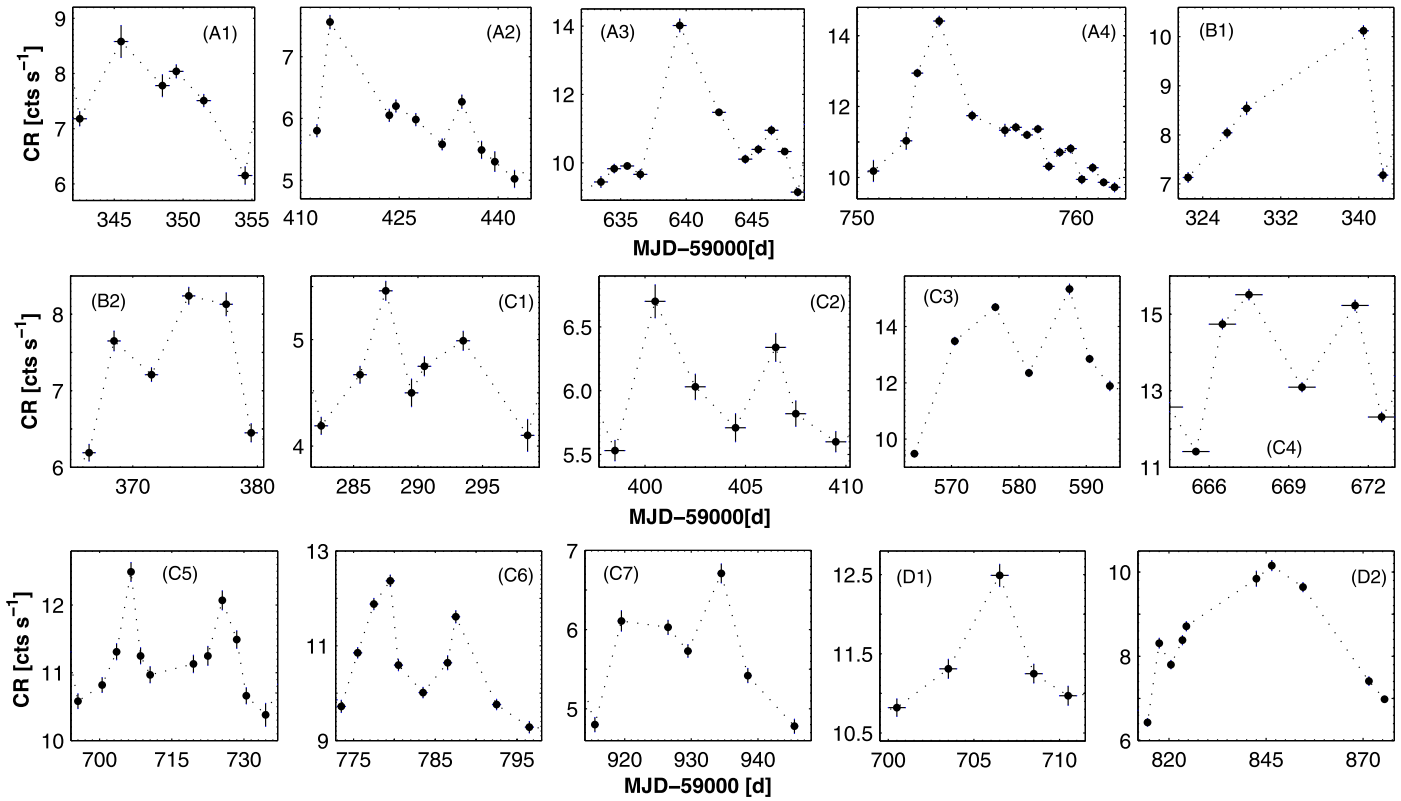

Figure 3. The XRT-band flares of Mrk 501 showing different profiles: fast brightening and slower decline (A), slow brightening and faster decline (B), two-peak (C), and nearly symmetric (D).

Table 6
Summary of the 0.3–10 keV IDVs Detected at the 99.997% and 99.5% Confidence Levels

ObsID(s) (1)	Date(s)/MJD (2)	ΔT(hr) (3)	χ^2/DOF/Bin(s) (4)	F_{var}(%) (5)	a or Γ (6)	b (7)	E_p (keV) (8)
			99.9%				
11184079	2021-02-12/59,257	0.23	5.96/6/120	18.4(3.0)	1.99(0.04)–2.10(0.04)P	…	…
11184082	2021-02-17/59,262	1.78	37.2/1/Or	9.0(1.1)	2.06(0.05) 1.90(0.06)P	0.26(0.12)	0.77(0.13)
11184085	2021-03-14/59,287	0.22	3.58/12/60	10.5(1.9)	1.96(0.04)–1.99(0.04)P	…	…

Note. The third column gives the total length of the particular observation (including the blank intervals between the separate XRT orbits). Columns 6–8 give the ranges of the photon indices ("P" denotes the power-law model; otherwise, the results belong to the photon index a), curvature parameter, and the position of the synchrotron SED peak during the particular IDV, respectively.

(This table is available in its entirety in machine-readable form.)

derived the unabsorbed 0.3–2, 2–10, and 0.3–10 keV fluxes using the tool EDITMOD.

However, when the spectrum showed a curvature with $<2\sigma$ significance, we refitted it using a single power-law model $F(E) = KE^{-\Gamma}$, with Γ, the photon index throughout the observation band. Moreover, we performed an orbit-resolved spectral analysis when the particular XRT observation was distributed over two or more Swift orbits. Generally, the corresponding images (obtained in the WT regime) have different centers, and it is impossible to use the common source and/or background extraction regions. In such a situation, we split the original event file into those corresponding to the particular orbit and performed the aforementioned reduction/analysis steps separately. The same was done even for one-orbit XRT observation when (1) the source showed a 0.3–10 keV IDV; (2) the fit residuals showed some deviations, and therefore no satisfactory fits with any of the model described above were found. Such a situation generally occurs when the spectral parameters undergo a fast change, or there is a transition from the log-parabolic into the power-law spectral distribution of the 0.3–10 keV photons and vice versa.

3.2.1. The Spectral Curvature

Up to 55% of the 0.3–10 keV spectra (248 out of a total of 452) show a significant curvature and are well fitted with the log-parabolic model (see Table 7 for the results). Moreover, Figure 6(A1) presents a histogram constructed with values of the curvature parameter b and the corresponding properties (minimum, maximum, and mean values, and distribution skewness) are listed in Table 8. The distribution peak value was derived by fitting the histogram with the log-normal model

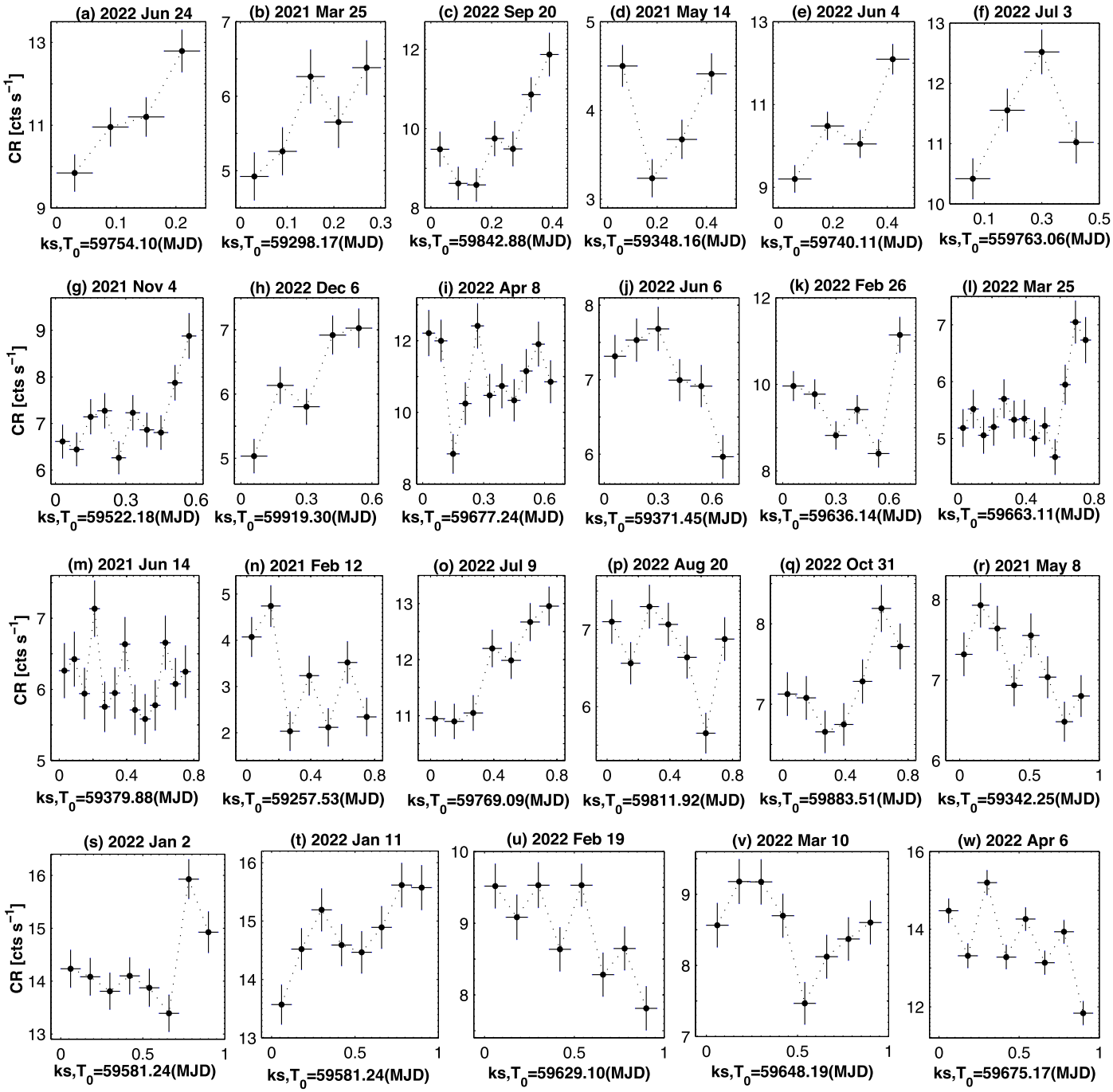

Figure 4. Fastest 0.3–10 keV IDVs detected at the 99.99% confidence level. The instances are arranged in order of increasing observation duration.

or with the beta-distribution in the case of the negative skewness. We see that the source mostly showed a low curvature ($b \sim 0.3$ or lower). Only four spectra showed curvatures with $b > 0.4$ (taking into account the associated errors).

In order to study the statistical properties of the curvature parameter, we also constructed a normalized cumulative distribution of the values. The Kolmogorov–Smirnov (K-S) test was adopted to compare the distributions of the particular parameter in different time intervals (defined in Table 1), and to measure the maximum distance $D_{\mathrm{K-S}}$ between the corresponding normalized cumulative distributions (see Table 9). However, since our samples are not statistically complete, a comparison of the corresponding distributions could be affected by some biases. Namely, there is a risk of obtaining a large $D_{\mathrm{K-S}}$ value between the selected distributions indicating that they are different, simply due to the lack/absence of the data in some bins of each histogram. To check the significance of the K-S test results, the recipe of Massaro et al. (2011) based on Monte Carlo simulations was followed for dealing with this effect and to estimate its relevance: we randomly simulated two distributions for both data sets with the same number of components, adopting two different models for the simulated distributions—log-uniform and log-normal. The former simply has the same maximum and minimum values of the observed distribution, while the latter is spanned over the

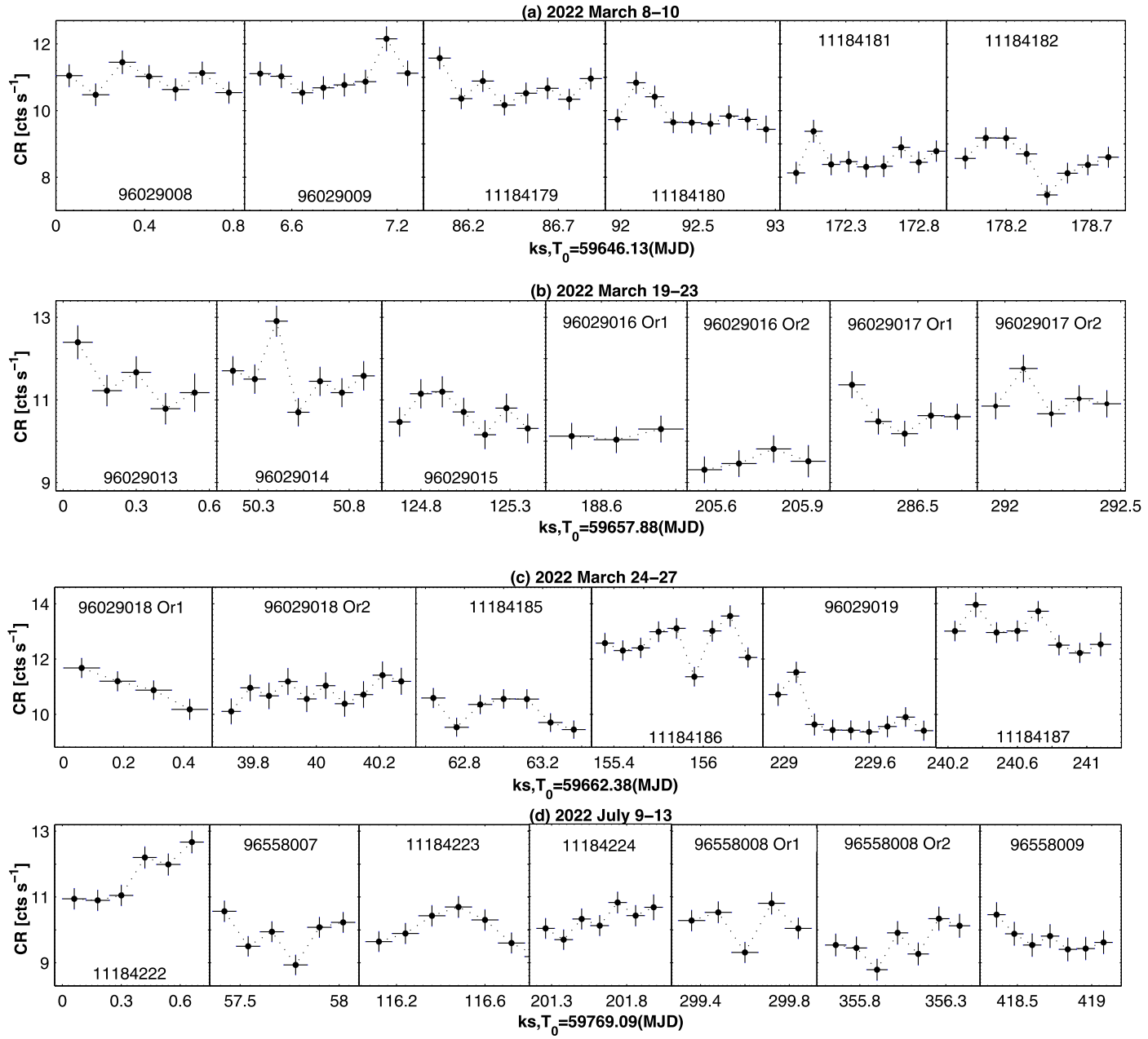

Figure 5. 0.3–10 ke IDVs from the densely sampled XRT observations of Mrk 501.

same range of values and characterized by the same variance and median of the observed distribution. We measured the $D_{\mathrm{K-S,simul}}$ distance between the simulated distributions, repeated simulations at least 30,000 times, and built a distribution of the obtained $D_{\mathrm{K-S,simul}}$. Finally, the probability of obtaining the observed $D_{\mathrm{K-S}}$ randomly was also estimated, which provides the confidence level of the K-S test. However, we did not find any significant difference between the distributions of the curvature parameter values in different parts of Interval 1, as indicated in Table 9 (see also Figures 6(A2)–(A5)). They were characterized by practically the same peak and mean values ($b_{\mathrm{p}} = 0.18$–0.20 and $\overline{b} = 0.23$–0.26, respectively; see Table 8).

Figure 7(c) demonstrates that the parameter b did not show a large variability and, on average, the source was characterized by a relatively low curvature during the flaring X-ray states. This trend is evident in Figure 8(a) where we observe a very weak but statistically significant anticorrelation between the spectral curvature and unabsorbed 0.3–10 keV flux (see Table 10 for the value of the Spearman's correlation coefficient ρ and the corresponding p-chance). Note that this result can be considered in the context of the second-order Fermi acceleration (see the corresponding discussion in Section 4.2.2). However, this relation was held only in Interval 1c with $\rho = 0.47 \pm 0.10$, while it was below the 99% threshold in other intervals, especially, in Interval 1b (see Figure 8(a)). The fastest variability with $\delta b = 0.31(0.11)$ occurred within the 0.3–10 keV IDV during the 0.96 ks XRT observation performed on 2022 March 10 (MJD 56,948; see column 8 of Table 6). Four additional IDV examples of the curvature parameter with $\delta b = 0.17(0.11)$–$0.32(0.12)$ occurred within 2.0–16.1 ks time intervals. Detection of such instances is useful for discerning the underlying unstable physical processes.

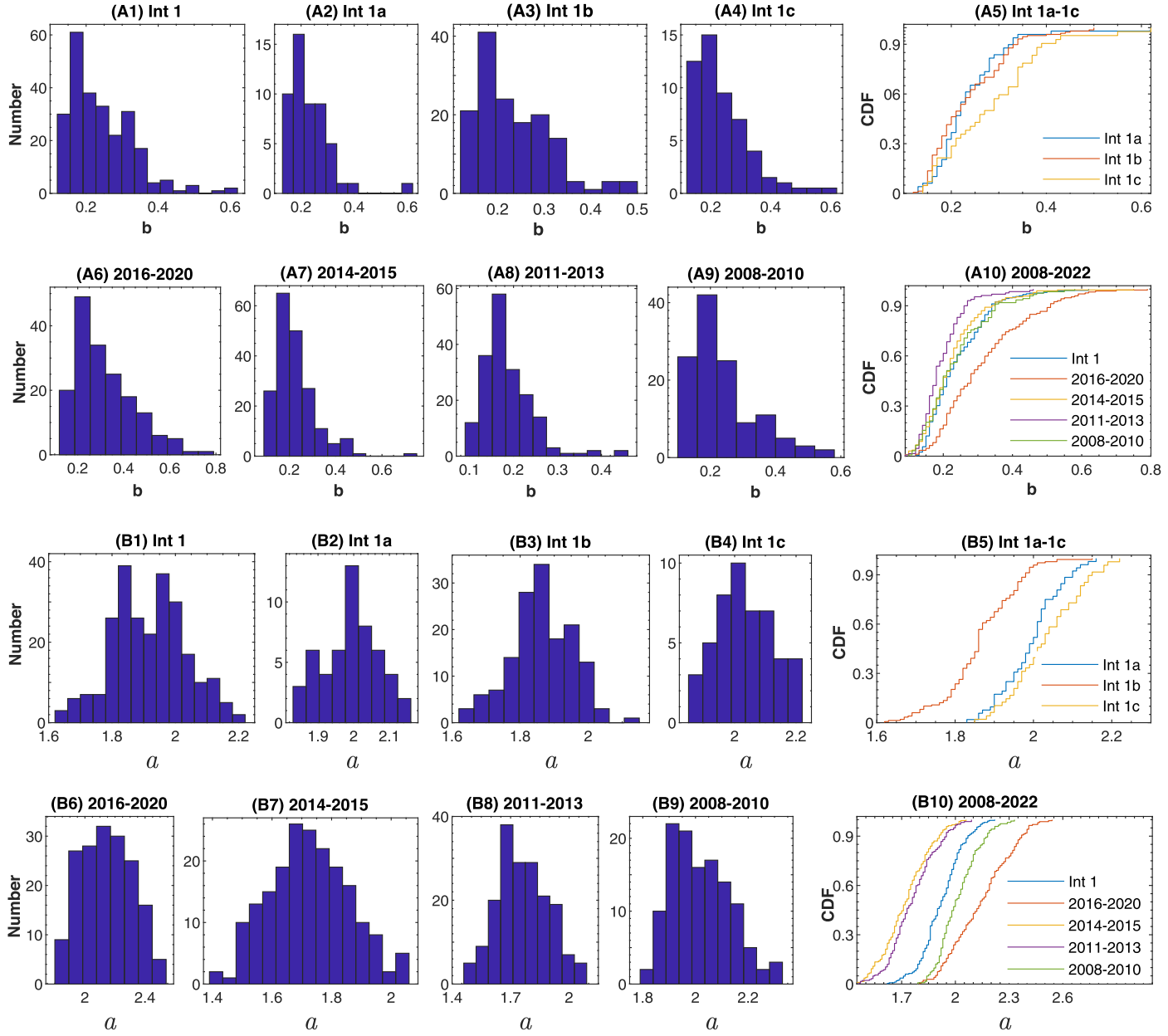

Figure 6. Distribution of spectral parameter values in different time intervals (histograms and corresponding normalized cumulative distribution in the last panel of each row): curvature parameter (panel (A)), photon index at 1 keV (panel (B)), synchrotron SED peak position (panel (C)), and 0.3–10 keV photon index describing the power-law spectra (panel (D)).

Moreover, the curvature parameter also showed a very weak anticorrelation with the position of the synchrotron SED peak, which was statistically significant only in Interval 1a (see Figure 8(b) and Table 10). This parameter showed a relatively strong anticorrelation with the photon index at 1 keV in Interval 1a ($\rho = 0.35 \pm 0.11$), but it was not present in other parts of Interval 1 and, consequently, the scatter plot a–b from the entire period does not show a significant correlation (Figure 8(c)). The physical implications of these relations are discussed below, in the framework of the stochastic acceleration of the X-ray emitting electrons (see Section 4.2.2).

3.2.2. Photon Indices

These curved spectra were characterized by a broad range of the photon index at 1 keV with $\Delta a = 0.60 \pm 0.28$ and the hardest spectrum showing $a_{\rm min} = 1.62 \pm 0.05$. A majority of these spectra are hard ($a < 2$; at least 68%, taking into account the uncertainties) and mostly derived from the XRT observations of Mrk 501 performed in Interval 1b (81.4%). Note that the latter contained all very hard spectra ($a < 1.80$), which amount to at least 9.3% of all curved spectra. Consequently, the distribution of the a values in Interval 1b significantly differs from those in other intervals with the distribution peak $a_{\rm p} = 1.88 \pm 0.01$ versus $a_{\rm p} = 2.00$–2.01 corresponding to Intervals 1a and 1c (see Figures 6(B2)–(B5) and Table 9 for the results from the K-S test). Note also that the mean value in Interval 1b was by $\delta a = 0.14$–0.17 harder than than that those corresponding to other intervals (Table 8). Consequently, the a-histogram constructed for the entire period presented here shows a double-peaked distribution (Figure 6(B1)).

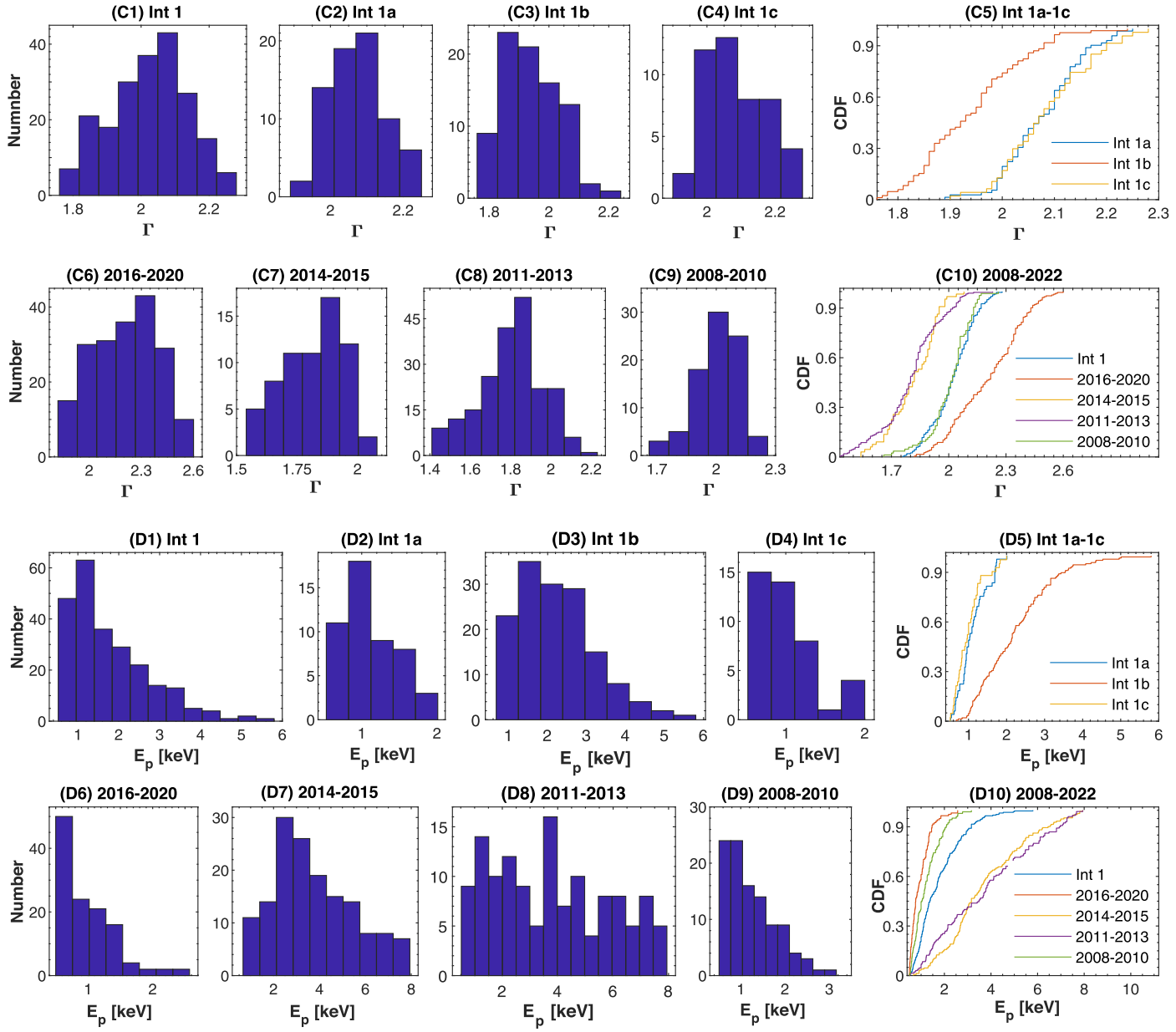

Figure 6. (Continued.)

Table 7
Results of the Swift-XRT Spectral Analysis with the Log-parabolic Model

ObsId (1)	a (2)	b (3)	E_p (4)	$10 \times K$ (5)	χ^2/DOF (6)	$F_{0.3-2\ \mathrm{keV}}$ (7)	$F_{2-10\ \mathrm{keV}}$ (8)	$F_{0.3-10\ \mathrm{keV}}$ (9)
11184082 S1	2.06(0.05)	0.26(0.12)	0.77(0.13)	2.94(0.09)	0.98/106	8.73(0.19)	5.30(0.39)	14.03(0.54)
11184083	2.02(0.04)	0.18(0.09)	0.88(0.11)	2.31(0.06)	1.08/137	6.80(0.13)	4.81(0.28)	11.61(0.37)
11184084	2.01(0.04)	0.19(0.08)	0.94(0.10)	2.59(0.06)	0.97/137	5.36(0.15)	5.36(0.29)	10.72(0.31)

Note. In column 1, the acronyms "Or" and "S" stand for "Orbit" and "Segment," respectively; columns 2–3 present the values of the photon index at 1 keV and the curvature parameter, respectively; the E_p values (column 4) are given in keV; columns 5 and 6 present the norm and the reduced chi-squared (along with the corresponding DOF), respectively; the unabsorbed 0.3–2 keV, 2–10 keV, and 0.3–10 keV fluxes (columns 7–9) are given in units of 10^{-11} erg cm^{-2} s^{-1}.

(This table is available in its entirety in machine-readable form.)

Figure 7(d) demonstrates that the photon index strongly varied on diverse timescales along with unabsorbed 0.3–2 and 2–10 keV fluxes, and the source generally followed a harder-when-brighter spectral evolution (interpreted in the framework of the shock-in-jet model with escape and synchrotron losses; see Section 4.2.2). This spectral trend is reflected in the strong anticorrelation a–$F_{0.3-10\ \mathrm{keV}}$ presented in Figure 8(d). Among the subsamples corresponding to the different intervals, a

Table 8
Distribution of the Spectral Parameter Values in Different Time Intervals

Parameter (1)	Min. (2)	Max. (3)	Mean (4)	Peak (5)	Skew. (6)
			Int 1		
b	0.12(0.06)	0.62(0.11)	0.24(0.01)	0.18(0.01)	1.33
a	1.62(0.05)	2.22(0.05)	1.92(0.01)	⋯	−0.02
E_p	0.24(0.08)	5.80(0.52)	1.79(0.01)	1.35(0.03)	1.14
Γ_{XRT}	1.76(0.03)	2.28(0.03)	2.02(0.01)	2.07(0.01)	−0.18
Γ_{LAT}	1.34(0.13)	2.80(0.28)	1.90(0.01)	1.65(0.02)	1.03
			Int 1a		
b	0.13(0.07)	0.62(0.11)	0.23(0.01)	0.19(0.02)	0.84
a	1.83(0.04)	2.16(0.03)	1.99(0.01)	2.00(0.02)	−0.02
E_p	0.24(0.08)	2.01(0.20)	1.11(0.02)	0.98(0.05)	0.54
Γ_{XRT}	1.89(0.05)	2.25(0.04)	2.08(0.01)	2.08(0.02)	−0.01
Γ_{LAT}	1.43(0.12)	2.80(0.28)	1.94(0.03)	1.76(0.04)	1.00
			Int 1b		
b	0.12(0.06)	0.50(0.09)	0.23(0.01)	0.18(0.01)	1.04
a	1.62(0.05)	2.15(0.03)	1.86(0.01)	1.88(0.01)	−0.12
E_p	0.68(0.11)	5.80(0.52)	2.23(0.02)	1.68(0.04)	0.86
Γ_{XRT}	1.76(0.03)	2.24(0.03)	1.94(0.01)	1.87(0.02)	0.43
Γ_{LAT}	1.34(0.13)	2.69(0.24)	1.82(0.03)	1.71(0.05)	1.16
			Int 1c		
b	0.14(0.07)	0.62(0.13)	0.26(0.01)	0.20(0.01)	1.01
a	1.85(0.04)	2.22(0.05)	2.03(0.01)	2.01(0.02)	0.07
E_p	0.25(0.09)	2.00(0.18)	1.01(0.02)	⋯	0.98
Γ_{XRT}	1.90(0.03)	2.28(0.03)	2.09(0.01)	2.06(0.02)	0.18
Γ_{LAT}	1.48(0.12)	2.51(0.23)	1.92(0.03)	1.70(0.05)	0.75
			2016–2020		
b	0.12(0.06)	0.79(0.26)	0.32(0.01)	0.23(0.01)	0.88
a	1.80(0.07)	2.54(0.05)	2.15(0.01)	2.13(0.01)	0.08
E_p	0.08(0.04)	2.57(0.23)	0.97(0.01)	⋯	1.38
Γ_{XRT}	1.82(0.04)	2.60(0.06)	2.21(0.01)	2.27(0.01)	−0.22
Γ_{LAT}	1.26(0.14)	2.93(029)	1.96(0.01)	1.77(0.01)	0.65
			2014–2015		
b	0.09(0.05)	0.75(0.27)	0.23(0.01)	0.17(0.01)	1.79
a	1.39(0.06)	2.06(0.04)	1.72(0.01)	1.68(0.01)	0.12
E_p	0.67(0.10)	20.86(1.81)	3.76(0.03)	2.85(0.04)	0.51
Γ_{XRT}	1.54(0.02)	2.08(0.04)	1.82(0.01)	1.88(0.01)	−0.37
Γ_{LAT}	1.30(0.15)	2.41(0.25)	1.73(0.01)	1.67(0.02)	0.45
			2011–2013		
b	0.09(0.05)	0.46(0.12)	0.23(0.01)	0.16(0.01)	0.75
a	1.46(0.05)	2.09(0.03)	1.76(0.01)	1.69(0.01)	0.18
E_p	0.85(0.10)	29.43(3.22)	3.79(0.03)	⋯	0.27
Γ_{XRT}	1.41(0.03)	2.23(0.03)	1.80(0.01)	1.86(0.01)	−0.20
Γ_{LAT}	1.25(0.13)	2.93(0.28)	1.80(0.01)	1.50(0.02)	0.83
			2008–2010		
b	0.10(0.05)	0.58(0.23)	0.24(0.01)	0.19(0.01)	1.16
a	1.79(0.04)	2.33(0.03)	2.02(0.01)	1.90(0.01)	0.47
E_p	0.20(0.06)	3.16(0.26)	1.25(0.01)	⋯	0.92
Γ_{XRT}	1.66(0.04)	2.26(0.06)	2.01(0.01)	2.06(0.02)	−0.56
Γ_{LAT}	1.33(0.13)	2.76(0.25)	1.83(0.01)	1.71(0.02)	0.68

Note. The minimum, maximum, mean, and peak values of the particular parameter are provided in columns (2), (3), (4), and (5), respectively; the distribution skewness is given in the last column. The position of the synchrotron SED peak is presented in keV.

harder-when-brighter trend was the weakest in Period 1a with $\rho = 0.31 \pm 0.11$ versus $\rho = 0.65 \pm 0.07$ derived from Interval 1b, with the intermediate situation in the third interval (see Table 10). Note that Interval 1a was characterized by interruption of this trend by the opposite spectral evolution during the time interval of 2–29 days (the longest one occurring in MJD 59,381–59,400; see Figure 7(a) and Table 7), as well as by unclear trends on some occasions. Note that such instances have an important physical implication (as discussed below). They were less-pronounced in Interval 1b and occurred mainly on the intraday timescales.

During the 0.3–10 keV flares, the largest variabilities of the photon index were the hardening by $\delta a = 0.44(0.06)$ and softening by $\delta a = 0.34(0.06)$ during MJD(555)35–87 and (597)54–71, respectively. Finally, the parameter a frequently was variable during the 0.3–10 keV IDVs by $\delta a = 0.08(0.04)$–$0.21(0.06)$ during 0.23–23.8 hr (see column 6 of Table 6). Note that the largest IDV of the photon index represented a hardening to $a = 1.67 \pm 0.05$ (one of the hardest spectra in the period presented here), which occurred during the very fast IDV shown in Figure 4(v). Such changes in the spectral hardness or very fast transition from the curved into the power-law shape (or vice versa) are very useful for drawing conclusions about the particle acceleration mechanisms and jet unstable processes (as presented in Section 4.2).

More than 45% of the 0.3–10 keV spectra of Mrk 501 did not show significant curvatures (the detection significance of 1σ or lower) and were well fitted with a simple power law, yielding a range of the 0.3–10 keV photon index which was comparable to that of the index a ($\Delta\Gamma = 0.52 \pm 0.04$ with the hardest value $\Gamma_{min} = 1.76 \pm 0.03$; see Table 11). However, Figure 8(C1) demonstrates that the photon index Γ was characterized by a significantly softer distribution then its "counterpart" from the curved spectra: at least 56.2% show $\Gamma \geqslant 2$ (versus 14.8% for the log-parabolic spectra) and the peak value $\Gamma_p = 2.07 \pm 0.01$. The softest power-law spectra were observed in Intervals 1a and 1c with $\overline{\Gamma} = 2.08$–2.09 and $\Gamma_p = 2.06$–2.08 (Figures 6(C2) and (C4)). On the contrary, Interval 1b was notable for (i) significantly harder power-law spectra ($\overline{\Gamma} = 1.86$ and $\Gamma_p = 1.88$; see also Figure 6(C2) and Table 9 for the normalized cumulative distributions and the results of the K-S test, respectively); (ii) the lowest percentage of power-law spectra (36.2% versus 50%–58% in Intervals 1a and 1c).

According to Figure 7(d), the source showed the power-law spectra in any X-ray state recorded during Interval 1. On many occasions, there was a change from the log-parabolic into the power-law energy distribution or vice versa for the spectra extracted from the different segments of the particular XRT observation of Mrk 501, corresponding to the different Swift orbits. The same occurred frequently also for the spectra extracted from 150–600 s segments of some single-orbit observation. For example, the observation MJD 11184188 represents one of the extreme cases: the spectra from the first, second, and fourth segments (each of 195 s duration) were curved with $a = 1.62(0.05)$–$1.79(0.05)$, $b = 0.20(0.09)$–$0.30(0.09)$, and $E_p = 3.35(0.34)$–$4.34(0.45)$ keV, while those from the second and fifth segments are well fitted with a single power law, yielding $\Gamma = 1.81(0.04)$–$1.82(0.03)$.

The power-law spectra also showed a harder-when-brighter variability with the same strength as did the curved "counterparts" (see Figure 8(e) and Table 10). Similar to the curved

Table 9
Results from the K-S Test

	K-S							D_{KS}						
Par.	Int 1a vs Int 1b	Int 1a vs Int 1c	Int 1b vs Int 1c	Int 1 vs 2016–2020	Int 1 vs 2014–2015	Int 1 vs 2011–2013	Int 1 vs 2008–2010	Int 1a vs Int 1b	Int 1a vs Int 1c	Int 1b vs Int 1c	Int 1 vs 2016–2020	Int 1 vs 2014–2015	Int 1 vs 2011–2013	Int 1 vs 2008–2010
(1)	(2)	(3)	(4)	(5)	(6)	(7)	(8)	(9)	(10)	(11)	(12)	(13)	(14)	(15)
b	0	0	0	1	0	1	0	⋯	⋯	⋯	0.26	⋯	0.28	0
a	1	0	1	1	1	1	1	0.55	⋯	0.62	0.54	0.59	0.52	0.33
Γ	1	0	1	1	1	1	0	0.65	⋯	0.60	0.50	0.66	0.59	⋯
E_p	1	0	1	1	1	1	1	0.62	⋯	0.66	0.44	0.55	0.61	0.27

Note. The acronym "vs" in the column titles stands for "versus." In columns (2)–(8), the symbol "1" indicates that data sets are different from each other, and the corresponding maximum distance between the normalized cumulative distributions are provided in columns (9)–(15); "0"—no significant difference between the data sets.

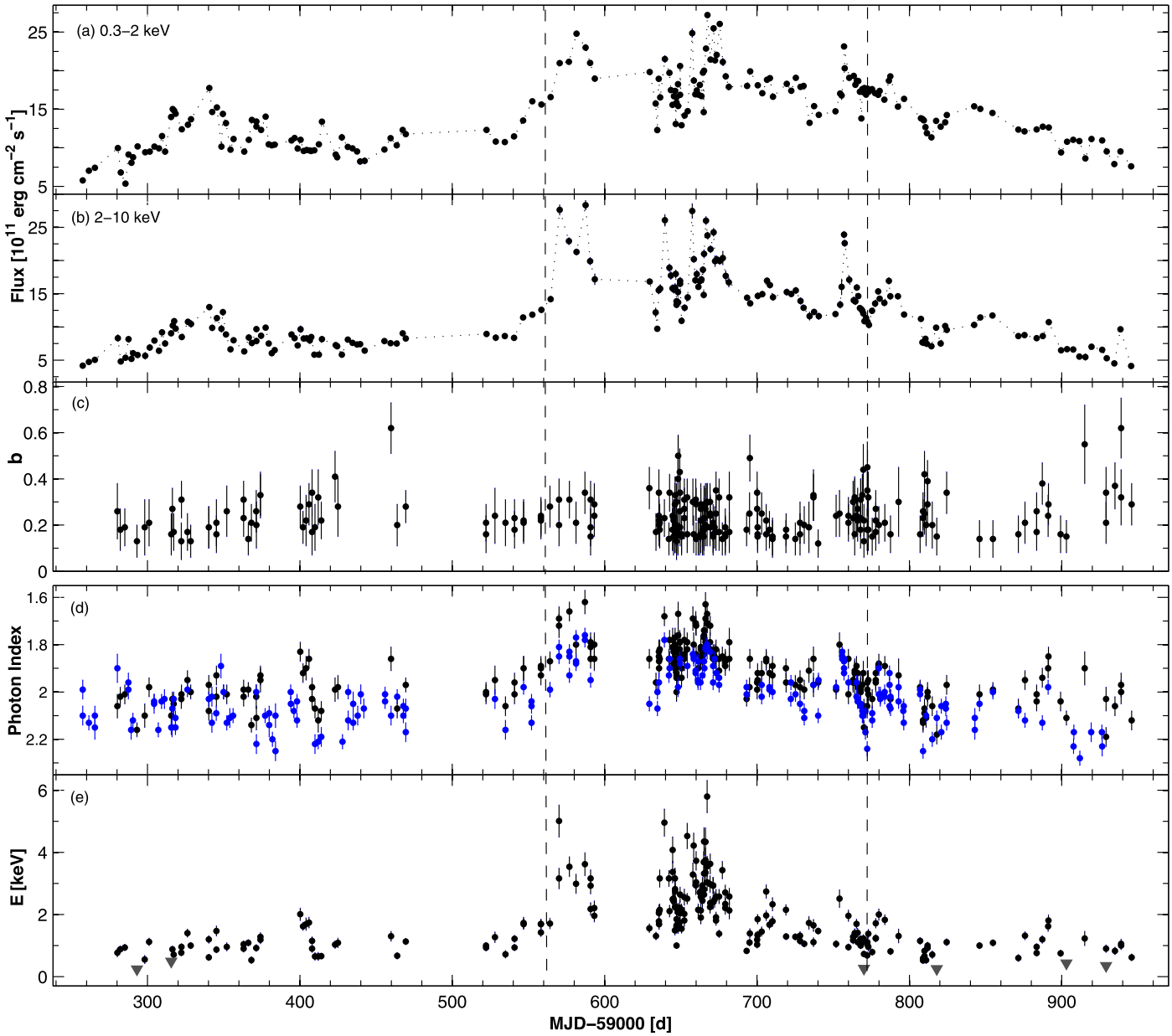

Figure 7. Unabsorbed fluxes and spectral parameters plotted vs. time. (a) 0.3–2 keV flux, (b) 2–10 keV flux, (c) curvature parameter, (d) photon index at 1 keV (black points) and the 0.3–10 keV photon index (blue points), and (e) position of the synchrotron SED peak. The Intervals presented in Section 3.1.1 are located between the vertical dashed lines. The downward gray triangles in the bottom panel indicate the upper limit to the intrinsic position of the synchrotron SED peak. The vertical dashed lines represent the boundaries between Intervals 1a, 1b, and 1c.

spectra, this trend was significantly weaker in Interval 1a, compared to other intervals (see Table 10). The photon index varied by $\delta\Gamma = 0.08(0.04)$–$0.15(0.04)$ during the 0.3–10 keV IDVs 12 times (see column 6 of Table 6). On longer timescales, the largest variabilities were a softening by $\delta\Gamma = 0.41(0.05)$ during MJD(597)56–72 and hardening by $\delta\Gamma = 0.40(0.05)$ (MJD 59,535–59,587; see Figure 7(d)), to be comparable to those observed for the curved spectra during Interval 1 and indicating a large variability in the strength of the acceleration mechanisms.

3.2.3. The Position of the Synchrotron SED Peak

Curved spectra showed a broad range of the synchrotron SED peak position between $E_p = 0.24 \pm 0.08$ keV and $E_p = 5.80 \pm 0.52$ keV. However, the spectra with $E_p < 0.5$ keV are poorly or not constrained by the observational data, and such E_p values (six instances) should be considered as upper limits to the intrinsic position of the synchrotron SED peak (see e.g., Kapanadze et al. 2020). Therefore, these values were not used by us for the construction of the scatter plots (Figures 8(c), (f), and (g)) and histograms presented in Figures 8(D1)–(D5).

At least 73 spectra (31.6% of the spectra with a secure detection of E_p) showed the synchrotron SED peak position in the hard X-ray range (i.e., $E_p > 2$ keV). All of these instance are concentrated in Interval 1b, which was characterized by the mean and peak values of 2.23 ± 0.02 keV and 1.68 ± 0.04 keV, respectively. In other intervals, these values were much lower: 1.01–1.11 keV and 0.95–0.98 keV, respectively.

Generally, the target showed a trend of shifting SED peak to higher frequencies and vice versa, which was demonstrated in a

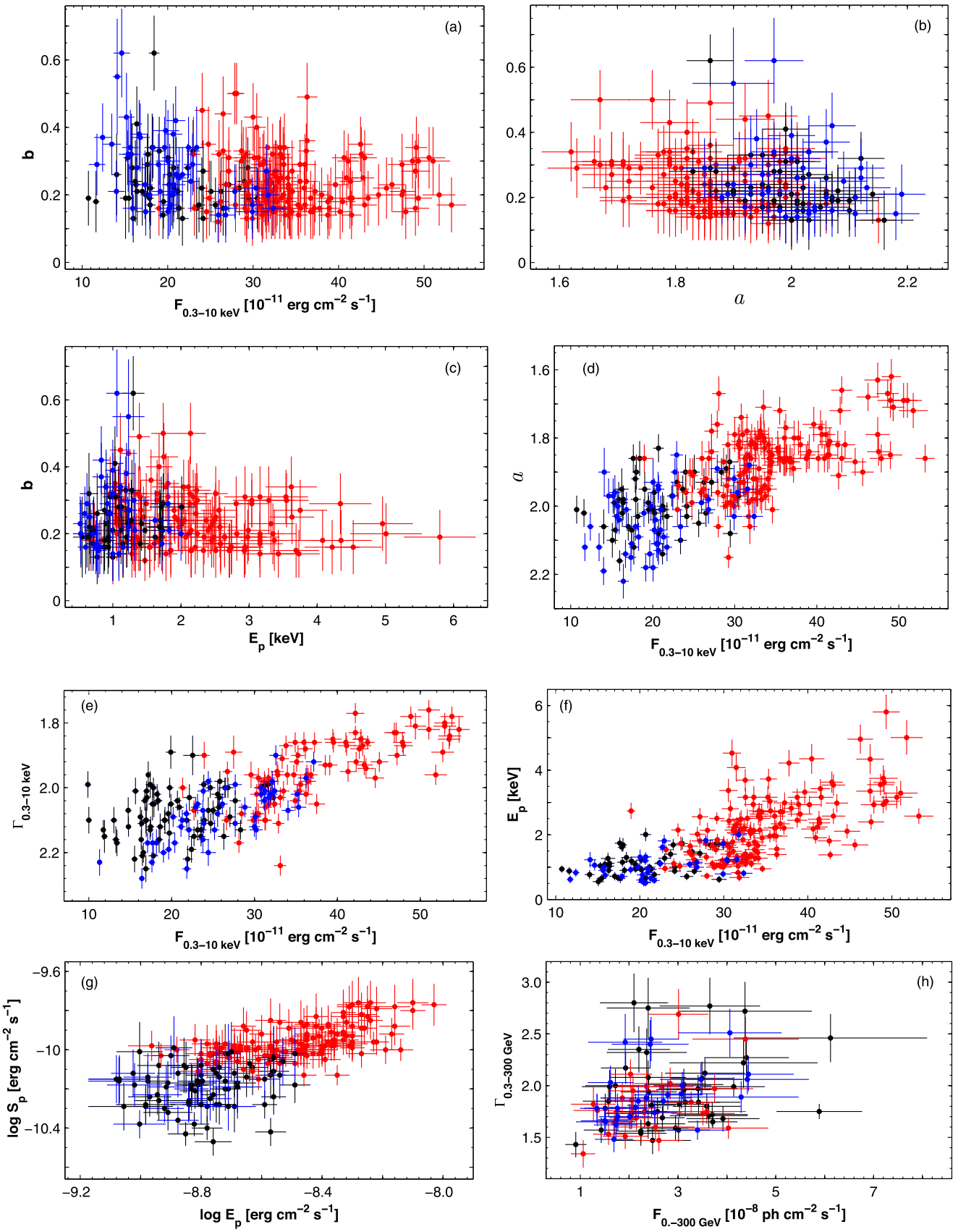

Figure 8. Correlation between the spectral parameters and MWL fluxes. (a)–(c) Curvature parameter b plotted vs. the unabsorbed 0.3–10 keV flux, the photon index a and the position of the synchrotron SED peak E_p, respectively. Parameters a and E_p are plotted vs. the unabsorbed 0.3–10 keV flux in panels (d)–(e). The scatter plot E_p–log S_p is presented in panel (f). The 0.3–10 keV photon index from the power-law spectra is plotted vs. the unabsorbed 0.3–10 keV flux in panel (g); the scatter plot with the LAT-band photon index and photon flux (1-weekly integration) is presented in the last panel. The black, red, and blue points correspond to the data from Intervals 1a, 1b, and 1c, respectively.

Table 10
Correlations between Spectral Parameters and MWL Fluxes in Different Time Intervals

Quantities	ρ	p
	Int 1	
b and $F_{0.3-10\ \mathrm{keV}}$	−0.22(0.12)	8.7×10^{-3}
b and E_{p}	−0.21(0.12)	2.5×10^{-3}
a and $F_{0.3-10\ \mathrm{keV}}$	−0.72(0.06)	4.0×10^{-13}
Γ and $F_{0.3-10\ \mathrm{keV}}$	−0.73(0.05)	1.1×10^{-13}
E_{p} and $F_{0.3-10\ \mathrm{keV}}$	0.73(0.07)	6.6×10^{-12}
$\log E_{\mathrm{p}}$ and $\log S_{\mathrm{p}}$	0.69(0.07)	8.7×10^{-13}
$\Gamma_{0.3-300\ \mathrm{GeV}}$ and $F_{0.3-300\ \mathrm{GeV}}$	0.34(0.11)	9.9×10^{-4}
	Int 1a	
a and b	−0.35(0.11)	7.0×10^{-5}
a and $F_{0.3-10\ \mathrm{keV}}$	−0.31(0.11)	8.8×10^{-3}
Γ and $F_{0.3-10\ \mathrm{keV}}$	−0.30(0.11)	5.6×10^{-3}
	Int 1b	
b and E_{p}	−0.27(0.12)	1.7×10^{-3}
a and $F_{0.3-10\ \mathrm{keV}}$	−0.65(0.07)	3.6×10^{-12}
E_{p} and $F_{0.3-10\ \mathrm{keV}}$	0.59(0.08)	1.4×10^{-9}
$\log E_{\mathrm{p}}$ and $\log S_{\mathrm{p}}$	0.58(0.08)	2.5×10^{-10}
Γ and $F_{0.3-10\ \mathrm{keV}}$	−0.74(0.06)	7.3×10^{-15}
	Int 1c	
b and $F_{0.3-10\ \mathrm{keV}}$	−0.47(0.10)	5.5×10^{-5}
a and $F_{0.3-10\ \mathrm{keV}}$	−0.41(0.09)	6.2×10^{-8}
E_{p} and $F_{0.3-10\ \mathrm{keV}}$	0.43(0.12)	5.4×10^{-4}
Γ and $F_{0.3-10\ \mathrm{keV}}$	−0.75(0.06)	9.6×10^{-10}
	2016–2020	
b and $F_{0.3-10\ \mathrm{keV}}$	−0.48(0.09)	1.8×10^{-8}
a and b	−0.27(0.11)	2.1×10^{-3}
b and E_{p}	−0.27(0.11)	7.7×10^{-4}
a and $F_{0.3-10\ \mathrm{keV}}$	−0.55(0.08)	5.7×10^{-10}
Γ and $F_{0.3-10\ \mathrm{keV}}$	−0.70(0.06)	1.4×10^{-12}
$\log E_{\mathrm{p}}$ and $\log S_{\mathrm{p}}$	0.30(0.12)	8.0×10^{-4}
E_{p} and $F_{0.3-10\ \mathrm{keV}}$	0.35(0.11)	6.2×10^{-4}
$\Gamma_{0.3-300\ \mathrm{GeV}}$ and $F_{0.3-300\ \mathrm{GeV}}$	0.30(0.11)	1.7×10^{-4}
	2014–2015	
b and E_{p}	−0.32(0.12)	2.8×10^{-4}
a and $F_{0.3-10\ \mathrm{keV}}$	−0.73(0.06)	8.9×10^{-14}
Γ and $F_{0.3-10\ \mathrm{keV}}$	−0.80(0.04)	6.5×10^{-14}
E_{p} and $F_{0.3-10\ \mathrm{keV}}$	0.61(0.08)	2.3×10^{-10}
$\log E_{\mathrm{p}}$ and $\log S_{\mathrm{p}}$	0.66(0.08)	2.1×10^{-12}
$\Gamma_{0.3-300\ \mathrm{GeV}}$ and $F_{0.3-300\ \mathrm{GeV}}$	0.32(0.11)	3.6×10^{-4}
	2011–2013	
b and E_{p}	−0.23(0.12)	1.7×10^{-3}
a and $F_{0.3-10\ \mathrm{keV}}$	−0.79(0.05)	2.3×10^{-15}
Γ and $F_{0.3-10\ \mathrm{keV}}$	−0.81(0.04)	1.1×10^{-15}
E_{p} and $F_{0.3-10\ \mathrm{keV}}$	0.74(0.07)	3.7×10^{-12}
$\log E_{\mathrm{p}}$ and $\log S_{\mathrm{p}}$	0.74(0.07)	1.3×10^{-13}
	2008–2010	
b and $F_{0.3-10\ \mathrm{keV}}$	−0.30(0.11)	4.8×10^{-4}
b and E_{p}	−0.38(0.12)	7.1×10^{-5}
b and a	0.28(0.12)	3.1×10^{-3}
a and $F_{0.3-10\ \mathrm{keV}}$	−0.30(0.12)	6.3×10^{-4}
Γ and $F_{0.3-10\ \mathrm{keV}}$	−0.43(0.09)	4.9×10^{-5}
$\log E_{\mathrm{p}}$ and $\log S_{\mathrm{p}}$	0.27(0.13)	6.2×10^{-3}
E_{p} and $F_{0.3-10\ \mathrm{keV}}$	0.34(0.12)	4.4×10^{-4}

Note. In columns (2)–(3), ρ and p stand for the Spearman correlation coefficient and the corresponding p-chance, respectively.

strong positive correlation between E_{p} and unabsorbed 0.3–10 keV flux (see Figure 8(f) and Table 10). This trend (expected by injection of high-energy particles in the shock acceleration process and demonstrating a general dominance of synchrotron cooling of the highest-energy electrons over the IC cooling; see below) was particularly evident in Interval 1b: the hardest values of the parameter E_{p} correspond to the highest 0.3–10 keV states (see Figure 7(e)). On the contrary, the significance of the correlation E_{p}–$F_{0.3-10\ \mathrm{keV}}$ was slightly lower than 99% in Interval 1a.

Similar to other spectral parameters, the synchrotron SED peak position was variable on diverse timescales: the last column of Table 6 shows changes by $\delta E_{\mathrm{p}} = 0.28(0.15)$–$2.25(0.61)$ during 27 IDVs and there was a shift by at least 0.97 keV during that recorded within ObsIDs 96558007–11184223, since the lowest value of 0.26 keV extracted from the first segment of ObsID 11184223 represents an upper limit to the intrinsic position of the synchrotron SED peak. As for the long-term variability, the most dramatic variability was observed in MJD(596)63–75 when E_{p} shifted by 3.90(0.56) keV to higher energies, which was followed by a shift by 4.42(0.53) keV to the opposite direction (Figure 7(e)). This result show extreme changes in the X-ray emission zone of Mrk 501 (as discussed in Section 4.2.4).

3.3. Gamma-Ray and Optical-to-UV Emissions

Generally, Mrk 501 is not a bright LAT-band source and, therefore, we used the 8-weekly integration in order to obtain significant detections for the vast majority of the time bins (98%). Only two bins (centered on MJD 59,615.5 and 59,657.5) showed the detection significance below the 3σ threshold, and we calculated the upper limits to the 0.3–30 GeV flux in those cases. When adopting the narrower 4 day and 3 day integration, the significant detection percentage drops to 84% and 61%, respectively.

The 1 week binned historical LAT-band light curve is presented in Figure 1(d): in contrast to the 0.3–10 keV energy range, we do not observe a strong long-term γ-ray flare in the source during Interval 1, and the mean 0.3–300 GeV photon flux of $(2.70 \pm 0.07) \times 10^{-8}$ ph cm^{-2} s^{-1} was lower than in the intervals 2011–2013 and 2014–2015 ($(3.02–3.66) \times 10^{-8}$ ph cm^{-2} s^{-1}) and slightly higher than in 2008–2010 and 2016–2020 ($(2.41–2.48) \times 10^{-8}$ ph cm^{-2} s^{-1}; see Tables 4–5). On the other hand, the HE variability was stronger than that observed in the BAT and MAXI bands. The source showed only a moderate flaring behavior on various timescales in Intervals 1a–1c (Figure 2(c)). The highest flux of $(1.25 \pm 0.40) \times 10^{-7}$ ph cm^{-2} s^{-1} corresponds to the 1 day binned 0.3–300 GeV data collected with LAT on 2021 September 29 (MJD 59,476).

The source was detected only four times by FACT with a significance of 3σ and higher in the TeV energy range, showing no significant variability (during MJD(593)40–46; see Figure 2(e) and Table 4). These detections were coeval with the short-term 0.3–10 keV flare presented in Figure 3(B1) and the corresponding excess rates were much lower than those recorded in the epochs of the strong 0.3–10 keV flares observed in 2012–2015 (see Figure 1(e)). However, note that the FACT data of Mrk 501 are not available before MJD 59,340 and after MJD 59,469, owing to the volcanic activities at La Palma and related consequences in the latter case (D. Dorner 2023, private communication). Note that the aforementioned detections correspond to higher VHE states, than the FACT detections of Mrk 501 and VHE fluxes from 1 week binned MAGIC data collected during MJD 57,754–59,214 (in 2017 November–

Table 11
Results of the XRT Spectral Analysis with a Simple Power-law Model

ObsId (1)	Γ (2)	$10 \times K$ (3)	χ^2/DOF (4)	$F_{0.3-2\ \mathrm{keV}}$ (5)	$F_{2-10\ \mathrm{keV}}$ (6)	$F_{0.3-10\ \mathrm{keV}}$ (7)
11184079 S1	2.10(0.04)	2.01(0.07)	1.03/67	6.25(0.27)	3.75(0.29)	10.00(0.33)
11184079 S2	1.99(0.04)	1.75(0.07)	1.13/65	5.30(0.25)	4.59(0.32)	9.89(0.34)
11184080	2.13(0.03)	2.23(0.05)	1.03/114	7.03(0.19)	4.72(0.22)	11.75(0.27)

Note. The value of the 0.3–10 keV photon index is provided in column 2; columns 3 and 4 present the norm and the reduced chi-squared, respectively; the unabsorbed 0.3–2 keV, 2–10 keV, and 0.3–10 keV fluxes (columns 5–7) are given in units of 10^{-11} erg cm^{-2} s^{-1}.

(This table is available in its entirety in machine-readable form.)

Table 12
Results from the LAT Observations in the 100–500 GeV Energy Range

Interval (1)	TS (2)	N_{pred} (3)	Flux (4)	Γ (5)
Int 1	58.0	6.0	1.15*	...
Int 1a	57.9	5.0	1.50*	...
Int 1b	0	0	...	...
Int 1c	33.3	2.0	1.05*	...
2016–2020	139.3	10.0	0.54(0.09)	3.20(0.79)
2014–2015	221.9	16.0	2.60(0.35)	2.25(0.18)
2011–2013	387.7	27.4	2.89(0.31)	2.09(0.14)
2008–2010	222.3	15.3	1.83(0.28)	2.74(0.24)

Note. Columns 2 and 3 give the test statistics and the number of the model-predicted photons, respectively; the 100–500 GeV photon flux (in units of 10^{-10} ph cm^{-2} s^{-1}) and photon index are provided in Columns 4 and 5, respectively. The symbol "*" denotes the 2σ upper limit to the 100–500 GeV photon flux.

2020 December), in the epoch of the lowest X-ray and γ-ray activity reported by Abe et al. (2023).

We also processed and analyzed the LAT observations of Mrk 501 in the separate 100–500 GeV energy range (see Table 12 for the results). Although the test statistics showed the target's VHE detection with a significance of about 7.5σ when performing the integration throughout the entire Interval 1, the number of the model-predicted photons was lower than the threshold adopted for the credible detection. Therefore, we calculated the 2σ upper limit to the 100–500 GeV photon flux. We did the same study in the particular Intervals 1–3, intending to discern the epoch of a relatively enhanced VHE activity. However, the source was not detectable at all in Interval 1b, which was notable with the highest X-ray states in the period presented here. Since the parameter TS was practically equal to zero, we were nor able to calculate even the upper limit to the VHE flux. As for the other intervals, the source was relatively active in Interval 1a with an upper limit to the 100–500 GeV flux almost 50% higher than that in Interval 1c. On the contrary, the source was securely detectable in this energy range yielding $F_{100-500\ \mathrm{GeV}} = (0.54\text{–}2.89) \times 10^{-10}$ ph cm^{-2} s^{-1} in the intervals of the period 2008–2020 defined in Table 1, with the lowest and highest fluxes in 2016–2020 and 2011–2013, respectively. Note that the 100–500 GeV flux in the interval 2014–2015 was comparable with the highest one.

The source was observed most frequently in the *UVW2* band with UVOT (193 visits), and a comparable number of pointings was performed in the other two UV bands. However, the UVOT observations were significantly fewer in the optical bands (64–68). Figures 1(f)–(k) demonstrate that, on average, Mrk 501 showed higher optical–UV states in Interval 1 than in the period 2008–2020 (e.g., $\overline{F}_{UVW2} = 2.75(0.01)$ versus $\overline{F}_{UVW2} = 2.20(0.01)$–$2.61(0.01)$). Nevertheless, a similar result is obtained in the *V*–*U* bands in such a situation that the source was not observed with UVOT in most of Interval 1b, in the epoch of the highest UV states (Figures 2(e)–(f)). Consequently, the highest historical states in these bands do not coincide with Interval 1, in contrast to the UV frequencies (see Tables 4–5). However, the variability strength was not the highest in the bands $U - UVW2$ ($F_{\mathrm{var}} = 0.09(0.01)$ in each, against $F_{\mathrm{var}} = 0.13(0.01)$–$0.15(0.01)$ in 2008–2010; in the *U* band, the same value was observed in 2016–2020). In bands *V* and *B*, the same maximum values were recorded in Interval 1 and in 2016–2020 (0.06 and 0.08, respectively).

In the particular intervals of Interval 1, the gamma-ray and optical–UV behavior can be summarized as follows:

1. Interval 1a was characterized by the highest 0.3–300 GeV states and mean photon flux recorded during Interval 1, while the fractional variability amplitude was the same in all intervals within the error ranges (see Table 5 for the values of F_{max}, $\overline{F}$, and F_{var}). The source was detected securely within each 1 week bin and showed various moderate flaring behavior, with an elevated mean 0.3–300 GeV state of ~4.5 months duration (during 59,255–59,390). This subinterval was notable for the highest values of the quantities F_{max} and F_{var} in the $UVW1 - UVW2$ bands during Interval 1 (see Table 5). However, the source was not variable at the 3σ confidence level in the *V*–*B* bands (in contrast to the *U*-band emission), owing to the few number of the observations as well as to the higher measurement errors and a general trend of increasing variability strength toward the higher frequencies. In the UVOT bands, the source showed brightenings and subsequent declines by 10%–43%, mostly with no evident correlation with the XRT and LAT-band variabilities.
2. The aforementioned two detections below the 3σ significance from 1 week binned LAT data occurred in Interval 1b, when the source showed the highest X-ray states. This subinterval was also characterized by the lowest mean 0.3–300 GeV flux and weakest flaring activity throughout the here-presented period. In each UVOT band, the optical–UV flux showed a declining trend during MJD (595)70–90 when the source underwent a strong two-peak flare. Similarly, low optical–UV states were observed in MJD(596)30–60 along with the subsequent short-term X-ray flares (described in Section 3.1.1). However, the source was found in the flaring optical–UV states in the second half of this interval, similar to the XRT and MAXI-band observations.

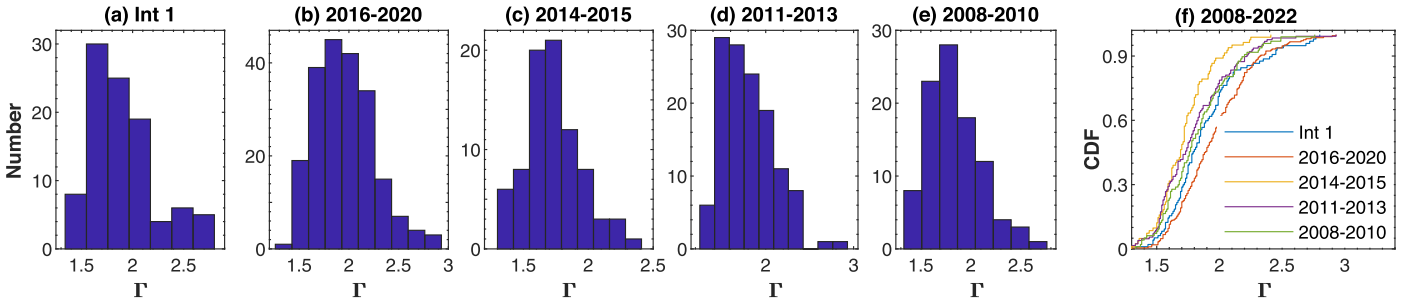

Figure 9. Same as Figure 6 for the LAT-band photon index.

3. While the source showed a long-term decline in the baseline X-ray flux level in Interval 1c, the 0.3–300 GeV brightness did not show a similar trend: the baseline γ-ray level was nearly constant, and only a moderate flare with $\sim$1.5 months duration occurred. On the other hand, this subinterval was notable for the highest mean optical–UV fluxes (except for the band V; see Table 5). However, the $F_{\rm var}$ values in bands $U-UVW2$ were the lowest in Interval 1. The source showed a variability by 10%–30% and, contrary to the X-ray energy range, no trend of a long-term brightness decline was observed.

The source rarely showed a significant LAT-band spectral curvature (detected with a significance of 2σ and higher): even in the case of the biweekly integration, only four spectra (8% of the 0.1–300 GeV spectra extracted from 2 week binned data) were curved with $b = 0.34(0.17)$–$0.57(0.18)$. The detection of significant curvature was even more rare among the spectra extracted with the 1 week integration (less than 3%). In the case of insignificant curvature, we refitted the spectra using a simple power law to obtain lower uncertainties for the photon index and flux. This model yielded a wide range of the 0.3–300 GeV photon index $\Delta\Gamma = 1.46 \pm 0.31$ and $\Gamma_{\rm min} = 1.34 \pm 0.13$ (see Figure 9(a) and Table 8). At least 59% of these spectra were hard with $\Gamma < 2.0$. On average, the spectra from Interval 1b were harder than those from Intervals 1b and 1c ($\overline{\Gamma} = 1.82$ (0.03) versus $\overline{\Gamma} = 1.92(0.03)$–$1.94(0.03)$).

4. Discussion

4.1. MWL Flux Variability and Physical Implications

4.1.1. Variability Character

The erratic long-term flares on timescales from several weeks to a few months are generally explained by the propagation and evolution of relativistic shocks, which start close to the central object and travel through the blazar jet (see, e.g., Kirk et al. 1998). However, such variability was superimposed on the longer-term enhancement in the baseline 0.3–10 keV flux level. Such a behavior was also reported for another nearby bright HBL source 1ES 1959+650 by Kapanadze et al. (2018) and explained by the possible enhanced matter collimation rate on yearly timescales. Note that the historical 0.3–10 keV light curve of Mrk 501 (see Figure 1(a)) shows long-term variations in the baseline X-ray level on timescales of a few years also during 2011–2015.

In order to check for possible quasiperiodic behavior in the flux variations in the period presented here, first, we constructed a Lomb–Scargle periodogram (LSP; Lomb 1976; Scargle 1982) from the most densely sampled data trains in the 0.3–10 keV, $UVW2-UVW1$, and 0.3–300 GeV bands. The LSP is an improved Fourier-based technique, which was developed for unevenly sampled time series g_n without interpolation for the data gaps (VanderPlas 2018). This technique can detect the most significant power spectral density (PSD) peak corresponding to the brightness periodicity, and estimate the detection significance by testing the false-alarm probability of the null hypothesis. For this purpose, we simulate light curves that match the PSD, the probability density function, sampling, and observational noise by using the recipe of Emmanoulopoulos et al. (2013).

An alternative check for the reliability of the detected LSP peak is a weighted wavelet Z-transform (WWZ; Foster 1996 and references therein). This technique is capable of detecting variability timescales from the unevenly sampled observations. However, the constructed LSP and WWZ plots (Figure 10) do not show any firm evidence of the (quasi)periodicity: there are low-power, permanent, nearly horizontal narrow strips in the WWZ plots, which are based on the XRT and LAT-band data trains (Figures 10(a)–(b)). However, the corresponding peaks are below the 2σ significance in the LSP plots and show a slow variation in the period. Such a situation is described in detail by O'Neil et al. (2022) and explained to be red noise. Note that this strip shifts gradually down to 70–90 days in Figures 10(c)–(d). An additional, similar case is presented in the latter figures: we observe the strips starting at $P \sim 200$ days MJD 59,250 and gradually shifting to $P \sim 230$ days at the end of the data trains. The significances of the corresponding LSP peaks are less than 2σ. According to O'Neil et al. (2022), only the peaks with a significance of 3σ and higher correspond to genuine periodicity. The same strips are not visible in the XRT and LAT-related plots.

As discussed in Section 3.1.1, the 0.3–10 keV light curve showed a variety of flare profiles, which represent the specific cases of particle acceleration and cooling. Namely, a (nearly) symmetric shape of the flare, with or without a long standing plateau, indicates that the observed variability was driven by the crossing timescale of the underlying disturbance (e.g., relativistic shock front; Roy et al. 2019). Consequently, the given flare is dominated by the time required for the radiation (or the "responsible" particles) to cross the emission region (Abdo et al. 2010), while the cooling timescale of radiating particles is of lower importance. Note that the symmetric flare profiles were detected only in Interval 1c. On the other hard, observation of symmetric flares is less expected: according to Nalewajko (2013), an overall asymmetric variability profile can be a superposition of different individual flares occurring in different emission regions that lie at different azimuthal angles in the jet cross section.

According to Roy et al. (2019), flares with a negative asymmetry may indicate a gradual acceleration of the particles, which radiate X-rays and/or are responsible for the IC

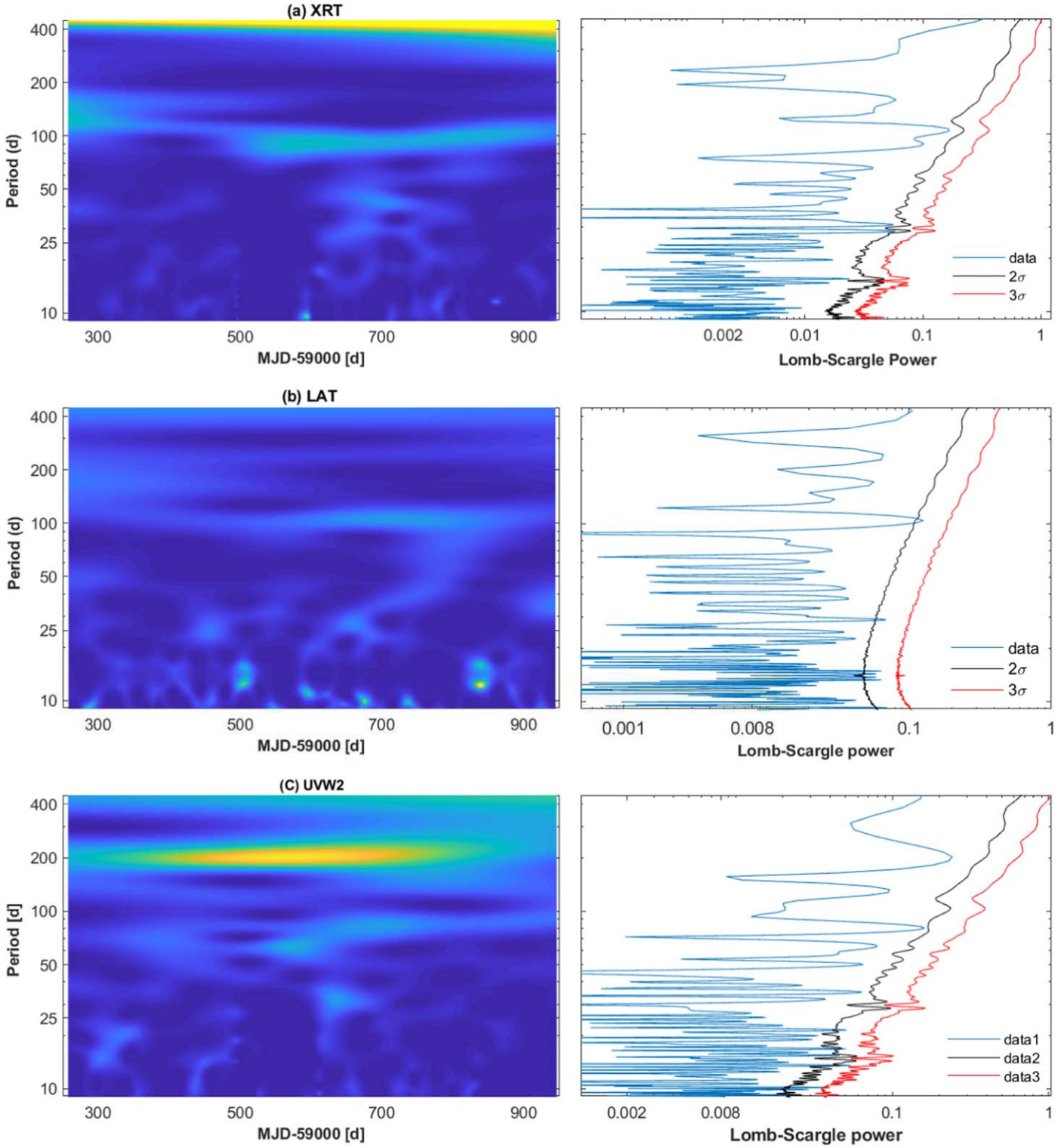

Figure 10. WWZ (left column) and LSP (right column) plots in different spectral bands: Panels (a) and (c) are based on the 1 day binned 0.3–10 keV and *UVW2* band light curves, respectively; panel (b) is based on 1 week binned 0.3–300 GeV flux values.

upscattering of low-energy photons to the MeV-to-GeV range. In that case, their cooling timescale can be shorter than the acceleration one. In X-rays, such instances were present only during the rising phase and maximum epoch of the long-term flare observed in 2021–2022. Note that this acceleration type is inherent to the stochastic, second-order Fermi mechanism operating in the jet region with a low magnetic field and high matter density (Virtanen & Vainio 2005). Consequently, the latter could hint at a higher importance of the stochastic particle acceleration in the particular time interval. However, the source showed the anticorrelation $b - E_{\rm p}$ only in interval 1c (which is one of the predictions of the efficient stochastic acceleration), while it was not detected at the 99% confidence in Interval 1a, which was the only subinterval showing such a flaring profile. Consequently, the observed longer-rising phase of the flares with a negative asymmetry could be due to the superposition of

two or more low-amplitude and short events, not individually detectable but producing an apparently prolonged rising phase of a single flare. Moreover, the absence of such flares in Interval 1c could be an artifact of observational sampling.

The time-dependent modeling of Saito et al. (2015), based on the BLAZAR code developed by Moderski et al. (2003), demonstrated that a nonuniformity of the Doppler factor across the jet (caused by the radial expansion of the relativistic flow) may lead to a significant symmetry distortion of the observed light curves and produce an asymmetric flare profile with substantially extended decay phase (i.e., showing a positive asymmetry). Consequently, the light curve corresponding to the flare decay phase is rather dependent on the gradient of the bulk Doppler factor across the emitting shells of the jet plasma: the emitting shells are considerably extended in the jet radial direction, so that the different parts of shells are observed at different viewing angles. Consequently, the emission produced within those parts characterized by the largest inclinations arrives to the observer with a significant time delay compared to the emission of the parts located at smaller viewing angles. In such a situation, the flare decline profile can be less impacted by the radiative cooling of the highest-energy particles. With the decreasing jet opening angle, however, the variance of the Doppler factor across the emitting shell becomes smaller and, consequently, the flare asymmetry decreases and is expected to become symmetric for the jet opening angle $\theta \lesssim 0.3$ deg and narrower. As discussed in Section 3.1.1, the source frequently showed 0.3–10 keV flares with a positive asymmetry in Intervals 1a–1b, and we may conclude that the situations with a considerable jet opening angle should be common for Mrk 501. In fact, Giroletti et al. (2008) estimated the intrinsic jet opening angle to be 10°–15°, which is considerably higher than the aforementioned limit. This result was obtained from the deep very long baseline interferometry observations at 1.4 GHz with the High Sensitivity Array in 2004 November, while no opening angle value was reported for the target by Pushkarev et al. (2017) from the Monitoring Of Jets in AGNs with VLBA Experiments (MOJAVE) program carried out at 15 GHZ during 1995–2015. Alternatively, flares with a positive asymmetry can be explained by a fast injection of accelerated particles and slower radiative cooling and/or escape from the energization region and, therefore, to be considered as a cooling-dominated variability (Abdo et al. 2010). However, the radiative lifetimes corresponding to the X-ray to MeV–GeV energy range are generally very short, and in the case that the emitting shells are not considerably extended in the jet radial direction during the particular flare, the observed flare profile with an apparent positive asymmetry can by produced by the superposition of two or more low-amplitude, shorter-term events occurring in the period of the long-term brightness decline.

The source also exhibited a two-peak flare profile several times in the both XRT and LAT-band light curves. According to the simulations of the time-dependent spectra and light curves in the framework of detailed internal-shock model (Böttcher & Dermer 2010), such a timing feature can be established by the propagation of forward and reverse shocks. The latter can be triggered by colliding "shells" of high-energy plasma, injected into the blazar jet with different speeds: a forward shock moving into the slower shell and a reverse one propagating in the faster shell.

4.1.2. Log-normality and MWL Correlations

We also performed a check for the log-normal flux variability, which can provide important information about the triggering unstable mechanism as follows (Rieger 2019): (i) influence of the accretion disk (AD) instabilities on the jet. Namely, independent density fluctuations in the AD, occurring on the local viscous timescales and characterized by a negligible damping, can propagate inward and couple together to produce a multiplicative behavior in the innermost disk part. This perturbation is efficiently transmitted to the jet (e.g., by means of the particle injection rate), if the timescales for particle acceleration and radiative losses within the jet are correspondingly small. Consequently, a log-normality can be feasible over different energy ranges and timescales; (ii) cascade-related emission processes (e.g., proton-induced synchrotron cascades). In that case, log-normal variability can be observed at optical-to-gamma-ray frequencies and over timescales depending on the energy range; (iii) log-normality can be associated with the acceleration process itself, e.g., with random fluctuations in the particle acceleration rate (Sinha et al. 2018). In such a situation, log-normality is expected to be energy-dependent, becoming weaker toward lower energies and disappearing at the energies $\gamma \rightarrow \gamma_0$, with γ_0 to be the injection Lorentz factor.

In order to detect a log-normality, we constructed histograms from all of the available flux values of Mrk 501 in those energy bands where a significant number of the data points were available, and the detection of this phenomenon would not be affected by a sparse sampling. Namely, Figures 11(A1)–(A5) present the distributions of the unabsorbed, daily binned 0.3–10 keV flux values in Interval 1 and in the parts of the period 2008–2020, fitted with the Gaussian and log-normal functions. The corresponding values of the reduced Chi-squared (presented Table 13 for each energy range in the different time intervals) indicate that the log-normal function fitted significantly better with the histogram in Interval 1 and a similar situation was also present in the intervals 2011–2013, 2014–2015, and 2016–2020, while the distribution was slightly closer to the Gaussian shape in 2008–2010 (possibly owing to the higher fraction of the X-ray emission related to the ultrarelativistic electron populations energized by the local, jet-inherent instabilities compared to other time intervals). Intervals 1a–1c also showed a log-normality. In Interval 1, the log-normality was also observed in the separate 0.3–2 and 2–10 keV bands: the corresponding variabilities showed a strong correlation with each other (see Figure 12(a) for the corresponding scatter plot; Table 10 for the value of the correlation coefficient and the corresponding p-chance). Strong $F_{0.3-2\,\mathrm{keV}} - F_{2-10\,\mathrm{keV}}$ correlations also occurred in different intervals of the period 2008–2020 (as found within our spectral analysis). This result indicates these emissions were produced by the same ultrarelativistic electron population via the synchrotron mechanism. Note that the correlation is weakened and even broken if there is a significant contribution of hard X-ray photons produced by IC upscatter of the local or external low-energy photons to the hard X-ray energies (which is not generally the case for HBL sources like Mrk 501.

The regularly sampled, weakly binned LAT observations yielded the distributions of the 0.3–300 GeV fluxes, which were modeled significantly better by the log-normal model in Interval 1 and in 2014–2020 (Figures 11(B1)–(B3)). However, the variability shown by the source in 2011–2013 was not well fitted with the log-normal and Gaussian models, and the latter

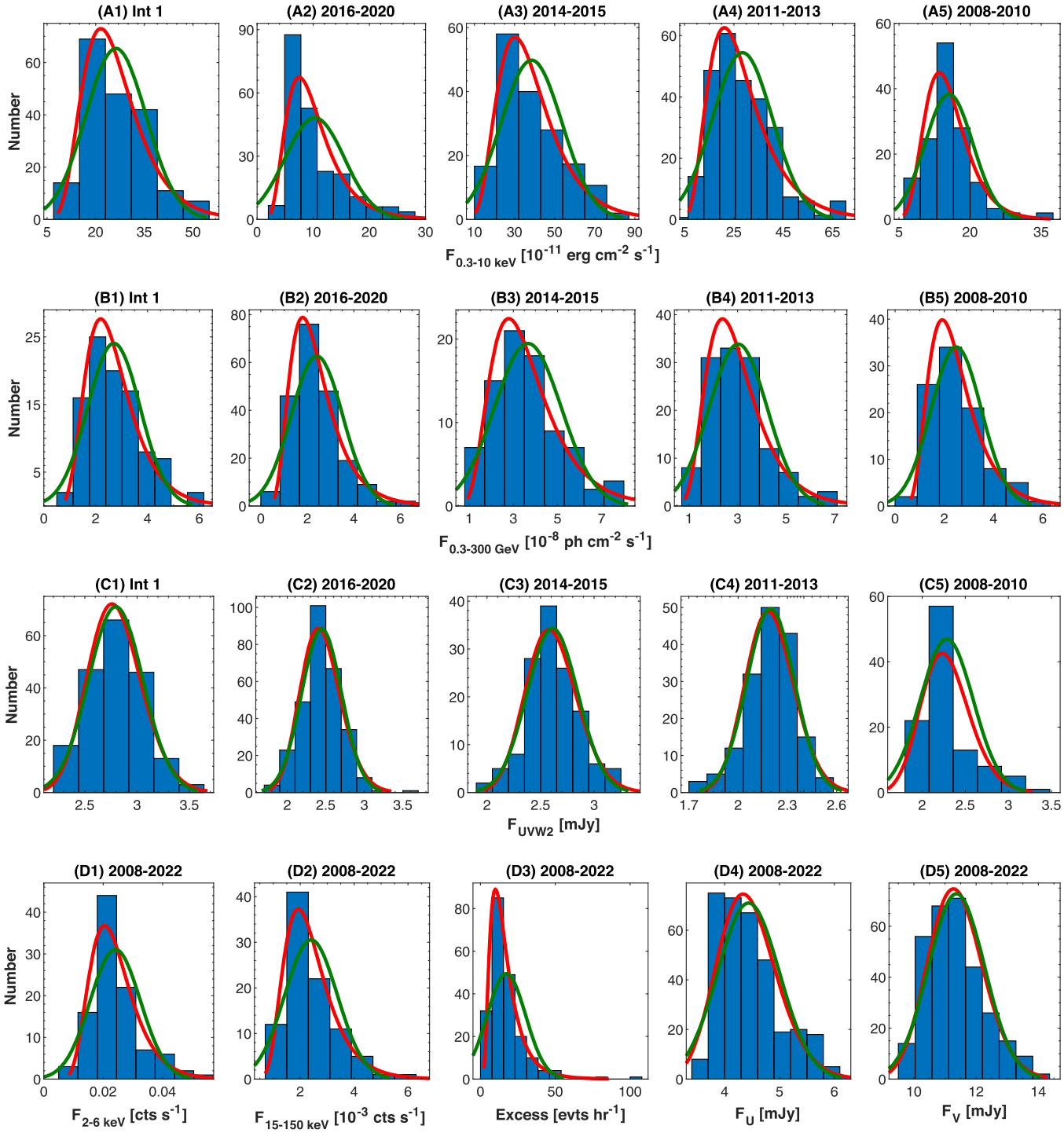

Figure 11. Distribution of the MWL flux values in different time intervals: 1 day binned unabsorbed XRT-band flux (A-panel); LAT-band fluxes with 1 week integration (B); 1 day binned *UVW2*-band flux (C); 1 week binned MAXI and BAT-band fluxes (panels (D1) and (D2), respectively); 1 day binned TeV-band excess rates (FACT observations; panel (D3)); 1 day binned fluxes in the UVOT bands *U* and *V* (panels (D4) and (D5), respectively). The red and green curves show the log-normal and Gaussian fits to the histograms, respectively.

model described the histogram from the interval 2008–2010 slightly better than the log-normal one (Figures 11(B1) and (B3), respectively; see Table 13 for the χ^2_r values for the log-normal and Gaussian fits to the histograms constructed for each time interval). This result could be related to the significant portion of those 0.3–300 GeV photons, which were produced by the external IC upscatter of the soft photons coming from other jet regions (Aharonian et al. 2009) by the ultrarelativistic electrons from the X-ray emission zone during the period 2008–2013.

As discussed in Section 3.3, the source did not show correlated variability in the 0.3–10 keV and 0.3–300 GeV energy ranges, neither in the entire Interval 1 nor in Intervals 1a–1c (as is also evident from the scatter plot presented in Figure 12(b)),[19] in spite of the log-normal flux distributions in both bands.

[19] Since no $F_{\rm XRT} - F_{\rm LAT}$ correlation was detected at the 99% confidence level, we have not included the corresponding correlation coefficient value in Table 10.

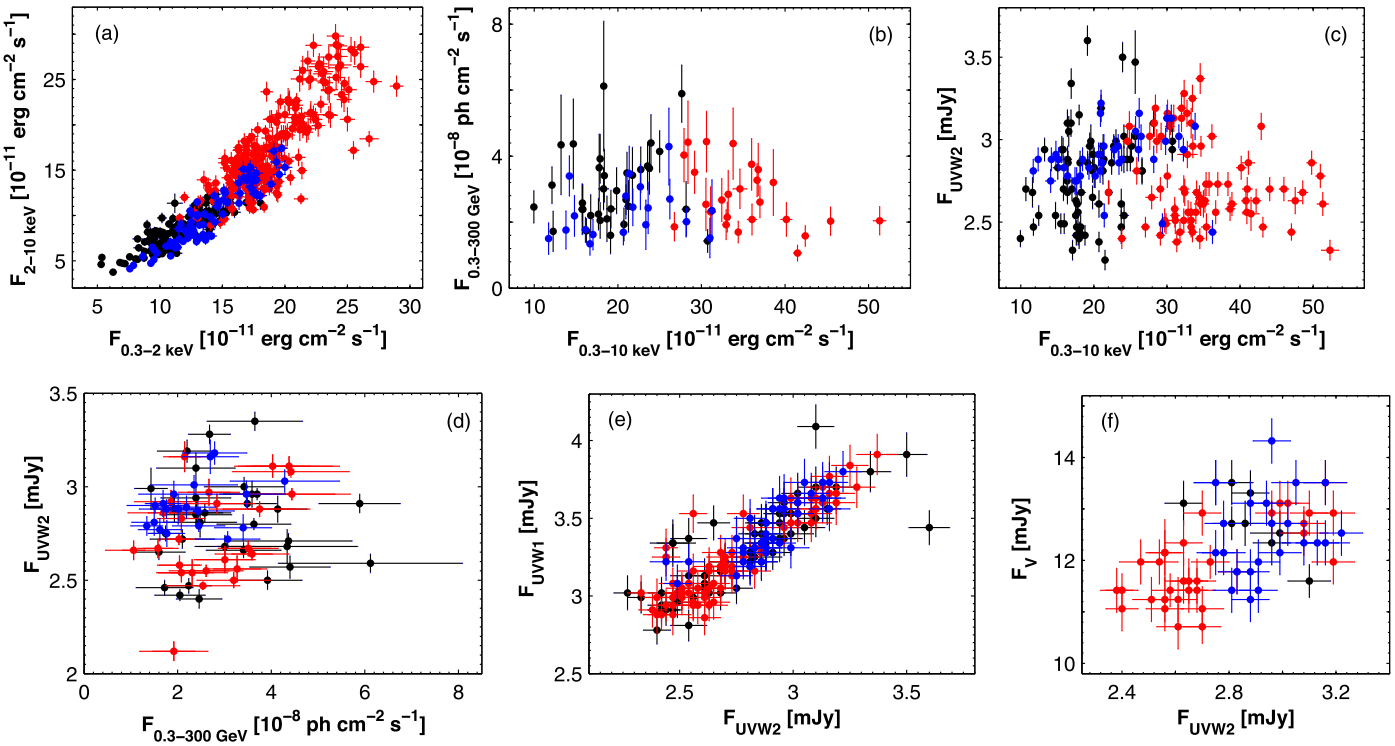

Figure 12. Correlation between the MWL fluxes. (a) Unabsorbed 0.3–2 keV and 2–10 keV fluxes; (b)–(c) 0.3–10 keV flux vs. the 0.3–300 GeV (1 week binned) and *UVW2* fluxes; (d)–(f) *UVW2* flux vs. the 0.3–300 GeV, *UVW1* and *V* fluxes. The black, red, and blue points correspond to the data from Intervals 1a, 1b and 1c, respectively.

Table 13
Goodness-of-fit for the Flux and Photon-index Distributions in Various Energy Bands

Energy Band (1)	χ^2_r/DOF (Gaussian) (2)	χ^2_r/DOF (log n) (3)
0.3–10 keV (Int 1)	2.50/6	1.20/6
0.3–10 keV (2016–2020)	1.87/10	1.18/10
0.3–10 keV (2014–2015)	2.32/7	1.10/7
0.3–10 keV (2011–2013)	1.53/10	0.95/10
0.3–10 keV (2008–2010)	1.15/8	0.88/8
0.3–3000 GeV (Int 1)	2.02/8	1.27/8
0.3–3000 GeV (2016–2020)	1.61/7/8	0.93/7
0.3–3000 GeV (2014–2015)	1.70/7	1.21/7
0.3–3000 GeV (2011–2013)	1.27/7	1.24/7
0.3–3000 GeV (2008–2010)	1.20/8	1.25/8
UVOT-*UVW2* (Int 1)	1.09/5	1.07/5
UVOT-*UVW2* (2016–2020)	1.03/9	1.01/9
UVOT-*UVW2* (2014–2015)	1.07/8	1.05/8
UVOT-*UVW2* (2011–2013)	1.24/7	1.22/7
UVOT-*UVW2* (2008–2010)	1.40/5	1.36/5
2–6 keV (2008–2022)	1.50/7	1.17/7
15–150 keV (2008–2022)	1.66/6	1.02/6
VHE-FACT (2008–2022)	2.51/13	1.19/13
UVOT-*U* (2008–2022)	2.44/9	2.13/9
UVOT-*V* (2008–2022)	1.41/8	1.36/8

Note. The distribution fits are performed by using the Gaussian and log-normal functions (Columns 2 and 3, respectively).

Presumably, the log-normality phenomenon was related to the different instability processes. For example, the source frequently showed hard HE γ-ray spectra (see Section 3.3), which are expected if there was a significant contribution of the γ-ray photons from the hadronic cascades to the 0.3–300 GeV energy range (Shukla et al. 2015). This mechanism also could yield a log-parabolic flux distribution (Rieger 2019), although this may break the correlation between the γ-ray and synchrotron (e.g., optical-to-X-ray) emissions expected in the framework of the one-zone SSC model (Böttcher & Dermer 2010). Note also that a significant X-ray and LAT-band correlation was found by Abe et al. (2023) for the entire period 2008–2020, while this correlation was absent in the separate interval 2017–2020. Similarly, the correlation $F_{\rm XRT} - F_{\rm LAT}$ was also absent during 2014 March–October (Paper I), and the data sets not belonging to these two intervals should be responsible for the positive correlation between these emissions in the entire period 2008–2020.

Although the *UVW2*-band fluxes showed a good fit with the log-parabolic function, the latter showed a nearly zero-skewness and was practically indistinguishable from the Gaussian fits with the same histograms (Figures 11(C1)–(C4) and Table 13). Finally, none of these models showed a good fit with the *UVW2*-band histogram corresponding to the interval 2008–2010 (Figure 11(C5)). Similar results were obtained for the variations shown by the source in other UV bands: they exhibited strong correlations with each other and with that recorded in the *UVW2*-band (see Table 10 and Figure 12(e)), indicating their origin in the same particle population and emission mechanism. The latter was significantly different from those responsible for the variability and emission generation in the XRT and LAT bands: the *UVW2*-band variability showed a positive correlation with the 0.3–10 keV one (although weakly) only in Interval 1a, while it was not present in Intervals 1b–1c and, eventually, the scatter plot $F_{0.3-10\,\rm keV}$–$F_{\rm UVW2}$ does not show any significant correlation for the entire Interval 1 (Figure 12(c)). The source showed

mostly uncorrelated variabilities also in different intervals of the period 2008–2020 (which we checked; see also Paper I). This result could be caused by significant contribution of the UV emission from other jet regions (see the discussion above). A similar complex relation was observed also between the UV and HE γ-ray variabilities: a statistically significant correlation was observed only in Interval 1b, contrary to other intervals that destroyed a correlation in the scatter plot $F_{0.3-300\,\mathrm{GeV}}$–$F_{\mathrm{UVW2}}$ constructed for the entire Interval 1 (see Figure 12(c) and Table 10). Note that the 0.3–300 GeV flux was weakly correlated with the those in the UVOT UV-bands, while correlated relatively strongly with the optical emission during 2014 March–October (Paper I).

A log-normality was also not present in the longer-wavelength UVOT bands *U*–*V*: neither this model nor the Gaussian one are well fitted with the corresponding histograms (Figures 11(D4)–(D4)). Since the observations were significantly fewer in these bands, we constructed the histograms by using the entire data sets from the entire period 2008–2022. This result could be related to the higher importance of the local, jet-related instabilities in the production of optical photons. For example, fluctuations in the electron escape rate can yield flux distributions that significantly differ from Gaussian and log-normal ones (Sinha et al. 2018). Moreover, a difference from the log-normal variability could be related to the "contamination" by photons coming from other jet regions. In turn, these photons could be undergoing an IC upscatter and contribute to the LAT-band emission, eventually breaking the correlation of the latter with those produced locally in the synchrotron bands. Moreover, the same process could bias the LAT-band variability from the log-normality, which was observed during 2008–2013. Note that the *B*- and *V*-band variabilities are not cross-correlated as strongly as those observed at the UV frequencies (see Figure 12(f)), or as in the case of some other bright HBLs, e.g., very strong F_{B}–F_{V} correlation with $\rho = 0.89 \pm 0.02$ in 1ES 1959+650 during the strong X-ray flaring activity during 2016 January–August (Kapanadze et al. 2018) against $\rho = 0.67 \pm 0.05$ in Mrk 501. The latter could be an artifact of the underestimation of the host contribution to the total optical emission of Mrk 501 by Nilsson et al. (2007), which, on turn, was adopted by us for calculating the fluxes in millijanskys provided in Table 3 and used in the cross-correlation study. In favor of this suggestion, we remark the following: in the case of each UVOT observation of Mrk 501, the optical fluxes in the νF_{ν} representation do not show an increase toward the direction of higher frequencies, as is generally the case for the HBL sources having the synchrotron SED peak position in the X-ray energy range (see below). Consequently, we could obtain weaker F_{B}–F_{V} correlation (similar to other optical cross-correlations) and larger bias from the log-normal flux distributions. Moderate optical-to-optical and optical-to-UV correlations were observed also during 2008–2020 (see also Paper I and Abe et al. 2023).

Similar to the optical bands, we used the entire data sets corresponding to the 5σ detections of Mrk 501 in the MAXI and BAT bands for the log-normality search. Figures 11(D1)–(D2) demonstrate a good fit of these data with the log-normal model. A similar result was obtained for the FACT-band variability during the entire period 2008–2022 (Figure 11(D3), constructed by using the daily binned excess rates corresponding to the detections with 3σ and higher).

On average, our study shows a trend of weaker log-normality toward longer wavelengths, which is one of the features of the log-normality contributed by random fluctuations in the particle acceleration rate (as stated by Sinha et al. 2018). However, these results could also be related to the increasing contribution of the emission from those electrons, which were energized by the local, purely jet-related unstable processes or to the photons coming from the different jet regions (as discussion above). Moreover, the intraday 0.3–10 keV variability clearly shows the impact of the local, jet-inherent instabilities (as revealed by by means of the 0.3–10 keV IDVs; see the corresponding discussion below). Finally, we cannot exclude the impact of the hadronic cascades and AD-related instabilities: long-term flares on timescales from several weeks to a few months can generally be explained by the propagation and evolution of relativistic shocks, which start close to the central object and travel through the blazar jet (see, e.g., Kirk et al. 1998). In its turn, a shock can be triggered by the instabilities occurring in the accretion disk, which may momentarily saturate the jet with extremely energetic plasma having significantly higher pressure than the steady jet plasma downstream (Sokolov et al. 2004 and references therein). Consequently, a log-normal MWL variability in the blazar jet can be naturally impacted by the instabilities in the inner AD area. Nevertheless, the long-term 0.3–10 keV outburst in Interval 1 could be linked to the enhanced matter collimation rate supported by some unstable mechanism operating in the accretion disk of Mrk 501 on yearly timescales (see Section 4.1.1). We conclude that the observed MWL variability was characterized by a complexity and could not be triggered by a single unstable mechanism.

4.1.3. Intraday Variability

In the period presented here, the duty cycle (DC, i.e., the fraction of total observation time during which the source displays a variability; see Romero et al. 1999 and references therein) of the 0.3–10 keV IDVs, detected for the target at the 99.9% confidence level was 34.8%, and this parameter rises to 45.1% when including those IDVs detected at the 99.5% confidence level. Note that these values are lower than the DC corresponding to the exceptionally strong flare in 2014 March–October (51.5% and 55.6%, respectively; see Paper I). Along with the higher flare strength (larger values of the parameters F_{max}, $\overline{F}$, and F_{var}, this result can be also related to the denser observational sampling: 101 XRT visits to the source with a net exposure of 112 ks (see Section 3.1.1 for the corresponding numbers in Interval 1). Nevertheless, we excluded several ObsIDs from our analysis owing to the bad quality or very short duration, as discussed above.

We also examined the occurrence of the 0.3–10 keV IDVs during the flares with various amplitudes and timescales, as well as in the time intervals between these events. Such a study may hint at the possible origin of these IDVs: those observed during the flaring epochs are in favor of the shock-in-jet scenario (interaction of a propagating shock front with the jet inhomogeneities; see Sokolov et al. 2004 and references therein). On the contrary, those events detected in the nonflaring segments of the long-term 0.3–10 keV light curve could be triggered by other kinds of the jet instabilities, which were not related to the propagation of relativistic shocks (e.g., Kelvin–Helmholz instability, magnetic reconnection, interaction between the standing shock, and relativistic jet flow; Marscher 2014) or by the unstable processes occurring near the

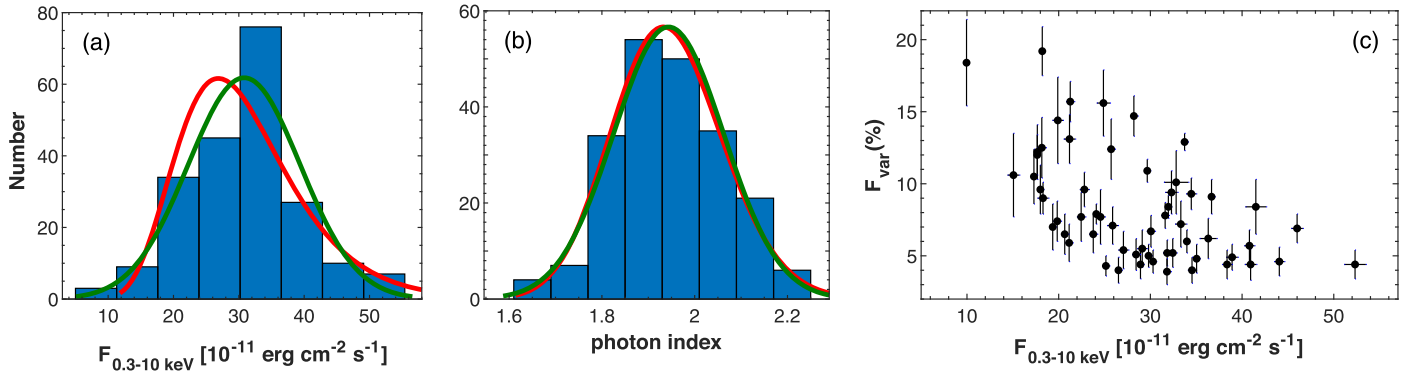

Figure 13. Statistical properties of the 0.3–10 keV IDVs: distribution of the related unabsorbed 0.3–10 keV fluxes (panel (a)) and photon indices (panel (b)); fractional variability amplitude plotted against the corresponding 0.3–10 keV flux (panel (c)). The red and green curves show the log-normal and Gaussian fits to the histograms, respectively.

event horizon of the central SMBH. In the latter case, the variable emission from the black hole vicinity will not be overwhelmed by the huge amount of X-ray flux produced at the shock front. Note that a vast majority of the 0.3–10 keV IDVs, which we reported in Section 3.1.2, were associated with the flaring states that are in favor of the shock-in-jet scenario: shock propagation can strongly amplify the turbulence in the shocked jet material (as discussed in Section 4.2.2). The most rapidly variable higher-energy emission (e.g., X-rays) is expected to be produced in the smallest jet areas, which contain the strongest magnetic field of the turbulent origin (see Mizuno et al. 2014).

It is also important to detect the flux-doubling/halving instances, since they allow us to constrain the upper limit to the variable emission zone as follows (Saito et al. 2013):

$$R_{\rm em} \leqslant \frac{c\tau_{\rm d}\Gamma_{\rm em}}{1+z}, \tag{4}$$

where $R_{\rm em}$ and $\Gamma_{\rm em}$ are the size and Lorentz factor of the emission zone, respectively. Here, the flux-doubling/halving timescale is calculated as $\tau_{\rm d,h} = \Delta t \times \ln(2)/\ln(F_2/F_1)$, where F_1 and F_2 are the initial and final flux values, respectively, and Δt is the corresponding time interval. However, the source did not show such instances on intraday timescales, in contrast to other bright HBLs (Mrk 421, 1ES 1959+650, and 1ES 0033 +595; see, e.g., Kapanadze et al. 2016, 2018; Kapanadze & Gurchumelia 2022). In the case of the 120 s binned count rates, the fastest observed flux-doubling instance occurred within 3.97 days (MJD 59,257.53–59,261.50), which corresponds to $\tau_{\rm d} = 1.28$ days. Using the typical value of the bulk Lorentz factor $\Gamma_{\rm em} = 10$ (see, e.g., Kapanadze & Gurchumelia 2022), we obtain an upper limit of 8.56×10^{16} cm for the emission zone responsible for that extreme variability.

In Figure 13(a), we constructed a histogram from the unabsorbed 0.3–10 keV fluxes corresponding to those XRT observations of Mrk 501 showing an IDV in Interval 1. While the entire data set of the XRT-band fluxes is well fitted with the log-normal model, this sample rather shows a Gaussian distribution than a log-normal one ($\chi^2_{\rm r}/{\rm DOF} = 1.22/7$ compared to 1.50/7 in the latter case). The distribution of the corresponding photon index is not significantly different from the Gaussian model (Figure 13(b)), which is expected in the case of random fluctuations in the particle acceleration rate (as suggested by Sinha et al. 2018). However, a log-normal flux distribution is also anticipated in that case. Hence, we conclude that the origin of the 0.3–10 keV IDVs is rather more complex than that caused by a single unstable mechanism (e.g., interaction between the relativistic shock front and the local, small-scale jet inhomogeneities with turbulent magnetic fields). Note that Figure 13(c) shows an anticorrelation between the fractional amplitude and the mean 0.3–10 keV flux for the 0.3–10 keV IDVs detected at the 99.97% confidence level. According to Zhang et al. (2005), this result indicates a strong nonstationary origin of the X-ray variability (as the random fluctuations in variance should not produce such a correlation) and fast variable physical conditions in the emission zone. Note that such properties are more inherent to relativistic shocks and turbulent magnetic fields.

4.2. Spectral Properties, Particle Acceleration, and Emission Processes

4.2.1. Photon Index and Relativistic Magnetic Reconnection

Our X-ray spectral analysis of the intense XRT observations of Mrk 501 in the period 2021 February–2022 December demonstrates an extreme spectral behavior compared to some previous time intervals. Namely, at least 9.3% of the log-parabolic spectra were very hard with $a < 1.80$, while the source did not show such spectra in 2008–2010 and 2016–2020, with significantly higher mean values ($\overline{a}$ = 2.02–2.15 versus $\overline{a} = 1.92$ in Interval 1; see Table 8). While only 20% of the photon indices were higher than $a > 2.0$ (taking into account the associated errors), at least 43.9% and 70.3% of the spectra were soft in the intervals 2008–2010 and 2016–2020, respectively.

On the other hand, the source exhibited even more extreme spectral properties in other time intervals: only one (out of the total 182) and three (out of 194) spectra with $a > 2$ were detected in 2014–2015 and 2011–2013, respectively, with the mean values $\overline{a} = 1.72$–1.76. In the case of the harder spectra, the largest difference with respect to the a-distribution of Interval 1 is shown by that from the interval 2011–2013 (see Figure 6(B5) and Table 9). Note also that at least 65% of the curved spectra were very hard with $a < 1.80$ in 2014–2015 (versus 9.3% in Interval 1), primarily owing to the exceptionally strong X-ray flaring activity of Mrk 501 during 2014 March–October. A similar situation was observed also in 2011–2013 (at least 57.7% of the curved spectra harder than $a = 1.80$). These periods also were notable by the extremely hard spectra with $a \sim 1.50$ or lower down to $a = 1.39 \pm 0.06$ (9

and 19 instances in the intervals 2011–2013 and 2014–2015, respectively), which were not present in Interval 1.

However, the distributions of the photon index in these periods were significantly softer than that shown by 1ES 0033 +595 during the XRT observations performed in 2005–2022: it was the hardest source among HBLs with more than half of the curved spectra showing very hard and extremely hard values (Kapanadze & Gurchumelia 2022). Nevertheless, this source showed $\alpha \sim 1$ for 13 spectra, which has not been reported for any other HBL to date.

Among the power-law spectra, only one spectrum showed the photon index less than $\Gamma = 1.80$, while such instances were significantly more numerous in 2014–2015 (24 instances, 36.4% of all power-law spectra) and in 2011–2013 (82, 39.6%) with the most extreme spectrum described by $\Gamma = 1.42 \pm 0.03$ in the latter case. A good fit of most of these spectra with the power-law model cannot simply be related to the possible case when the synchrotron SED peak position is far beyond the XRT instrumental range. This can make it difficult to evaluate the spectral curvature, which could be the case for very hard and extremely hard power-law spectra with the possible presence of the synchrotron SED peak far beyond 10 keV. However, such spectra amounted to more than one-third of all power-law spectra in 2014–2015, which was notable by the lowest portion of these spectra among all time intervals (25.5%; see Column 5 in Table 1). Note also that this percentage was the highest in Interval 1a (58.1% of all spectra) when no very hard power-law spectra were observed.

The detection of the spectral curvature could also be prevented in the case of very soft spectra ($\Gamma > 2.2$) with the possible location of the synchrotron SED peak at the UV frequencies. However, only one spectrum was detected securely in this range in Interval 1a, notable for the highest portion of the power-law spectra. Therefore, more frequent observation of power-law spectra in Mrk 501 (compared to other bright HBLs) could be related to the higher importance of those acceleration processes, which yield the establishment of a power-law electron energy distribution (EED).

According to the relativistic magnetohydrodynamic (MHD) simulations of Bodo et al. (2021), a nonlinear kink instability can generate current sheets, where particles can be efficiently accelerated via the magnetic reconnection. Frequently, such an instability first generates large-scale current sheets, which then break up into small-scale turbulence and a fast magnetic reconnection can be also triggered by turbulence in the small-scale, highly magnetized jet area (Lazarian et al. 2014). The particle-in-cell (PIC) simulations (see, e.g., Sironi & Spitkovsky 2014; Werner & Uzdensky 2017) showed that the magnetic reconnection can be relativistic in such a situation: the energy density of the reconnecting magnetic field B_0 exceeds that of the ambient plasma (including the rest-mass energy), heating plasma to relativistic temperatures, driving relativistic flows and accelerating particles to ultrarelativistic energies. In that case, a hard power-law particle energy distribution $N(\gamma) \propto \gamma^{-p}$ can be established with $p \rightarrow 1$, which can result in the hard power-law X-ray spectra.

As noted in Section 3.2, the source showed fast log-parabolic-to-power-law EED transitions and vice versa for the spectra extracted from 150–600 s segments of the observation performed during a single Swift orbit. Namely, we presented an extreme example of the fast log-parabolic-to-power-law EED transitions and vice versa for the spectra extracted from the different segments of a single XRT observation ObsID 11184188: three spectra out of five 195 s segments showed a curvature with $b \sim 0.3$ or lower, which is anticipated in the case of the efficient stochastic acceleration of electrons in the highly turbulent jet medium (see below). Two other segments of the same observation showed hard power-law spectra with a transition "chain" log-parabola → power law → log-parabola → power law. This finding may have an important physical implication: we suggest that there were two turbulence-driven reconnection instances in the relativistically magnetized jet area with small spatial extent during that XRT observation of Mrk 501. Namely, if we adopt a typical value of the bulk Lorentz factor for the emission zone $\Gamma_{\rm em} = 10$ (Falomo et al. 2014), then the relativistic reconnection occurred on the spatial scale of $\sim 10^{-12}$ cm during that observation.

The same or similar transition "chains" (with two to four transitions) between the hard power-law and curved spectra with $b \sim 0.2$–0.3 within the comparable spatial scales were observed during other 28 single-orbit XRT observations of Mrk 501 (ObsIDs 11184183, 11184189, etc.; mostly in Interval 1b). Moreover, transition "chains" with two to three interchanges between the soft power-law spectra and low-curvature ones were the case for an additional 43 XRT observations, which could be caused by nonrelativistic magnetic reconnection in the small-scale jet environment. In several cases, the power law to log-parabolic transitions occurred on timescales from a few hours to up to 1 day, generally, during the 0.3–10 keV IDVs presented in Table 6. In those cases, the transitions occurred on spatial scales of $\sim 10^{13-14}$ cm, with participation of the both hard and soft power-law spectra.

4.2.2. Spectral Curvature, Relativistic Shocks, and Turbulence

Similar to other bright HBLs, Mrk 501 generally demonstrated a harder-when-brighter spectral behavior during the X-ray flares presented in Section 3.1. The observed hardening of the spectrum with increasing flux can be reproduced by a shock-in-jet model with escape and synchrotron losses (see Kirk et al. 1998 and references therein). In this model, the spectral slopes of accelerated particles are controlled by synchrotron cooling, and thus naturally represent the temporal behavior of the spectral index as observed in the 0.3–10 keV energy range. In the framework of the shock-in-jet scenario, a flaring behavior is explained by the shock front propagating through plasma whose density is locally enhanced (see, e.g., Sokolov et al. 2004 and references therein). Consequently, this enhancement increases the number of particles injected into the acceleration process. On the other hand, the increase in the plasma density is accompanied by an increase in the magnetic field strength, leading to a higher acceleration rate and a shift of the maximum particle energies to higher energies. In such a situation, a harder-when-brighter spectral evolution (exhibited by Mrk 501 in Interval 1, as well as in the different pars of the period 2008–2020; see Table 10 for the anticorrelations $a - F_{0.3-10\,\rm keV}$ and $\Gamma - F_{0.3-10\,\rm keV}$) indicates a general stronger and faster variability in the number of the electrons producing X-ray photons by the synchrotron mechanism.

Note also that the source showed a bluer-when-brighter chromatism, i.e., variable optical and optical-UV color-indices (see Figure 14 and Table 14 for the corresponding correlation coefficients), which represents a lower-frequency extension of the harder-when-brighter spectral evolution and exhibits an increasing variability strength with frequency. While this trend was weakly expressed between the adjacent bands, it becomes

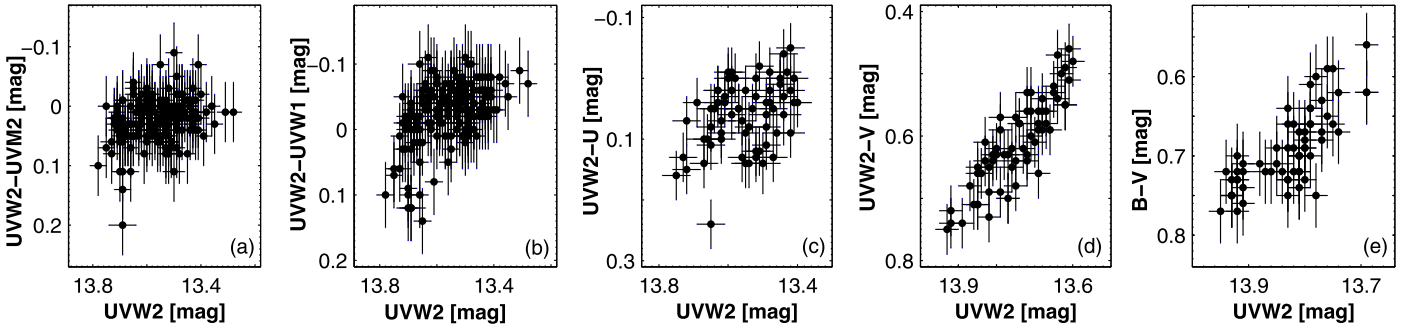

Figure 14. Magnitude–color diagrams for the observations performed with UVOT.

Table 14
Correlations between MWL Fluxes in Interval 1 and Its Three Parts

Quantities	ρ	p
	Int 1	
$F_{0.3-2\ \mathrm{keV}}$ and $F_{2-10\ \mathrm{keV}}$	0.90(0.03)	1.1×10^{-17}
F_{UVW2} and F_{UVM2}	0.88(0.03)	8.3×10^{-17}
F_{UVW2} and F_{UVW1}	0.86(0.03)	4.0×10^{-16}
F_{UVW2} and F_{U}	0.79(0.04)	9.3×10^{-15}
F_{UVW2} and F_{B}	0.64(0.05)	4.8×10^{-9}
F_{UVW2} and F_{V}	0.54(0.06)	5.2×10^{-6}
F_{B} and F_{V}	0.67(0.05)	1.1×10^{-9}
m_{UVW2} and $m_{\mathrm{UVW2}} - m_{\mathrm{UVM2}}$	0.28(0.11)	2.1×10^{-4}
m_{UVW2} and $m_{\mathrm{UVW2}} - m_{\mathrm{UW1}}$	0.47(0.08)	5.2×10^{-10}
m_{UVW2} and $m_{\mathrm{UVW2}} - m_{\mathrm{U}}$	0.47(0.08)	5.2×10^{-10}
m_{UVW2} and $m_{\mathrm{UVW2}} - m_{\mathrm{V}}$	0.85(0.03)	3.8×10^{-15}
m_{U} and $m_{\mathrm{V}} - m_{\mathrm{V}}$	0.83(0.04)	9.1×10^{-15}
m_{B} and $m_{\mathrm{V}} - m_{\mathrm{V}}$	0.68(0.05)	9.1×10^{-15}
F_{var} and $F_{0.3-10\ \mathrm{keV}}$	−0.53(0.10)	2.0×10^{-6}
	Int 1a	
$F_{0.3-2\ \mathrm{keV}}$ and $F_{2-10\ \mathrm{keV}}$	0.83(0.03)	8.0×10^{-16}
F_{UVW2} and $F_{0.3-10\ \mathrm{keV}}$	0.33(0.11)	5.9×10^{-3}
F_{UVW2} and F_{UVM2}	0.84(0.02)	8.3×10^{-17}
F_{UVW2} and F_{UVW1}	0.81(0.03)	2.2×10^{-15}
	Int 1b	
$F_{0.3-2\ \mathrm{keV}}$ and $F_{2-10\ \mathrm{keV}}$	0.77(0.04)	1.6×10^{-15}
F_{UVW2} and F_{UVM2}	0.88(0.03)	8.3×10^{-17}
F_{UVW2} and F_{UVW1}	0.89(0.03)	6.7×10^{-17}
F_{UVW2} and $F_{0.3-300\ \mathrm{GeV}}$	0.40(0.12)	3.7×10^{-3}
F_{UVM2} and $F_{0.3-300\ \mathrm{GeV}}$	0.36(0.12)	8.5×10^{-3}
F_{UVM2} and $F_{0.3-300\ \mathrm{GeV}}$	0.34(0.12)	9.8×10^{-3}
	Int 1c	
$F_{0.3-2\ \mathrm{keV}}$ and $F_{2-10\ \mathrm{keV}}$	0.91(0.02)	5.5×10^{-18}
F_{UVW2} and F_{UVM2}	0.84(0.03)	7.7×10^{-16}
F_{UVW2} and F_{UVW1}	0.81(0.04)	1.3×10^{-15}

gradually stronger with the separation of the particular bands and, eventually, Figure 14(d) shows a strong anticorrelation between the *UVW2*-band magnitude and color-index $UVW2 - V$.

However, the source showed a deflection and even a softer-when-brighter evolution during some short time intervals of various durations (a few hours to weeks).[20] This behavior was possibly related to the addition of a new, soft flaring component in the emission zone to the existing hard one. Eventually, the total 0.3–10 keV flux increased significantly, and stronger X-ray flares were recorded, while destroying the ongoing harder-when-brighter spectral evolution. Since such a situation was the most frequent in Interval 1a (reflected in the weak a–$F_{0.3-10\ \mathrm{keV}}$ and Γ–$F_{0.3-10\ \mathrm{keV}}$ anticorrelations), a gradual increase in the baseline 0.3–10 keV level (observed in this interval) could be caused by frequent addition of soft X-ray emitting electron populations to the existing one. Along with the weakest photon index–flux correlation in Interval 1a, these new soft components yielded the elevated F_{var} value in this band, which was comparable to that in the hard 2–10 keV band. On the contrary, the hard-band F_{var} value was significantly higher than the softer-band "counterpart" in Intervals 1b–1c when the photon index–flux anticorrelations were also considerably stronger.

Moreover, the source exhibited a general shift of the synchrotron SED peak toward higher energies in Interval 1 (as discussed in Section 3.2), and a similar behavior was also recorded in different intervals of the period 2008–2020 (see Table 10 for the positive correlation $E_{\mathrm{p}} - F_{0.3-10\ \mathrm{keV}}$ in each time interval). Such a trend can be explained by the injection of high-energy particles in the shock acceleration process, which dominate in the observed brightness variations over a large range of activity (Acciari et al. 2021). Furthermore, the presence of the correlation E_{p}–$F_{0.3-10\ \mathrm{keV}}$ demonstrates a general dominance of synchrotron cooling of the highest-energy electrons over the IC cooling (see, e.g., Zhang 2010). The simulations of Tramacere et al. (2009) demonstrated that when E_{p} increases, the mean cooling timescale of the X-ray-emitting electron population shortens and can compete with the acceleration timescales. In such a situation, a weakening of the E_{p}–b anticorrelation is expected, since the cooling timescale is shorter than those of the first-order Fermi process and stochastic acceleration. This supposition is in accordance with our spectral study of Mrk 501: the source exhibited a very weak anticorrelation between the parameters E_{p} and b in Interval 1 against the strong E_{p}–$F_{0.3-10\ \mathrm{keV}}$ correlation. However, the latter trend was generally not observed in those time intervals, when the source showed a deflection from the harder-when-brighter spectral evolution, which are explained to stem from the addition of a new, soft flaring component in the emission zone. As noted above, the deflections from the harder-when-brighter trend were the most frequent in Interval 1a, and, correspondingly, no statistically significant E_{p}–$F_{0.3-10\ \mathrm{keV}}$ correlation was observed (see Table 10 and Figure 8(f)). Consequently, the observed X-ray variability of Mrk 501 frequently required a rather more complex emission scenario

[20] The weekly time intervals could be affected by relatively sparse observational sampling, and therefore, we cannot draw a firm conclusion as to whether the source was following a softer-when-brighter or unclear trend during the entire time interval.

than the one-zone SSC model. Moreover, the correlation $E_{\rm p}$–$F_{0.3-10\,{\rm keV}}$ was weak in 2016–2020, while the anticorrelation $E_{\rm p}$–b was not stronger than those observed in other time intervals. This result indicates a higher importance of the IC cooling in 2016–2020 and could be related to the weaker magnetic field and turbulence (see the additional discussion below) in the jet of Mrk 501 during that time interval that, in turn, yielded a general low level of synchrotron emission. Consequently, the source showed the lowest 0.3–10 keV states throughout the period 2008–2022.

Our spectral study also revealed an anticorrelation between the spectral curvature and 0.3–10 keV flux, which implies that the source, on average, showed smaller curvatures during X-ray flares than it otherwise would. Consequently, the stochastic acceleration was more efficient during the 0.3–10 keV flares: a low curvature is related to wider synchrotron SED, and the latter is expected within the efficient second-order Fermi process (see, e.g., Massaro et al. 2011). Namely, there is an inverse proportionality between the EED curvature r and the diffusion coefficient D in the Fokker–Planck kinetic equation: $r \propto D^{-1}$. On the other hand, $r \propto \varepsilon/(n_{\rm s}\sigma_{\varepsilon}^2)$ (Massaro et al. 2004), where $n_{\rm s}$ is the number of the acceleration steps, and σ_{ε}^2 is the variance of the energy gain ε. Consequently, the detection of low spectral curvatures implies higher values of $n_{\rm s}$ and diffusion coefficient, which requires a stronger turbulence, i.e., our spectral result indicates an increase in the turbulence strength within X-ray flares compared to the lower brightness states. As noted in Section 4.1, a strong X-ray variability of HBLs is most commonly explained in the framework of the shock-in-jet scenario. On the other hand, the relativistic MHD simulations of Mizuno et al. (2014) demonstrated that shock propagation through an inhomogeneous medium can yield an amplification of the turbulent magnetic field, owing to the shock interaction with higher-density inhomogeneities existing in the pre-shock medium. Eventually, the amplification of the jet turbulence can make the second-order Fermi mechanism more efficient when the curvatures with $b \sim 0.3$ are predicted (versus $b \sim 0.7$ in the case of inefficient stochastic acceleration; see Massaro et al. 2011).

However, the weakness of the anticorrelation $E_{\rm p}$–b and large percentage of the spectra with $b \sim 0.2$ and even lower indicate a high "contamination" of the stochastic acceleration process by other particle energization processes. The latter could be the first-order Fermi process operating at the relativistic shock front: when particles are confined by a magnetic field at the shock front, whose confinement efficiency is declining with increasing electron gyration radius (i.e., electron's energy), the probability p_i that a particle undergoes an acceleration step i is given by $p_i = g/\gamma_i^q$, where g and q are positive constants; γ_i^q is the particle's energy and energy gain at the ith step. When the magnetic field is characterized by the aforementioned property, then $q > 0$, and the probability for a particle to be accelerated is lower when its energy increases (so-called energy-dependent acceleration probability process, EDAP; Massaro et al. 2004). Consequently, a log-parabolic EED can also be established in this case, producing a curved photon spectrum. Tramacere et al. (2009) showed that the EDAP process also can yield an anticorrelation between the curvature parameter and the synchrotron SED peak position (as within the stochastic acceleration), although $E_{\rm p}$–b scatter plot may have a different slope than in the case of the second-order Fermi acceleration. Consequently, a joint operation of these two mechanism in the particle acceleration zone can produce a large scatter of the data points in the plane $E_{\rm p}$ versus b and, eventually, we may observe a (very) weak anticorrelation between these spectral parameters (as observed In Interval 1 and during each part of the period 2008–2020).

Such a complex acceleration scenario was presented by Katarzynski et al. (2006): initially, the particle can be efficiently accelerated at the shock front. After escaping into the shock downstream region, the particle can be further accelerated by the stochastic mechanism. As a result, the particle energy may increase enough to let the particle reenter the shock acceleration region and repeat an acceleration cycle by the first- and second-order Fermi mechanisms. Consequently, the spectral curvature $b \sim 0.3$ (expected from the stochastic mechanism) can be decreased in combination with the non-EDAP first-order Fermi process (yielding a power-law photon distribution) and obtain a weaker anticorrelation $E_{\rm p}$–b (as observed in each time interval). Note that the source showed the EDAP signatures in the period presented here, e.g., relatively large curvatures with $b > 0.4$ that are not expected in the case of the efficient stochastic acceleration. Moreover, the source showed a positive $a - b$ correlation in Interval 1b, which can be observed within the EDAP-acceleration of the electron population with very low initial energy γ_0 (Kapanadze et al. 2020).

This complex acceleration scenario is supported by the 2–8 keV observations of Mrk 501 with Imaging X-ray Polarimetry Explorer (IXPE) carried out in 2022 March 8–10 and 26–28 (Liodakis et al. 2022): the X-ray polarization degree was more than a factor of 2 higher than the optical one in both cases. The authors presented the possible explanations as follows: (1) higher-energy, hard X-ray emitting particles populate a magnetically more ordered region closer to the acceleration site, e.g., shock front, and then diffuse away to the area with a less-ordered magnetic field, producing optical emission with lower polarization; (2) in the plasma crossing a shock front and having a turbulent field, particle acceleration would be most efficient in those cells whose magnetic field is nearly parallel to the shock normal, leading to a higher value of the polarization degree and more pronounced variability at higher frequencies; (3) turbulence-induced reconnection in the jet flow impacted by transverse velocity gradients and yielding higher-ordered fields in the jet transverse direction. In the both time intervals of the IXPE observations, there were the densely sampled XRT campaigns for Mrk 501, which show a dominance of the curved spectra with a range of the curvature parameter values: (i) $b \sim 0.3$, hinting at the efficient stochastic acceleration of particles by turbulent magnetic fields; (ii) $b \sim 0.5$, the EDAP accelerating particles at the shock front; (iii) $b \sim 0.2$, joint operation of stochastic acceleration and non-EDAP first-order Fermi mechanism; and (iv) very fast log-parabolic-to-power-law EED transitions and vice versa, characterized to the turbulence-driven, relativistic magnetic reconnection (see Section 4.2.1). In contrast to IXPE, the XRT observations also include the soft 0.3–2 keV band, and the corresponding emission could be produced in those jet areas, which were relatively distant from the shock front and characterized by higher turbulence (i.e., less-ordered magnetic field).

When the magnetic field is not characterized by declining confinement efficiency with rising electron energy, the first-order Fermi mechanism can yield a power-law EED and the

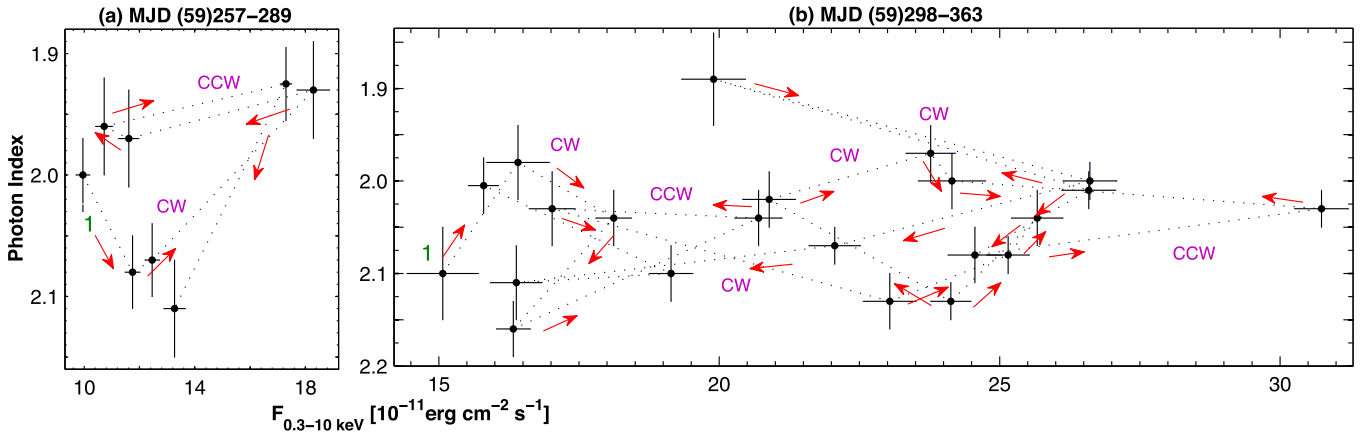

Figure 15. Spectral hysteresis patterns. In each plot, the start point is denoted by "1," and the subsequent looping behavior can be traced by means of the red arrows. (The complete figure set (6 images) is available.)

photon spectrum is well fitted with a simple power-law model. High importance of the non-EDAP first-order Fermi acceleration in the jet of Mrk 501 is imprinted on a larger portion of the power-law spectra in Interval 1 than that shown by other bright HBLs (45% versus 9.6%–27.5% for Mrk 421 in different periods; see Kapanadze et al. 2020). Therefore, we conclude that the properties of the magnetic field in the jet of Mrk 501, on average, differed from those of other HBLs (at least, in point of the confinement efficiency) in the period presented here. Note that the intervals Ia and Ic were particularly notable for this property (50%–58% versus 36% in Interval 1b; see Table 1). A similar situation also occurred during 2011–2013 and 2016–2020 (53%), in contrast to the interval 2014–2015, which was characterized by more than a twice-as-low portion of the power-law spectra and highest historical 0.3–10 keV states.

4.2.3. Spectral Loops

We can draw further conclusions about the particle acceleration mechanisms when investigating the spectral evolution of X-ray flares in the photon index–flux plane (so-called spectral hysteresis). The corresponding results are presented in Figure 15 and Table 15, which show that the source frequently followed a clockwise (CW) spectral loop. The latter can be observed if the spectral evolution is due to the flaring component starting in the hard X-ray band, making the spectrum progressively harder in the brightening phase of the source (Tramacere et al. 2009). Note that such a spectral evolution has an important physical implication: the timescales of X-ray flux variability, acceleration, and synchrotron cooling of the X-ray emitting particles (denoted as τ_{var}, τ_{acc}, and τ_{syn}, respectively) can be related $\tau_{syn} \gg \tau_{var} \gg \tau_{acc}$ (Kirk et al. 1998). Such a spectral component is triggered by a rapid injection of very energetic particles rather than by a gradual acceleration, and this scenario could be compatible with the first-order Fermi mechanism within the Bohm's limit of particle diffusion: in the case of a 1 G magnetic field and relativistic shock, this mechanism is capable of accelerating electrons to the typical energies required to produce X-ray photons on timescales of seconds (see Tammy & Duffy 2009). As listed in Table 15, the CW loops were observed in all parts of Interval 1, for the 0.3–10 keV flares with various profiles including that with a negative asymmetry, i.e., slow brightening and faster decline (see Figures 3(B1) and (B2)). This result cannot be explained by the gradual particle acceleration process. However, the observed longer-rising phase of the given flare could be the superposition of two or more low-amplitude and short events (as discussed in Section 4.1.1). Sometimes, two different, subsequent CW loops were observed during a single X-ray flare, or there was transition from a CW loop into the opposite, counterclockwise (CCW) behavior. Consequently, we may conclude the existence of two or more coeval short-term flares (characterized by similar or different particle acceleration processes, e.g., driven by the first- and second-order Fermi processes), which were not resolvable individually, and jointly produce an apparent longer-term brightness increase or decline phases.

In the case that magnetic field is significantly weaker than 1 G in the jet emission zone, the first-order Fermi process cannot be instantaneous, and a gradual acceleration of electrons is expected (Tammy & Duffy 2009). Consequently, an X-ray flare will propagate from low to high energies, and a CCW-type spectral evolution should be observed (Tramacere et al. 2009). The PIC simulations showed that a slow, gradual acceleration and CCW loops are also expected by stochastic acceleration of electrons in the jet region with low magnetic field and high matter density (Virtanen & Vainio 2005). Mrk 501 also frequently showed the CCW-type loops in Interval 1 (Table 15 and Figure 15). Several times, two different, subsequent CCW loops were observed, or the source showed a CCW → CW transition (or conversely) during the single X-ray flare (see, e.g., Figures 15(k) and (m), respectively). However, some short-term flares or their particular parts did not exhibit any clear trend, possibly owing to the coexistence of different acceleration mechanisms and complex physical conditions in the jet. Namely, such a spectral behavior was observed during MJD(596)65–77, when the source exhibited two subsequent short-term flares, including the two-peak instance with the highest 0.3–10 keV state in Interval 1 (see Figure 3(C4))). These results are in agreement with the repeated electron acceleration scenario proposed by Katarzynski et al. (2006): the initial shock acceleration, further energization by the second-order Fermi mechanism and eventual return of the electron in the shock acceleration zone.

The source showed a similar, very complex looping behavior during the exceptionally strong flaring activity in 2014 March–October (see Paper I) and during the short-term 0.3–10 keV

Table 15
List of the CW and CCW Loops Shown by Mrk 501 in the Photon Index–Flux Plane

Int.	MJDs	Variability Instance
		CW evolution
1a	(592)82–89	The fist peak of the two-peak flare presented in Figure 3(C1)
1a	(59)298–307	Two subsequent short-term, low-amplitude flares superimposed on the longer-term one
1a	(593)18–54	Two subsequent short-term flares in Figures 3(B1) and (A1), respectively
1a	(593)68–79	Short-term flare presented in Figure 3(B2)
1a	(593)81–98	Short-term low-amplitude flare superimposed on the long-term one
1a	(59)534–564	Final segment of the long-term brightness increase trend
1b	(595)64–93	Two-peak flare (Figure 3(C3))
1b	(596)35–43	Short-term flare presented in Figure 3(A3)
1b	(596)48–60	Two subsequent short-term, low-amplitude flares
1b	(596)63–65	Short-term, low-amplitude flare superimposed on the longer-term one
1b	(597)06-40	Two-peak flare (Figure 3(C5))
1b	(597)54–770	Short-term flare presented in Figure 3(A4)
1c	(597)75-87	The first peak of the two-peak flare in Figure 3(C6)
1c	(598)14-71	Nearly symmetric flare presented in Figure 3(D2)
		CCW evolution
1a	(592)57–82	The first short-term, low-amplitude flare
1a	(593)07–18	Two subsequent short-term flares
1a	(593)54–63	Short-term flare
1a	(59)398–442	Subsequent two-peak flare and that with a positive asymmetry (Figures 3(C2) and (A2), respectively)
1a	(59)459–534	Long-term flare superimposed on longer-term increasing baseline level
1a	(596)43–47	The second short-term flare, lower-amplitude flare in Figure 3(A3)
1b	(596)60–63	Short-term flare
1c	(59)787–814	The first peak of the two-peak flare in Figure 3(C6) and subsequent segment of long-term declining phase
1c	(59)899-945	Subsequent short-term flares (including that in Figure 3(C7))

Note. Note that the A panels represent the flares with a positive asymmetry in Figure 3; (B) those with the opposite asymmetry (slow brightening and fast decline); (C) two-peak flares; and (D) nearly symmetrical flares.

flares occurring in Intervals 2008–2010 and 2011–2013 (which we checked). Note that it is difficult to trace clearly expressed CW or CCW loops when the object is in low X-ray states that generally happened during 2016–2020. No clearly expressed loops were found by Mohorian et al. (2022) or Xue & Cui (2005) from the XMM-Newton (during 2022–2020) RXTE-ASM (in 1997) observations, respectively. During the RXTE-PCA and XMM-Newton observations in 1997–2000, Mrk 501 showed CW loops during the X-ray flares recorded in 1998 June and 1999 May flares, and no looping behavior was found in other cases (Gliozzi et al. 2006).

4.2.4. The Position of the Synchrotron SED Peak and Particle Upscatter Regimes

During the presented period of the long-term strong flaring activity, Mrk 501 was predominantly an extreme high-frequency peaked object (i.e., an HBL source with the synchrotron SED peak $E_{\rm p} > 1$ keV; Costamante et al. 2001; at least 68.5% of all curved spectra), exhibiting a wide range of the syncrotron SED peak position from $E_{\rm p} < 0.5$ keV to $E_{\rm p} > 5$ keV. As discussed in Section 3.2.3, we deal with upper limits to the intrinsic SED peak position in the first case. However, this peak was never situated beyond the threshold of 0.1 keV (i.e., at the UV frequencies), as deduced from the broadband optical-to-X-ray SED fit with the log-parabolic function $\log \nu F_\nu = A(\log \nu)^2 + B(\log \nu) + C$ (Landau et al. 1986). On the contrary, such very soft spectra were observed frequently in 2016–2020 when the source was showing the lowest historical 0.3–10 keV states. On the other hand, the source did not show extremely hard spectra with $E_{\rm p} > 10$ keV during 2021–2022, which were frequent in the intervals 2011–2013 and 2014–2015, with the most extreme case $E_{\rm p} > 29.4$ keV (which we derived from the spectrum corresponding to the third 340 s segment of ObsID 91138036, 2011 November 1, MJD 55,866.55). Finally, the synchrotron SED peak was located at energies $E_{\rm p} \sim 100$ keV or even beyond during the exceptional TeV/X-ray outburst in 1997 (Pian et al. 1998). Moreover, Mrk 501 was an ultra-high-energy BL Lac object (defined as an HBL source exhibiting the synchrotron SED peak at frequencies higher than 10^{19} Hz ($\approx$41.7 keV; see Giommi et al. 2001) in 1998 June, showing $E_{\rm p} \gtrsim 50$ keV (Sambruna et al. 2000). Consequently, Mrk 501 showed an overall variability of the synchrotron SED peak position by at least 3.1 orders of frequency $\nu_{\rm p}^{\rm sync} = E_{\rm p}/h$ Hz (where h is Planck's constant), which is the widest range reported for BL Lac object sources to date. Among other HBLs, the most extreme position of the synchrotron SED peak has been reported for 1ES 0033+595 ($E_{\rm p} = 23.19 \pm 1.98$; Kapanadze & Gurchumelia 2022).

Since the synchrotron peak position is related to the jet physical conditions, the extreme range of the $E_{\rm p}$ parameter values shown by Mrk 501 during 1997–2022 reflects a tremendous variability in values of the jet physical parameters. Namely, Tramacere et al. (2009) derived the relation $E_{\rm p} \propto \gamma_{3p}^2 B\delta$, where γ_{3p} is the peak of the distribution $n(\gamma)\gamma^3$, B is the magnetic field strength, and δ is the bulk Doppler factor in the emission zone. In the case of the log-parabolic EED $n(\gamma)$ (yielding a curved photon spectrum), this relation can be reduced to $\log E_{\rm p} \propto 2 \log \gamma_{\rm p} + (3/5b)$ (Tramacere et al. 2011), where $\gamma_{\rm p}$ is the peak electron energy. Consequently, the syncrotron SED peak position scales with this peak as $E_{\rm p} \sim \gamma_{\rm p}^2$ and the aforementioned overall variability $\nu_{\rm p}^{\rm sync}$ by more than 3.1 orders of frequency yields an overall shift the EED peak $\gamma_{\rm p}$ by up to 2 orders of the peak energy. On the other hand, this shift can be caused by an extreme change of the jet physical parameters (first of all, the magnetic field strength).

On the other hand, the source was not detected at the 5σ confidence level with BAT in Interval 1 (by adopting any time integration), in contrast to the frequent detections and strong 15–150 keV flares in the intervals 2011–2013 and 2014–2015, as well as during 2005–2006. This result could be related to the lack of the ultrarelativistic electrons with energies capable of producing hard X-ray photons via the synchrotron mechanism beyond 15 keV. In Section 4.2.2, we discussed the possibility of joint operation of the different acceleration mechanisms in the emission zone: a cycle of the initial particle acceleration at the shock front, followed by escape and further acceleration in the shock downstream area via the stochastic process and reentering the shock acceleration region. In the case that this

cycle is repeated many times, the particle can gain a very large energy and fill the EED's highest-energy tail, responsible for the BAT-band emission. Presumably, this process was not as efficient in Interval 1 as in the aforementioned periods of the frequent detections and flaring activity in the BAT band, likely owing to the weaker turbulence and, hence, weaker magnetic fields in the shock downstream area and less-efficient stochastic acceleration (resulting in the weaker anticorrelation $E_{\rm p}-b$ compared to those time intervals; see, e.g., Paper I).

Moreover, Hakobyan et al. (2021) demonstrated that fast magnetic reconnection can form a self-similar chain of plasmoids, which accumulate particles both from the adjacent current sheets and grow in time. Meanwhile, their interiors compress and amplify the internal magnetic field linearly with time. Eventually, this process leads to particle energization as a result of magnetic moment conservation and adding a nonthermal tail $f(E)\propto E^{-3}$ to the existing EED at higher energies, followed by an exponential cutoff. The cutoff energy can increase with time as $E_{\rm cut}\propto\sqrt{t}$, sometimes to extremely large values depending on the process duration and filling the EED's highest-energy tail with particle capable of producing the BAT-band emission. However, the process of formation of self-similar plasmoid chains was probably weakly developed in Interval 1 rather than in 2005–2006 and 2011–2015, resulting in the deficit in the EED's highest-energy tail and, hence, a weakness in the hard X-ray emission beyond 15 keV.

Note that Massaro et al. (2011) predicted a low probability (∼12%) for the generation of TeV photons in HBL sources when the curvature is larger than the boundary value $b^{*}=0.55$. However, such curvatures were not securely detected for Mrk 501 in Interval 1 when the source was very passive in the VHE γ-rays and was detected only four times with a significance of 3σ and higher during the 213 days of the FACT observations. Although the FACT data are not available after MJD 59,469, the LAT observations of Mrk 501 in the 100–500 GeV energy range allow us to draw some conclusions about the VHE activity of the source. Namely, it was not detectable with any significance in this energy range in Interval 1b, which was notable for the highest X-ray states during the presented 1.8 yr period of strong X-ray long-term flaring activity in 2021–2022. Note that the source showed a low $N_{\rm pred}$ value and, therefore, less-credible detection from the 100–500 GeV data collected with LAT during the entire period. On the contrary, the source showed a highly credible detection with up to 15σ significance in the shorter (≈1.5 yr) time interval of 2014–2015 and a similar situation was also in 2008–2010 where the duration of the LAT observations is only 10% longer than Interval 1 (see Table 12).

In the epoch of the strong long-term X-ray flaring activity and elevated optical-UV states, the passivity of the source in the VHE energy range and moderate activity at the MeV to GeV frequencies could be caused by high importance of the IC upscatter of optical-to-X-ray photons in the Klein–Nishina (K-N) regime. According to Tramacere et al. (2011), The K-N regime applies when $4\gamma\epsilon_0\gg 1$, with $\epsilon_0=h\nu_0/m_{\rm e}c^2$ to be the IC "seed" photon energy in units of $m_{\rm e}c^2$. In that case, the upscatter cross section $\sigma_{\rm KN}=(3/8)\sigma_{\rm T}\,\epsilon_0^{-1}\ln(1+2\ln 2\epsilon_0)$ is significantly smaller than that in the Thomson regime ($\sigma_{\rm T}$). Consequently, the IC scattering efficiency is significantly decreased as follows: (i) the upscattered photon energy scales as $\epsilon_{\rm KN}\sim\gamma$ (versus $\epsilon_{\rm T}\sim\gamma^2$ in the Thomson regime); and (ii) the SSC peak frequency $\nu^{p}_{\rm ssc}\approx(2/\sqrt{3})(\gamma_{\rm p}m_e c^2/h$ is much lower than its "counterpart" in the Thomson regime ($\nu^{p}_{\rm ssc}/\nu^{p}_{\rm sy}=(4/3)\gamma^2_{\rm p}$; Chen 2018).

Our suggestion is corroborated by a positive correlation between the UV and 0.3–300 GeV variabilities in Interval 1b, when the source was not detectable in the 100–500 GeV energy range with LAT and the mean 0.3–300 GeV flux was the lowest during 2021–2022 (see Tables 14 and 5). Such a correlation was explained as a K-N suppression of the UV-band emission by Tramacere et al. (2009). The scatter plot $F_{0.3-300\ \rm GeV}$–$F_{\rm UVW2}$ also shows a positive trend in Intervals 1a and 1c, although the correlation was below the 99% threshold. This result could be related to the significant contribution of the X-ray photons upcattered in the K-N regime to the MeV to GeV energies, while the UV-band and X-ray variabilities exhibited only a weak positive cross-correlation in Interval 1a and were not correlated in other parts of Interval 1. Finally, in favor of the K-N suppression of the higher-energy SED peak to the lower, MeV-band energies is that fact the Mrk 501 was detectable in the 30 keV–100 MeV band with INTEGRAL-IBIS during 2021–2022 (E. Pian 2023, private communication). Note that such detections were not reported in the past, and Mrk 501 was mentioned only in the INTEGRAL/IBIS 17-year hard X-ray all-sky survey (17–60 keV band; Krivinos et al. 2020).

The possible positive correlation of the HE γ-ray emission with that in the UV and X-ray bands (owing to the upscatter in the K-N regime) could also be weakened/destroyed by a significant contribution of LAT-band photons having an hadronic origin. Nevertheless, we discussed the possible importance of the hadronic cascades for the observed log-normal variability. In Sections 3.3 and 4.1.2, we discussed a frequent occurrence of the hard 0.3–30 GeV photon indices. Note that the majority of these instances were related to the harder Γ-values in the higher-energy 2–300 GeV band compared to that in the lower-energy 0.3–2 GeV one. According to Shukla et al. (2015), the origin of such hard higher-energy γ-ray spectra is much easier to explain in the framework of the significant hadronic contribution to this energy range. We performed this study for 4 week binned LAT observations of Mrk 501, in order to achieve significant photon statistics in the 2–300 GeV band. Harder 2–300 GeV spectra amounted to 38% of the cases in the here-presented period, with the highest portion in Interval 1c (see the last column of Table 1). The comparable portions were derived for the 2008–2010 and 2011–2013 intervals, while Interval 1b and interval 2014–2015 were notable for having the lowest percentage of the harder 2–300 GeV spectra.

The source also showed a strong positive correlation between the quantities $\log E_{\rm p}$ and $\log S_{\rm p}$, where $S_{\rm p}$ is the height of the synchrotron SED peak (see Figure 8(g) and Table 10). The latter parameter was calculated as $S_{\rm p}=1.6\times10^{-9}\,{\rm K}10^{(2-a)^2/4b}$ erg cm^{-2} s^{-1}(Massaro et al. 2004). Note that the scatter plot $\log E_{\rm p}$–$\log S_{\rm p}$ shows a slope $\alpha=0.43\pm0.08$, i.e., the source showed the relation $S_{\rm p}\propto E_{\rm p}^{\alpha}$ with the α-value relatively close to the case $\alpha=0.6$. This latter was predicted in the framework of the Monte Carlo simulations by Tramacere et al. (2011) and represents the case when the momentum-diffusion coefficient D is variable during stochastic acceleration of electrons. Namely, there should be a transition from the Kraichnan-type spectrum of the turbulence with the exponent $q=3/2$ into the "hard-sphere" spectrum ($q=2$). This parameter represents the turbulent field spectral slope defined as $W(k)=(\delta B k_0^2/8\pi)(k/k_0)^{-q}$, where

$k = 2\pi/\lambda$ is the wavenumber, and δB is the turbulent component of the jet magnetic field. In the "hard-sphere" regime, the scattering and acceleration timescales are independent of the particle energy. However, since the observed value of q is lower than that corresponding to the aforementioned transition, there should be a "contamination" of the second-order Fermi process by other plausible energization mechanisms, preventing the electrons to be accelerated sufficiently long for achieving the energies required to emit the BAT-band photons (as discussed above and in Section 4.2.2).

Mrk 501 also showed a $\log E_{\rm p}$–$\log S_{\rm p}$ correlation in each interval of the period 2008–2020 (see Table 10, as well as column 6 in Table 1 for the corresponding values of α). The α-exponent was closer to the case $\alpha = 0.6$ in 2011–2013 and 2014–2015, demonstrating a higher importance of the change in the turbulence spectrum for the observed spectral variations. Consequently, there should be a higher importance of the hard-sphere turbulence, imprinted in considerably stronger BAT-band activity. Finally, the aforementioned correlation was weak or very weak in the intervals 2008–2010 and 2016–2020 with $\alpha = 0.18$–0.30, excluding any dominant physical factor in the spectral variability (see Tramacere et al. 2009 for other expected values of the α-exponent and corresponding physical factors).

5. Summary and Conclusions

We present the results from the period of a prolonged, strong 0.3–10 keV activity of the nearby TeV-detected blazar Mrk 501 during 2021 February–2022 December. The MWL data sets provide information from optical to VHE γ-rays and were obtained by several space- and ground-based instruments: Swift-XRT, Swift-UVOT, Swift-BAT, MAXI, Fermi-LAT, and FACT. The basic results of our study can be summarized as follows:

1. The source underwent a strong long-term outburst in the 0.3–10 keV energy range during 2021 February–2022 December, which was comparable to those shown in the period 2012–2014. A long-term variation of the baseline X-ray level was superimposed by lower-amplitude flares of various strengths and profiles: nearly symmetric (variability is dominated by the disturbance's crossing timescale), positive and negative asymmetries (gradual particle acceleration and jet radial expansion with nonuniformity of the Doppler factor, respectively), two-peak maxima (collision of two relativistic "shells" with high-energy plasma, moving with different speeds). The 0.3–10 keV count rate showed an overall variability by a factor of $\sim$6 and exceeded a level of 15 counts s^{-1} (corresponding to about 5.3×10^{-10} erg cm^{-2} s^{-1}) in the peaks of some short-term flares superimposed on the plateau-like baseline level in the maximum epoch of the presented long-term flare. In some short time intervals, Mrk 501 was the brightest source in the 0.3–10 keV sky. No periodic variability was detected in any spectral range. The object showed different X-ray activity on intraday timescales: while the 0.3–10 keV brightness varied at the 99.97% confidence level during 16 XRT observations with exposures 0.24–0.96 ks and fractional variability amplitudes of 4.4(1.1)%–18.4(3.0)%, the densely sampled XRT campaigns revealed only a slow variability in some epochs.
2. On average, Mrk 501 showed elevated optical–UV states compared to the previous years, while such a behavior was not observed in γ-rays: the source was detected a few times with a significance of 3σ and higher by FACT, and the LAT data do not show the emission of the VHE energy in the 100–500 GeV band in Interval 1b, characterized by the highest X-ray states in the period presented here. Moreover, no long-term elevated activity was observed in the 0.3–300 GeV energy range in 2021–2022, characterized only by a moderate flaring behavior on the various timescales, which was significantly weaker than that observed during 2012–2015. Such a behavior and VHE passivity of the source could be caused by the dominance of the IC upscatter of UV-to-X-ray photons in the K-N regime (rather than upscattering the lower-energy synchrotron photons in the Thomson regime).
3. During the presented period, the log-normal function was well fitted with the histograms constructed by using the XRT and LAT-band fluxes, which hints at imprinting of the disk unstable processes on the jet (e.g., shock propagation through the jet was triggered by the disk instabilities). Moreover, the source showed a trend of weaker log-normality toward longer wavelengths, which is one of the features of the log-normality caused by random fluctuations in the particle acceleration rate. Alternatively, the log-normal variability in the LAT-band could also be contributed by hadronic cascades, the presence of which explains the frequent occurrence of the hard LAT-band spectra easier than the leptonic models. Finally, the intraday 0.3–10 keV variability clearly shows the impact of the local, purely jet-inherent instabilities resulted in non-log-parabolic variability.
4. More than half of the 0.3–10 keV spectra were consistent with the log-parabolic model, yielding a wide range of curvature parameter values $b = 0.12(0.06)$–$0.62(0.11)$. However, a vast majority of the log-parabolic spectra showed curvatures with $b \sim 0.3$ (expected in the case of efficient stochastic acceleration of the X-ray emitting electrons) or lower (joint operation of the first and second Fermi mechanism in the emission zone). The importance of the first-order Fermi acceleration process was imprinted in the higher percentage of the power-law spectra (45%) than during the exceptional flare in 2014 March–October. In the long-term brightness increase phase, the source showed an importance of the EDAP mechanism in the acceleration of the electron population with very low initial energy.
5. The 0.3–10 keV spectra showed ranges of the photon indices $a = 1.62(0.05)$–$2.22(0.05)$ and $\Gamma = 1.76(0.03)$–$2.28(0.03)$, which varied on various timescales. In this process, the source mainly followed a harder-when-brighter spectral evolution during the 0.3–10 keV flaring activity (along with the bluer-when-brighter chromatism at the optical–UV frequencies), explained by the injection of high-energy electron population with a hard energy distribution and by the dominance of synchrotron cooling of the highest-energy electrons over the IC cooling. The latter was corroborated by the strong correlation $E_{\rm p}$–$F_{0.3-10\,\rm keV}$, generally explained by the injection of high-energy particles in the shock acceleration process. Our results are in accordance with the simulation-based

expectations: as the quantity E_p increases, the mean cooling timescale of the X-ray-emitting electrons shortens and competes with the acceleration timescales, resulting in a weakening of the E_p–b anticorrelation. However, the source showed a deviation from the harder-when-brighter trend and followed the opposite spectral evolution during some time intervals of various durations. Such instances could be caused by the emergence of a soft-X-ray component in the X-ray emission zone, and their occurrence was most frequent in the phase of the long-term increase of the baseline 0.3–10 keV flux level. Therefore, we conclude that this long-term trend could be partially related to the frequent emergence of the new, soft flaring components in the emission zone (within the long-term increase in the matter collimation rate through the jet of Mrk 501).

6. The source showed very fast transitions of log-parabolic-to-power-law energy distribution and conversely for the spectra extracted from 150–600 s segments of some single-orbit Swift observations. Frequently, the resulting power-law spectra were hard, which could be produced by the electron population with a hard or very hard power-law EED, established by turbulence-driven reconnection in the relativistically magnetized jet area with a very small spatial extent of $\sim 10^{-12}$ cm. The source also showed such transitions over hours to 1 day timescales, with the presence of both hard and soft power-law spectra (implying a nonrelativistic magnetic reconnection in the latter case) on the spatial scales of $\sim 10^{13-14}$ cm.
7. At least 31.6% of the curved spectra with a secure detection of E_p showed the synchrotron SED peak position in the hard X-ray range, up to energies $E_p \sim 6$ keV and varying by $\Delta E_p = 0.28(0.15)$–$2.25(0.61)$ keV during some 0.3–10 keV IDVs. The source showed the relation $S_p \propto E_p^{\alpha}$, with the exponent value relatively close to the case of $\alpha = 0.6$, which is expected for a transition from the Kraichnan-type into "hard-sphere" turbulence.

Acknowledgments

B.K. and A.G. thank Shota Rustaveli National Science Foundation and E. Kharadze National Astrophysical Observatory (Abastumani, Georgia) for the fundamental research grant FR−21–307. M.A. acknowledges partial support from the University of Michigan Department of Astronomy. B.K. thanks Dr Daniela Dorner for her fruitful suggestions. This research has made use of the XRTDAS software, developed under the responsibility of the ASDC, Italy; the MAXI data were provided by RIKEN, JAXA, and the MAXI team; the data obtained through the High Energy Astrophysics Science Archive Research Center Online Service were provided by the NASA/Goddard Space Flight Center; the Swift-BAT transient monitor results were provided by the BAT team; the Fermi-LAT data and analysis tools are from the Fermi Science Support Center. Finally, we thank the anonymous referee for providing useful suggestions.

ORCID iDs

B. Kapanadze https://orcid.org/0000-0002-7146-6751
M. Aller https://orcid.org/0000-0003-2483-2103

References

Abdo, A. A., Ackermann, M., Ajello, M., et al. 2009, ApJ, 700, 597
Abdo, A. A., Ackermann, M., Ajello, M., et al. 2010, ApJ, 722, 520
Abdo, A. A., Ackermann, M., Ajello, M., et al. 2011a, ApJ, 727, 129
Abdo, A. A., Ackermann, M., Ajello, M., et al. 2011b, ApJ, 736, 131
Abdollahi, S., Acero, F., Ackermann, M., et al. 2020, ApJS, 247, 33
Abe, H., Abe, S., Acciari, V. A., et al. 2023, ApJS, 266, 37
Acciari, V. A., Ansoldi, S., Antonelli, L. A., et al. 2020, A&A, 637, A86
Acciari, V. A., Ansoldi, S., Antonelli, L. A., et al. 2021, MNRAS, 504, 1427
Aharonian, F., Akhperjanian, A. G., Anton, G., et al. 2009, A&A, 502, 749
Aharonian, F., Akhperjanian, A. G., Barrio, J. A., et al. 1997, A&A, 327, L5
Albert, J., Aliu, E., Anderhub, H., et al. 2007, ApJ, 669, 862
Anderhub, H., Antonelli, A. A., Antoranz, P., et al. 2009, ApJ, 725, 1624
Andruchow, I., Romero, G. E., & Cellone, S. A. 2005, A&A, 442, 57
Atwood, W. B., Abdo, A. A., Ackermann, M., et al. 2009, ApJ, 697, 1071
Barthelmy, S. D., Barbier, L. M., Cummings, J. R., et al. 2005, SSRv, 120, 143
Bodo, G., Tavecchio, F., & Sironi, L. 2021, MNRAS, 501, 2836
Böttcher, M., & Dermer, C. 2010, ApJ, 711, 445
Breeveld, A. A., Landsman, W., Holland, S. T., et al. 2011, in AIP Conf. Proc. 1358, Gamma-Ray Bursts 2010, ed. J. E. McEnery et al. (Melville, NY: AIP), 373
Burrows, D. N., Hill, J. E., Nousek, J. A., et al. 2005, SSRv, 120, 165
Catanese, M., Bradbury, S. M., Breslin, A. C., et al. 1997, ApJL, 487, L143
Chen, L. 2018, ApJS, 235, 39
Chen, X.-Y., & Wang, J.-X. 2015, ApJ, 805, 80
Costamante, L., Ghisellini, G., Giommi, P., et al. 2001, A&A, 371, 512
Dermer, C. D., Schlickeiser, R., & Mastichiadis, A. 1992, A&A, 256, L27
Dorner, D., Ahnen, M. L., Biland, A., et al. 2015, arXiv:1502.02582
Emmanoulopoulos, D., McHardy, I. M., & Papadakis, I. E. 2013, MNRAS, 433, 907
Falomo, R., Pian, E., & Treves, A. 2014, A&ARv, 22, 73
Fitzpartick, E. L., & Massa, D. 2007, ApJ, 663, 320
Foster, G. 1996, AJ, 112, 1709
Fukugita, M., Shimasaku, K., & Ichikawa, T. 1995, PASP, 107, 945
Gehrels, N., Chincarini, G., Giommi, P., et al. 2004, ApJ, 611, 1005
Giommi, P., Ghisellini, G., Padovani, P., & Tagliaferri, G. 2001, in AIP Conf. Proc. 599, X-Ray Astronomy: Stellar Endpoints, AGN, and the Diffuse X-ray Background, ed. N. E. White et al. (Melville, NY: AIP), 441
Giroletti, M., Giovannini, G., & Cotton, W. D. 2008, A&A, 488, 905
Gliozzi, M., Sambruna, R. M., Jung, I., et al. 2006, ApJ, 646, 61
Hakobyan, H., Petropoulou, M., Spitkovsky, A., & Sironi, L. 2021, ApJ, 912, 48
Kapanadze, B. 2021a, ATel, 15059, 1
Kapanadze, B. 2021b, ATel, 15124, 1
Kapanadze, B. 2021c, ATel, 15134, 1
Kapanadze, B. 2022a, ATel, 15477, 1
Kapanadze, B. 2022b, ATel, 15753, 1
Kapanadze, B., Dorner, D., Romano, P., et al. 2017, MNRAS, 469, 1655
Kapanadze, B., Dorner, D., Vercellone, S., et al. 2016, ApJ, 831, 102
Kapanadze, B., Dorner, D., Vercellone, S., et al. 2018, ApJS, 238, 13
Kapanadze, B., & Gurchumelia, A. 2022, A&A, 668, 75
Kapanadze, B., Gurchumelia, A., Dorner, D., et al. 2020, ApJS, 247, 27
Katarzynski, K., Ghisellii, G., Mastichiadis, A., et al. 2006, A&A, 453, 47
Kirk, J. R., Rieger, F. M., & Mastichiadis, A. 1998, A&A, 333, 452
Krimm, H. A., Holland, S. T., Corber, R. H. D., et al. 2013, ApJS, 209, 14
Krivinos, R. A., Sazonov, S. Y., Kuznetsova, E. A., et al. 2020, MNRAS, 510, 4796
Landau, R., Golisch, B., Jones, T. J., et al. 1986, ApJ, 308, 78
Lazarian, A., Eyink, G., Vishniac, E., & Kowal, G. 2014, in ASP Conf. Ser. 488, 8th Int. Conf. of Numerical Modeling of Space Plasma Flows (ASTRONUM 2013), ed. N. V. Pogorelov et al. (San Francisco, CA: ASP), 23
Liodakis, I., Marscher, A. P., & Agudo, M. 2022, Natur, 611, 677
Lomb, N. R. 1976, Ap&SS, 39, 447
Mannheim, K. 1992, A&A, 269, 67
Marscher, A. P. 2014, ApJ, 780, 87
Marscher, A. P., & Gear, W. K. 1985, ApJ, 298, 114
Massaro, E., Perri, M., Giommi, P., & Nesci, R. 2004, A&A, 413, 489
Massaro, F., Paggi, A., & Cavaliere, A. 2011, ApJL, 742, L32
Matsuoka, M., Kawasaki, K., Ueno, S., et al. 2009, PASJ, 61, 999
Mizuno, Y., Pohl, M., Niemiec, J., et al. 2014, MNRAS, 439, 3490
Moderski, R., Sikora, M., & Blazejowski, M. 2003, A&A, 406, 855
Mohorian, M., Bhatta, G., Adhikari, T. P., et al. 2022, MNRAS, 510, 5280
Mücke, A., Protheroe, R. J., Engel, R., Rachen, J. P., & Stanev, T. 2003, Aph, 18, 593

Nalewajko, K. 2013, MNRAS, 430, 1324
Nilsson, K., Pasanen, M., Takalo, L. O., et al. 2007, A&A, 475, 199
O'Neil, S., Kiehlman, S., Readhead, A. C. S., et al. 2022, ApJL, 926, L35
Padovani, P., & Giommi, P. 1995, ApJ, 444, 567
Pian, E. 2002, PASA, 19, 49
Pian, E., Vacanti, G., Tagliaferri, G., et al. 1998, ApJL, 492, L17
Poole, T. S., Breeveld, A. A., Page, M. J., et al. 2008, MNRAS, 383, 627
Pushkarev, A. B., Kovalev, Y. Y., Lister, M. L., & Savolainen, T. 2017, MNRAS, 468, 4992
Quinn, J., Akerlof, C. W., Biller, S., et al. 1996, ApJL, 456, L83
Rieger, F. M. 2019, Galax, 7, 28
Romero, G. E., Cellone, S. A., & Combi, J. A. 1999, A&AS, 135, 477
Roming, P. W. A., Kennedi, T. E., Mason, K. O., et al. 2005, SSRv, 120, 95
Roy, N., Chatterjee, R., Joshi, M., & Ghosh, A. 2019, MNRAS, 482, 743
Saito, S., Stawarz, Ł., Tanaka, Y. T., et al. 2013, ApJL, 766, L11
Saito, S., Stawarz, Ł., Tanaka, Y. T., et al. 2015, ApJ, 809, 171
Sambruna, R., Aharonian, F. A., Krawczynski, H., et al. 2000, ApJ, 538, 127
Scargle, J. D. 1982, ApJ, 263, 835
Shukla, A., Chitnis, V. A., Singh, B. B., et al. 2015, ApJ, 798, 2
Sinha, A., Khatoon, R., Misra, R., et al. 2018, MNRAS, 480, L116
Sironi, L., & Spitkovsky, A. 2014, ApJL, 783, L21
Sokolov, A., Marscher, A. P., & McHardy, I. M. 2004, ApJ, 613, 725
Tammy, J., & Duffy, P. 2009, MNRAS, 393, 1063
Tramacere, A., Giommi, P., Perri, M., Varrecchia, F., & Tosti, G. 2009, A&A, 501, 879
Tramacere, A., Massaro, E., & Taylor, A. M. 2011, ApJ, 739, 66
Tramacere, A., Massaro, F., & Cavaliere, A. 2007, A&A, 466, 521
Ulrich, M.-H., Kinman, T. D., Lynds, C. R., et al. 1975, ApJ, 198, 261
VanderPlas, J. T. 2018, ApJS, 236, 16
Vaughan, S., Edelson, R., Warwick, R. S., & Uttley, P. 2003, MNRAS, 345, 1271
Virtanen, J. J. P., & Vainio, R. 2005, ApJ, 621, 313
Wagner, S., & Witzel, R. 1995, ARA&A, 33, 163
Werner, G. R., & Uzdensky, D. A. 2017, ApJL, 843, L27
Willingale, R., Starling, R. L. C., Beardmore, A. P., et al. 2013, MNRAS, 431, 394
Xue, Y., & Cui, W. 2005, ApJ, 622, 160
Zhang, Y. H. 2010, ApJ, 713, 180
Zhang, Y. H., Treves, A., Celotti, A., et al. 2005, ApJ, 629, 686